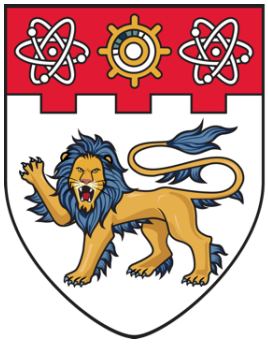

NANYANG TECHNOLOGICAL UNIVERSITY
SINGAPORE

ADVANCED CONTROL OF ELECTRICAL MACHINES IN MARINE APPLICATIONS

ZHAI JIANYANG

SCHOOL OF ELECTRICAL AND ELECTRONIC ENGINEERING

2019

ADVANCED CONTROL OF ELECTRICAL MACHINES IN MARINE APPLICATIONS

ZHAI JIANYANG

School of Electrical and Electronic Engineering

A thesis submitted to the Nanyang Technological University in partial fulfillment of the requirement for the degree of Doctor of Philosophy

2019

Statement of Originality

I hereby certify that the work embodied in this thesis is the result of original research, is free of plagiarised materials, and has not been submitted for a higher degree to any other University or Institution.

[Date Here]
4. Jan. 2019
Date

[Student's Signature Here]
Zhai Jianyang
[Studen's Name Here]

Supervisor Declaration Statement

I have reviewed the content and presentation style of this thesis and declare it is free of plagiarism and of sufficient grammatical clarity to be examined. To the best of my knowledge, the research and writing are those of the candidate except as acknowledged in the Author Attribution Statement. I confirm that the investigations were conducted in accord with the ethics policies and integrity standards of Nanyang Technological University and that the research data are presented honestly and without prejudice.

[Date Here]

4/1/2019

Date

[Supervisor's Signature Here]

WANG Youyi

[Supervisor's Name Here]

Authorship Attribution Statement

This thesis contains material from 2 published papers where I was the first and/or corresponding author.

Chapter 3 is published as J. Zhai, Y. Wang and X. Liu, "Optimal reset controller designed for induction machine drive with hardware in the loop test," 2017 IEEE Applied Power Electronics Conference and Exposition (APEC), Tampa, FL, 2017, pp. 506-511.

The contributions of the co-authors are as follows:

- Prof. Wang Youyi provided the initial project direction and edited the manuscript drafts.
- I prepared the manuscript drafts. The manuscript was revised by Dr. Liu Xiong. I presented the paper at the conference.
- I designed the control algorithm and verified it with simulation.
- I co-designed the Hardware-in-the-Loop (HIL) test rig and performed the laboratory work at the Rolls-Royce Advanced Technology Centre (ATC) at Nanyang Technological University. I also analyzed the data.

Chapter 4 is published as L. Niu, J. Zhai, X. Liu, Y. Wang and A. K. Gupta, "A smooth and fast transition method for PMSM SMO based sensorless control," 2016 IEEE 2nd Annual Southern Power Electronics Conference (SPEC), Auckland, 2016, pp. 1-6.

The contributions of the co-authors are as follows:

- Prof. Wang Youyi and Dr. Amit Kumar Gupta provided the initial project direction and edited the manuscript drafts.
- Dr. Niu Li prepared the manuscript drafts. The manuscript was revised by Dr Liu Xiong and I. I presented the paper at the conference.
- Dr. Niu Li and I designed the PMSM hard test rig and performed the laboratory work at the Electrical Power Systems Integration Lab @NTU (EPSIL@N). I also analyzed the data.

Zhai Jianyang

[Date Here] [Student's Signature Here]

4 Jan 2019 Zhai Jianyang

Date [Student's Name Here]

Acknowledgment

I would like to express my sincere gratitude to my supervisor, Prof. Wang Youyi, for his guidance and encouragement during my Ph.D. research work. He is not only a great academic supervisor to me, but also a mentor of life. I would also like to thank my ex-supervisor, Dr. Gilbert Hock Beng Foo who led me into the field of electric machine drives. A special thanks goes to Dr. Liu Xiong from Rolls-Royce who gave me so many valuable inspirations and insightful suggestions. I must thank Nanyang Technological University and RollsRoyce@NTU Corporate Lab for the award of the funding that made my research possible. I am particularly grateful to everyone in the "low-voltage drive" team. They are Dr. Han Kun, Dr. Niu Li, Dr. Madishetti Sandeep, Mr. Boggarapu Yasho Bharat, and Dr. Yoon Changwoo. Working with all of you have been a valuable experience and a wonderful time for me. My special thanks go to Prof. Hu Guoqiang and Prof. Huang Xiaoyang for their the help, guidance, and support as my thesis advisory committee members.

Next, I wish to express my gratitude to my colleagues and friends in NTU for their help, encouragement, and inspiration. They are Mr. Shi Donghan, Mr. Yu Yang, Dr. Liu Yong, Dr. Zhang Yicheng, Dr. Tu Pengfei, Mr. Fan Fei, Mr. Wang Shuai, Dr. Ji Dongxu, Dr. Xu Qianwen, Dr. Ma Xiaohe, Dr. Yin Shan, Dr. Zhang Xinan, Dr. Zhang Xiaolong, Dr. Ju Chengquan, Dr. Jin Chi, Dr. Liu Yitao, Dr. Hu Xiaolei, Dr. Liu Sijun, Dr. Guo Fanghong, Dr. Gabriel Ooi Heo Peng, Mr. Pabbathi Venkatesh, and Dr. Kavil Kambrath Jishnu.

Last but never least, I would like to address my sincere love and appreciation to my parents for their support and encouragement during the past four years. I want to give my deepest love to my girlfriend, Ms. Ju Chen, for her support and tenderness during my academic pursue.

Table of Contents

List of Figures

List of Tables

Summary

With the rapid development of power electronic devices, the ideas of more-electric ships (MES) and all-electric ships (AES) have become practical. A shipboard power system (SPS) permits more efficient utilization of the energy provided by fossil fuel. Electricity can be easily transported through cables or wires, which considerably saves space and reduces weight. This update creates an impact on almost every part of the system, including the power distribution system, the propulsion system, and the auxiliary system.

Electric machines (both thrusters and deck machinery products) are the most critical parts on an SPS. The traditional direct connection between the prime mover and the propeller is replaced with an electrical propulsion system. The operation speed for an electrical propulsion system is not fixed. Thus it can run at any optimized speed to reduce fuel consumption. The dynamic performance of an electric machine is better than diesel engines or gas turbines. The whole system becomes more robust, and the maintenance cost is minimized. These advantages would not have been possible without the development of electric machine drives. This thesis is focused on improving the performance of electric machines.

To begin with, in response to the complicated environment in marine applications, requirements to the dynamic performance are higher. A novel algorithm named the optimal reset controller (ORC) is introduced to the speed controller of electric machines. The ORC continuously resets the state of the base system through a designed optimal law. Through which, the transient response is improved while the overshoot is eliminated. The algorithm is shown in detail. It is verified by hardware-in-the-loop (HIL) tests and experiments conducted on a 15 kW induction machine test rig.

Next, regarding the extreme operation conditions in marine applications, the demand for the permanent magnet synchronous motor (PMSM) sensorless control is growing. Since the traditional back-EMF sensorless control method has

limited performance in low speed, a common approach is to start the machine in an open loop and switch to closed loop sensorless controller when the machine is accelerated. The switching transient may cause current overshoot and machine vibration. The switching transient is comprehensively analyzed, and a smooth transition method is proposed. It is a closed loop approach to reduce the q-axis current gradually with the error angle as the feedback. The simulation verifications are shown. Hardware experiments are conducted on two sets of PMSM test rigs rated 3 kW and 50 kW, respectively.

In marine applications, parameter variations have always limited the system performance and jeopardizing the robustness. Electric ships are required to work in diverse environments. They may have to work under a considerable variation of temperatures. In addition, they may endure a long-term operation without maintenance during ocean-going voyages. On the induction machine (IM) part, the parameter variation conditions are reviewed. The rotor resistance R_r is the most important parameter in the slip speed calculation of indirect field oriented control (IFOC). The DQ misalignment that caused by parameter variations is analyzed, a novel method is proposed to estimate the DQ misalignment angle, and compensate it through an updated R_r. In the simulation, the influence of parameter change on the DQ misalignment angle is shown, and the effectiveness of the proposed method is verified. Hardware tests are carried out on the 15 kW IM. Error angles under different rotor time constants are calculated to test the proposed method.

Equivalently, the effect of parameter variation on a PMSM is discussed, and the on-line identification methods are presented. A rotor flux Luenberger observer is introduced. The equations are derived, and the hardware test results are reviewed. There is a 6% error between the estimation and the measurement. The possible causes are discussed. Next, an on-line recursive least square (RLS) method is applied to identify multiple PMSM parameters at the same time. Experiment results are shown. It is proved that this method is highly sensitive to the test environments. The effect of the d-axis current perturbation and the setting of the forgotten factor are very important parts for the algorithm design. They are discussed thoroughly in this chapter. Simulation and experiment results are conducted on the 3 kW PMSM test rig.

Acronyms and Nomenclature

List of Acronyms

AC	Alternating Current
ADC	Analog-to-digital Converter
AES	All Electric Ships
ANN	Artificial Neural Network
Back-EMF	Back Electromotive Force
BLDC	Brushless DC Machine
CAN	Controller Area Network
DC	Direct Current
DP	Dynamic Positioning
DFIG	Doubly Fed Induction Generator
DQ	Direct Quadrature
DSP	Digital Signal Processor
DSPM	Doubly Salient PM
DTC	Direct Torque Control
EAT	Electrically Assisted Turbocharger
EKF	Extended Kalman Filter
EMF	Electromotive Force
EV	Electric Vehicle
EPM	Electric Propulsion Module
EPS	Electric Propulsion System

FOC	Field Oriented Control
FORE	First Order Reset Element
FRPM	Flux Reversal PM
FSPM	Flux Switching PM
FPGA	Field-programmable Gate Array
GPIO	General Purpose Input/output
HDD	Hard Disk Drive
HF	High Frequency
HIL	Hardware in the Loop
hp	Horsepower
HVIL	Hazardous Voltage Interlock Loop
IGBT	Insulated-Gate Bipolar Transistor
IM	Induction Machine
IPM	Interior PM
JTAG	Joint Test Action Group
LQR	Linear Quadratic Regulation
MES	More Electric Ships
MEA	More Electric Aircraft
MIMO	Multi-Input Multi-Output
MRAS	Model Reference Adaptive Systems
MTPA	Maximum Torque per Ampere
ORC	Optimal Reset Controller
PI	Proportional-integral
PM	Permanent Magnet
PMSM	Permanent Magnet Synchronous Motor
PFC	Power Factor Correction
RLS	Recursive Least Square
RPM, rpm	Revolutions per Minute
RTDS	Real-time Digital Power System Simulator

SCI	Serial Communication Interface
SRM	Switched Reluctance Motor
SPI	Serial Peripheral Interface
SPS	Shipboard Power System
SMO	Sliding Mode Observer
SyncRel	Synchronous Reluctance
SRM	Switched Reluctance Motor

Nomenclature

B	Friction Factor
d	(subscript) Direct Axis
C	Capacitance
E	Energy
e	(subscript) Electrical
f	Frequency
G	Gravitational Acceleration
J	Inertia
I, i	Current
L	Inductance
M	(subscript) Mutual-inductance
N or n_p	Number of Pole Pairs
P	Power
q	(subscript) Quadrature Axis
R	Resistance
T	Torque
	(Superscript) Matrix Transpose
t	Time
V, v	Voltage
W	Watt
ω	Rotation Speed
θ	Angle
ξ	Damping Factor
λ	Flux Linkage
τ	Time Constant

Chapter 1

Introduction

1.1 Background

The traditional marine system has changed profoundly with the development of electric devices and machines [1]. The idea of a more-electric ship (MES) has become practical due to the rapid development of power electronic devices since 1990s [2]. The update will impact almost every parts of the system, covering the propulsion system, the power distribution system, auxiliaries, sonars and radars.

A shipboard power system (SPS) permit a more efficient utilization of the energy provided by fossil fuel. The electricity is easy to transport through cables or wires, which considerably saves space and reduces weight. The power generation and distribution system in a electric ship are connected with an AC bus [3]. For other occasions, DC distribution bus has been installed where it is adapted with AC/DC converters. The voltage range for a DC bus is between 1.5 kV to 3 kV [4]. A typical configuration of the future SPS is presented in Figure 1.1. The prime mover for generators on most electric ships are diesel engines or gas turbines. The propulsion system is the crucial load on board. It is connected to an AC/DC/AC inverter. Other loads include lighting, communications, radar, cranes pumps are also powered through the main bus. In addition, power storage and supply units like battery banks, fuel cells or super capacitors are fundamental to the overall stability of the whole system.

This thesis focuses on the electric machine drive in a marine system. Among all marine applications of electric machines, the electric propulsion system consumes most power that generated. The history of electric propulsion system is dated back to the 1920s when twin 3,500 hp (about 2611 kW) turbo-electric propulsion

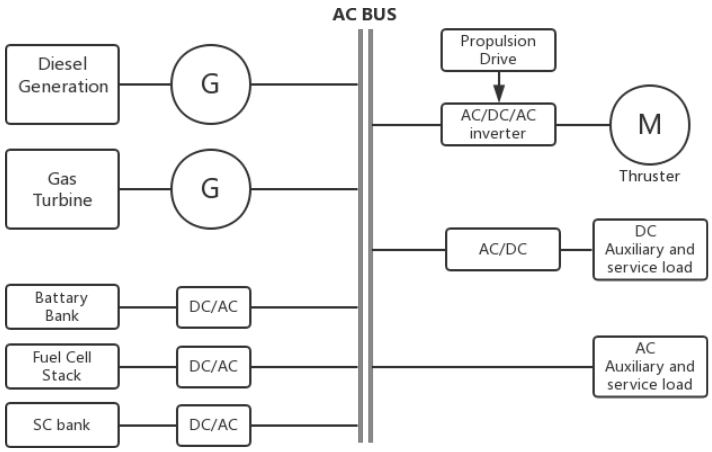

Figure 1.1: Simplified configuration of AC-SPS [5]

plants were installed on a battleship named the US Jupiter [3]. By the year of 2010 the power load of specific warship modules have reached 9000 kW. It is estimated to be doubled by 2020. On civil use, the first all-electric cargo ship has launched in Guangzhou, China by the end of 2017 [6]. This remarkable vessel is equipped with a 2,400 kWh lithium-ion battery. The electric ships have a positive influence on the environement too. It is estimated that global greenhouse gas emissions will be decreased by 2% by replacing the traditional cargo ship with an electric one [7].

Figure 1.2 shows four typical electrical machine applications on the marine thrusters and deck machinery systems [8]. The electrical propulsion system contains several sets of motors. The main thruster(s) provides the forward force for a ship. It is placed on the back of the ship. Tunnel thruster (Figure 1.2a) and /or azimuth (podded) thruster(s) (Figure 1.2b and 1.2c) are innovations of the modern propulsion system. They are installed beneath the keel and bring more agility for the ship. Azimuth thrusters are designed in a pod shape and connected to a shaft which is able to rotate to any horizontal angles. It can take the place of the rudder in some applications. An electrical winch is shown in Figure 1.2d, which is a typical deck machinery.

Various kinds of electric machines have been introduced to the marine propulsion system. The technology is the most mature on a induction machine. The PMSM, on the other hand, also have several commercialized applications avail-

(a) PM tunnel thruster (PMTT)

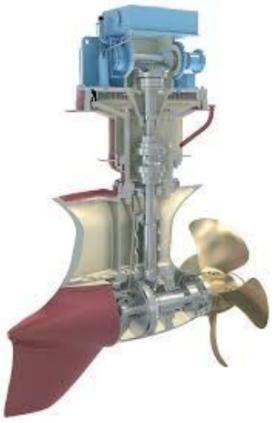

(b) Azimuthing thruster driven by induction machine

(c) Azimuthing thruster driven by PM L-drive

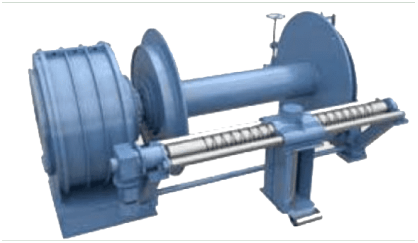

(d) Trawl winch with PM motor

Figure 1.2: Propulsion and deck machinery products [8]

able. Novel designs like reluctance motors are still under development [9]. There are various requirements on the machine for different ships. The listed characters should usually be covered.

- **Power density:** Although requirements on the power density for a more electric ship (MES) is not as strict as it is on a more electric aircraft (MEA), it remains as a significant concern given the enormous power demand. Take the modern electric cruise liners Queen Mary II as an example, its total power is 86 MW [10], the total weight for electric machines and power converters is as high as ten tons. Less weight for the machine and the converter means higher efficiency or more cargo loads.
- **Torque density:** Some electric ships particularly requires high torque in operations, for example, icebreakers or towboats. Additionally, all electric ships would appreciate high torque during startup.
- **Robustness:** In a marine application, the working conditions are harsh for all equipments on board. To begin with, the salty environment deals much damage to electric devices. Additionally, the machines should be strong against continuous vibrations. Lastly, sensors become fragile in extreme working conditions, which leads to intense demand for sensorless control algorithms.
- **Cost:** Cost is always an important concern in industrial designs.

Each type of motors have its own advantages considering the requirements that listed [11]. PMSMs are supreme because of their high power and torque density. On the other hand, PMSMs are less economical friendly due to its demand on the rare-earth material. Induction machine (IM) has the lowest cost since it has elementary structure and its manufacturing processes are mature. The cost and performance of a switched reluctance machine (SRM) are in between of these characters in the IM and the PMSM. However, the torque ripple for SRM under low speed should never be ignored. The research topic in this thesis is focused on the IM and the PMSM due to requirements of particular industrial projects.

1.2 Motivation

The benefits of the electric propulsion system (EPS) are obvious [12]. First, the traditional direct connection between the prime mover and the propeller is

decoupled. A electrical propulsion system can run at various speed in case its fuel consumption is optimized [13]. Secondly, on modern ships, more electric power is consumed by the auxiliary load on board. Applying a electric propulsion system makes the shipboard grid further integrated. Lastly, the ship with EPS has the potential of accessing renewable energy sources like solar and wind.

The challenges in electrical machine drive in marine applications can be listed in the following points.

- **Dynamic response:** The sea current and wind are changing continuously on the ocean. That brings challenges to a ship who is required to maintain its position while performing certain tasks. This process is normally refered to as dynamic positioning (DP). It is realized by consistently changing and tracking the reference speed in the machine drive. On the other hand, the propeller may get lifted out of the water then throw back in few seconds in a heavy storm, which induces a large and sudden load torque change. Strong and robust dynamic response is very important in that conditions.

- **Sensorless control:** Speed/position sensors are essential but fragile in the control system. Sensorless control is normally equipped as a backup system in case of the sensor failure. In addition, it is impossible to install a speed sensor in some particular applications. For example, on a novel, high-efficiency rim driven thrusters (shown in Figure 1.3), the blades are mounted on a ring which equivalents to the rotor. In that case, there is no shaft for a traditional speed sensor to install. The sensorless control is considered as a solution for the control on rim driven thrusters.

- **Parameter variations:** Machine parameters are influenced by many factors. They may change after the machine is installed, which brings challenges to the controller. Electrical parameters change with the motor working conditions. Mechanical parameters depend on the lubrication condition and the load or machine which connected to the same shaft. Parameter errors influence many model-based control algorithms. Parameter identification is very important to the advanced control of electrical machines. In addition, parameter identification is essential when overcoming the challenges on the dynamic response and the sensorless control.

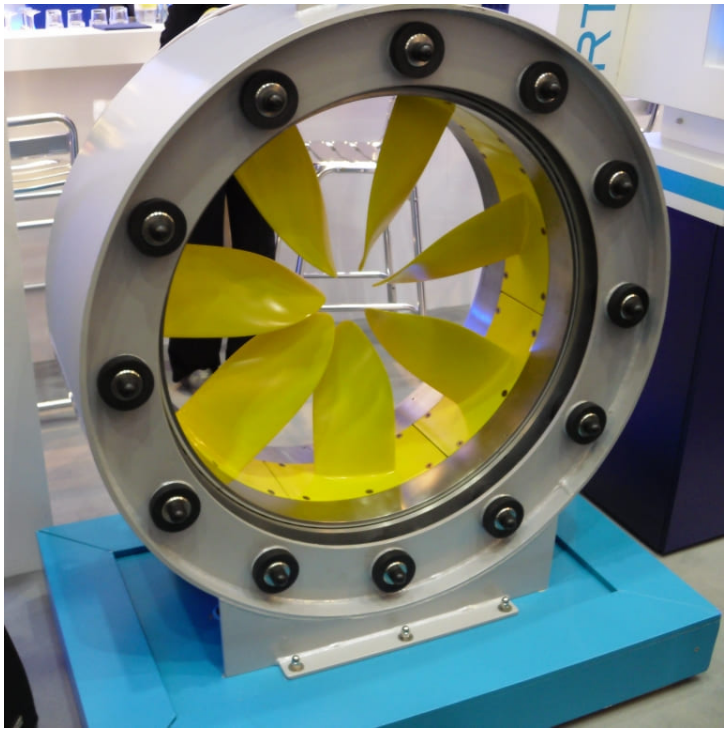

Figure 1.3: Rim Thruster, presented at SMM 2010 [14]

1.3 Major Contributions

In this thesis, analyses are made on the remaining challenges in electrical machine drives for marine applications. Algorithms and methods are proposed. Simulation and hardware test results are shown. The major contributions are listed as follows.

- The optimal reset controller (ORC) is proposed to improve the dynamic response of the electric machine drives. As a non-linear method, a ORC is designed to overcome the limitations of the conventional linear controller to eliminate the overshoot while sustain a fast response speed. The optimal law is calculated by solving the Riccati equation in a linear quadratic regulation (LQR) problem. The proposed algorithm is tested by a simulation, a hardware in the loop (HIL) test and an experiment on a 15 kW induction machine (IM). Hardware results show that the ORC is suitable as an add-on to the stable base proportional-integral (PI) controller. Under various PI controller damping ratios, the ORC provides improvements to the system dynamic response. In sudden load tests, the rotor speed recovery time for the ORC is faster than its base PI controller.

- A smooth transition method is proposed to improve the transient performance between a open loop starting and the sensorless FOC in the PMSM. This method is based on a gradually reduce of the current misalignment angle during the transient. The q-axis current decreases gradually based on the closed-loop feedback of a defined angle error signal. In simulation and hardware test results, the proposed method improved the transient current, torque or speed responses.

- For the parameter identification on the IM, the most critical parameter is the rotor resistance, as it is the reason for $d-q$ axis misalignment. In this thesis, a novel method is proposed to find the $d-q$ axis misalignment angle without identifying rotor resistance. Simulations are carried out to verify the accuracy of the identified error angle. In the hardware test, the rotor resistant value is identified by finding the slightest error angle with the proposed method.

- For the PMSM parameter identification, the on-line parameter identification method based on the recursive least square (RLS) method is explored. It is found through hardware test that the test condition for RLS are very important and it should not be neglected in previous literature. In addition, in a previous literature, boundaries of the estimation region are given to the specific parameters to guarantee the algorithm convergence. In this thesis, the boundaries are removed. The influence of forgotten factor and perturbation setting on RLS convergence issue is illustrated. In both simulation and hardware tests, the RLS algorithm convergence is achieved. Possible reasons of identification error are discussed.

1.4 Thesis Organization

Chapter 1 is the introduction of the history and the background of electric ships and the application of electric machines on-board. Primary concerns and challenges are pointed out. Motivations and major contributions for this thesis are given.

Chapter 2 reviews the background knowledge of the electric ship and marine environments, along with electric machines and their fundamental control techniques. Typical modules on a more electric ship are reviewed. The mathematical model for both PMSM and IM are presented. Additionally, widely used control

methods like the field oriented control (FOC) and the direct torque control (DTC) are introduced.

In Chapter 3, previous researches on the ORC are reviewed. The reset law is derived for electric machine speed loop control. Simulations are made. Hardware test result is carried out on both the HIL test and a 15 kW IM test rig. The hardware of HIL real-time simulator and the IM test rig are introduced in this chapter.

Chapter 4 focuses on the sensorless control of the PMSM. A back electromotive force (EMF) based sliding mode observer (SMO) is tested. Its robustness analysis and the design of a low-pass filter are shown. A smooth transition method is proposed to relieve the current overshoot during starting. Hardware tests are carried out on a 3 kW PMSM test rig and a 50kW PMSM test rig. The introduction on both PMSM test rigs are included.

The subject for Chapter 5 is correcting the potential parameter variation for the IMs. Slip speed is essential for all asynchronous machine operations. In the calculation of the slip speed, the rotor resistance plays an important role, which makes it a variation sensitive parameter with top-priority. In this chapter, this issue is examined from the direct-quadrature (DQ) current misalignment angle. The theoretical analyses are performed. A novel method is proposed to find the potential rotor resistance variation through the DQ misalignment angle. The hardware test results are shown.

In Chapter 6, the parameter identification methods for the PMSM are established. Two methods are implemented, namely the Luenberger observer and the recursive least square (RLS) method. The former only estimates the rotor flux while the latter works as a full order observer that estimates four important parameters: direct-quadrature inductances L_q, L_d, rotor resistance R_s, and rotor flux linkage λ_r. The hardware tests are carried out on the 3 kW PMSM rig. The estimation results are compared with the measured one. The possible reason for the error is discussed.

Chapter 7 concludes the thesis and offers recommendations for the future research.

As introduced in "IEEE Standard Test Procedure for Polyphase Induction Motors and Generators" [15], for whenever the word "motor" is used, it can be replaced with the word "generator", similarly, whenever "machine" is used, it can be replaced with either generator or motor. The only difference would present within the energy flow direction. The same idea could be applied to this

thesis. However, the works on electrical machines, including theoretical analysis, simulation, hardware tests, will be focused on their motor applications.

Chapter 2

Electric Ships and Electric Machines

In this chapter, the technologies about advanced control of electric machines in marine applications are reviewed. To begin with, the conceptions of MES and AES are introduced. Their shipboard power system and propulsion system are introduced in particular. Next, a review is conducted on a list of electric machines that have been or have a potential to be applied in the marine propulsion system. Among the list, the IM and PMSM will be discussed comprehensively in this chapter, while the other types of machines like the stator-PM machine, the brushless DC machine and the reluctance machines are briefly introduced. In the end, the fundamental knowledge about electric machine drives is provided.

2.1 MES and AES

In this section, the literature about MES and AES are reviewed. The ship power system is illustrated. Two modules, the propulsion module and deck machinery module which carrying the electric machine and its drives, are presented in particular.

2.1.1 Shipboard Power System

Many SPS schematics have been proposed to develop MES or AES [12]. In a general SPS, the following modules are included [16].

- Power generation module (PGM)

- Energy storage module (ESM)
- Power conversion module (PCM)
- Electric propulsion module (EPM)
- Loads (vital/non-vital)

On the MES, the diesel engines or gas turbines are applied to power the main propeller while also as the prime mover to generate power for the electrical loads on board. On the AES, the diesel engines or gas turbines are introduced only as the generator prime mover [17]. The SPS on an AES is designed to supply power for all the loads on board. The electric propulsion system will consume most of the power. In some particular applications, such as in the warships, weaponry systems can also be energy consuming [18].

To ensure the power supply for various type of loads, a particular power management procedure is necessary. A method to achieve optimized coordination between the power generation module and the energy storage module is discussed by Seenumani et al. in [12, 19].

Many research has been made on the AES power system optimization. The configuration [20] and construction [5] of the SPS are introduced. In [21], the focus is on the limitation of the greenhouse gas emissions with dynamic programming. The power factor is another appealing angle for the optimization. It is estimated in [22] that the overall efficiency of the generators increase from 91% to 93.5% with the power factor changed from 0.8 p.f to 1.0 p.f. The power factor correction (PFC) is applied to the ship board generators in [23].

Lastly, the electric propulsion module (EPM) is the subject of this thesis. Many characteristics of the SPS are shared when the EPM is discussed. For example, both long time horizons and transient performances are concerned. Their robustness and economic are also fundamental concerns.

2.1.2 Electric Propulsion Module

It is estimated that the efficiency for the electric propulsion system is around 95% while the optimal efficiency for a traditional one is about 85% to 90% [24]. For lower torque working conditions, the efficiency contrast is sharper. In an AES, the propulsion system is as an electirc load on board, the number of prime movers is reduced, the system flexibility is improved and the fuel consumption is further reduced. [25].

Advantages of Electric Propulsion

With the electric propulsion system, the thermal engine is allowed to work under more efficient speeds. As a result, the fuel consumption is reduced. Besides, the vibration and noise are minimized, which leads to a more comfortable environment for the crew.

In addition, the dynamic performance for the electric propulsion is superior. In motor starting, arresting or speed variation conditions, they can provide more robust and fast response to fit the special requirements that tradition propulsion system cannot comply [17].

Next, an electric machine creates a possibility of more flexible accommodations. For example, they can be installed with a short shaft or in the podded propellers. Therefore, their efficiency and maneuverability are improved. This feature will be further discussed Section 2.1.2 about the propulsion system structure.

Lastly, the automated control requires less crew. Human resource cost is reduced.

Electric Propulsion Applications

Acknowledging the advantages of the electric propulsion system, it is legitimate to estimate that most of the traditional propulsion system in the future will be replaced with an electric one. However, it will be a gradual process with the constraints of the cost and technology development.

The implementation will be various, depending on marine applications. The major categories are ocean-going, station keeping, ice-breaking [24] and naval [25].

Ocean-going refers to the application of the electrical main propellers on the vessels. In current designs, the power rating for the main duel propellers is up to 20-25 MW each [26]. Traditionally, synchronous motors are applied. Asynchronous machines are also introduced in recent years.

Station keeping is another challenging subject. Its objective is to maintain the vessel position during operations on the ocean surface. In that condition, the propeller is tuned to provide high torque under an extremely low speed [27]. For example, a marine riser is used for transportation of oil or gas from the seabed to the ocean surface. The disturbances to station keeping consists of wind, wave, and ocean current [28, 29]. This technique is also referred to as dynamic positioning (DP). Other applications of DP are oceanographic research vessels, cable layer

ships, and cruise ships [30].

Ice-breaking requires the electric machines to work in a over-torque operations. Since the 1990s, podded propellers are introduced to the icebreakers, who have a 360-degree steerable angle. That makes it possible to shift its course in the critical condition near the northern polar regions.

The electric propulsion system on a naval ship is another research orientation. Adapting to the electric system considerably increases the flexibility and the survivability of the ship. Next, in naval applications the requirments are higher on the stealth and noise reduction. In the end, the robustness and lower maintenance cost for the EPS are both excellent characters for the naval ships [25, 31].

Propulsion System Structures

In contrast to the traditional mechanical propulsion system, the electrical one finally free itself from the mass amount of gear and the strict shaft installation restrictions. The improvements on the flexibility are observed in the "in-hull" and the "podded propulsion" structures.

The first structure is the "in-hull" propulsion shaft which is similar to the traditional mechanical system. In such structure, a shaft is placed in the hull of the ship. The direction control is still achieved by a rudder. The improvement for this structure is in the reduction on the shaft length, and the motor is placed closer to the propeller [25].

Another novel structure is the "podded propulsion" system, in which both the machine and propeller are integrated in a pod and placed beneath the water. As a result, the propeller can rotate horizontally. In some contemporary designs by Rolls-Royce and ABB, a podded propeller can rotate 360 ° (Figure 2.1). In that case, the propeller also plays the role of the rudder. The ship maneuverability is greatly improved. In addition, the podded structure reduces the volume and the weight of the motor cooling system.

2.1.3 Winches and Deck Machinery

Except for the propulsion system, the winches and the deck machinery are the most common modules that involve electirc machines on the civil ships. A winch is a machine that designed for lifting or pulling the heavy objects with a rope or a chain. It has a wide range of operations. For example, in some heavy lifting works of anchoring, cargo lifting, and mooring winches, their controller design

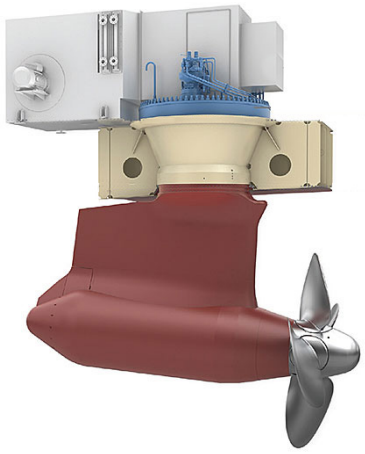

(a) “Mermaid” podded propulsors from Rolls-Royce [32]

(b) “Azipod” from ABB [33]

Figure 2.1: Podded propulsion system

is straightforward since the efficiency is the only concern [34]. A typical anchor handling and towing winch is shown in Figure 2.2.

On other applications, the machine control is more important. For example, in [36], the winch is designed for a submarine cable laying operation, the tension on the cable must be controlled within a particular range. A fuzzy control logic is applied for tension control. When the rope has an angle with the winch drum, the force on winch motor shaft will be stressed and unbalanced. In [37], the current signature in such conditions are analyzed.

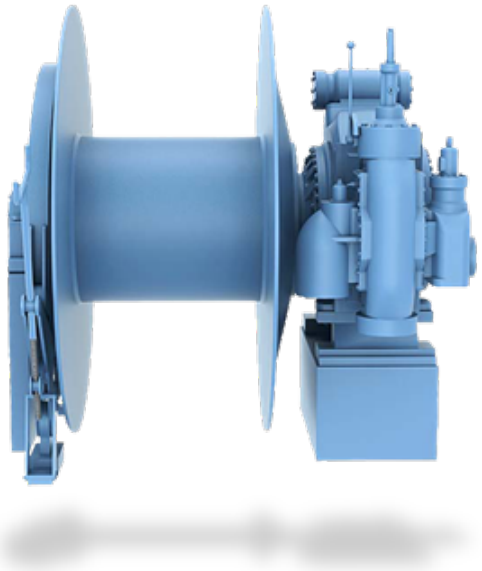

Figure 2.2: Anchor handling and towing winch by Rolls-Royce [35]

The winch controller design also influenced by large parameter variations. The machine moment of inertia and the torque radius change with the varying amount of the chain or the rope on the drum. In that case, the winch controller parameters require consistantly adjustments.

2.2 Induction Machines

Both IMs and PMSMs are commonly applied to the EPS and the deck machineries. Their detailed reviews are made in Section 2.2 and Section 2.3.

The history of the IM is very long. It was invented by Galileo Ferraris and Nikola Tesla dated back in 1887 [38]. It has always been a strong candidate for the propulsion system machine after the idea of MES or AES was proposed [39].

2.2.1 Industrial Applications for IM

The industrial IMs are highly commercialized and economic friendly. It is estimated that almost two-thirds of all the power that has been generated is consumed by the IMs [40]. For marine applications, the technology regarding on the IM, the wound field synchronous machine and the commutator machines are mature enough, while for the other types it is under development [40].

The cost is one of the reasons that IM is preferred by the industry. Such a character is the outcome of its sample and robust structure. Both the rotor and stator of an IM are built of magnetically permeable materials in thin layers and piled up. There are slots to contain conductors. For current applications, most of the IM rotor is with a structure called "squirrel-cage rotor", in which there are no windings but magnetically permeable material bars aligned along auniformly space (Figure 2.3). It is originally called the "bar-winding-rotor" [41].

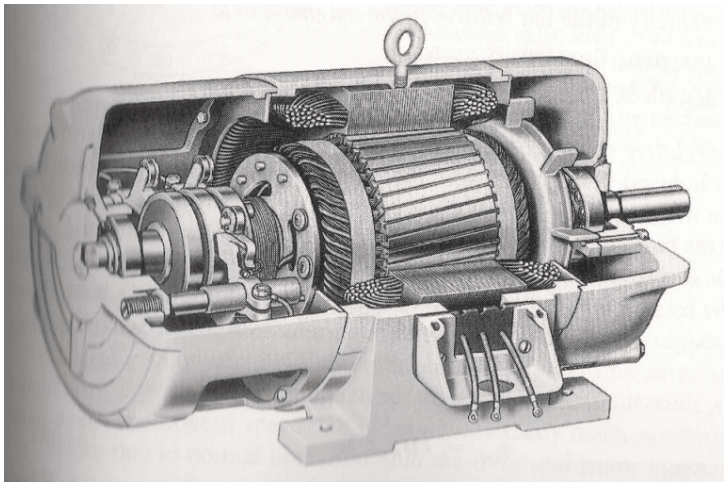

Figure 2.3: Cutway diagram of "squirrel-cage" rotor [42]

The doubly fed induction machine (DFIM) has a rotor winding that is also connected to a converter. The connection is realized with a multi-phase slip ring with brushes. In that case, the rotor frequency is no longer bounded with the stator frequency. In this approach, the DFIG is very suitable for the machine on wind farms, which would require a vast range of operation speeds [43–45]. Similarly, it also well-suited as the generator in the marine applications, which is generally installed on the propeller shaft, the rotor speed changes while the output frequency is required to be constant.

Due to the limited performance in low speed (starting up) or high speed with a heavy load, the conventional marine combustion engines have been installed with an electrically assisted turbocharger (EAT) to increase the torque during the startup and regenerate excessive energy in high-speed [46]. The IM is proved to fit the requirements for an EAT [47].

2.2.2 Mathematical Model of the Induction Machine

The three-phase induction motor model is greatly simplified through the coordinate transformation. Supportive introduction about the reference frame transformation will be included in Section 2.5.1. For the IM model in this section, the $a-b-c$ reference frame is transformed into an $\alpha-\beta$ frame. The mathematical model of IM is written as Equation (2.1) [48].

$$\begin{cases} \frac{d\omega}{dt} = \frac{n_p^2}{J}(i_{s\beta}\psi_{s\alpha} - i_{s\alpha}\psi_{s\beta}) - \frac{n_p}{J}T_L \\ \frac{d\psi_{s\alpha}}{dt} = -R_s i_{s\alpha} + u_{s\alpha} \\ \frac{d\psi_{s\beta}}{dt} = -R_s i_{s\beta} + u_{s\beta} \\ \frac{di_{s\alpha}}{dt} = \frac{1}{\sigma L_s T_r}\psi_{s\alpha} + \frac{1}{\sigma L_s}\omega\psi_{s\beta} - \frac{R_s L_r + R_r L_s}{\sigma L_s L_r} i_{s\alpha} - \omega i_{s\beta} + \frac{u_{s\alpha}}{\sigma L_s} \\ \frac{di_{s\beta}}{dt} = \frac{1}{\sigma L_s T_r}\psi_{s\beta} + \frac{1}{\sigma L_s}\omega\psi_{s\alpha} - \frac{R_s L_r + R_r L_s}{\sigma L_s L_r} i_{s\beta}\omega i_{s\alpha} + \frac{u_{s\beta}}{\sigma L_s} \end{cases} \tag{2.1}$$

where ω is the rotor speed. n_p is the number of pole pairs, ψ is the rotor flux linkage. R and L represents the resistance and the inductance respectively. i and u represents the current and the voltage respectively. The subscripts α β represents that the cooresponding value are in an α β reference frame, while the subscripts s and r represents the stator and the rotor respectively. T_r is the rotor time constant, which is calculated as $T_r = \frac{L_r}{R_r}$. σ is the dispersion coefficient, which is calculated with $\sigma = 1 - \frac{L_m^2}{L_s L_r}$.

Define system states as a vector X, the chosen variables are listed as,

$$X = [w \quad \psi_{s\alpha} \quad \psi_{s\beta} \quad i_{s\alpha} \quad i_{s\beta}]^T \tag{2.2}$$

where the vectors represents the rotor speed, stator flux in $\alpha-\beta$ reference frame, and stator current in $\alpha-\beta$ reference frame respectively

The input matrix U is as Equation (2.3).

$$U = [u_{s\alpha} \quad u_{s\beta} \quad T_L]^T \tag{2.3}$$

where u are the stator voltages in the $\alpha-\beta$ reference frame, T_L is the load torque.

Electric torque for this machine is calculated as Equation (2.4).

$$T_e = n_p(i_{s_\beta}\psi_{s\alpha} - i_{s\alpha}\psi_{s\beta}) \tag{2.4}$$

In a less abstract approach, an induction motor system is described as three coupled subsystems: the magnetic, the mechanical and the electrical system. The relation between the three subsystems are shown in Figure 2.4. When the machine is working as a motor, the input to the whole system is the three-phase voltage, and it is the input of the electrical subsystem. The overall output θ (Rotor angle) is the output of the mechanical subsystem. The electrical and the mechanical subsystem are coupled with the magnetic system. λ_r presents the rotor flux linkage. In addition, the mechanical subsystem impacts the electrical system with the back electromotive force (EMF).

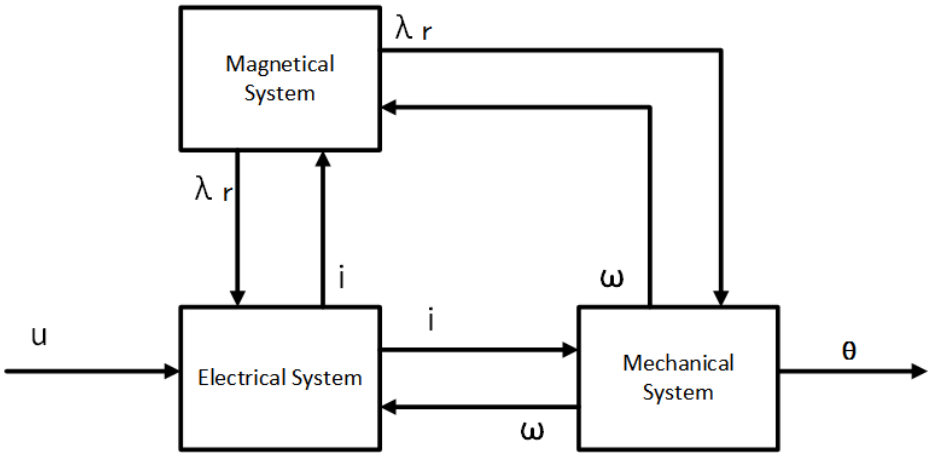

Figure 2.4: Subsystems of an induction motor

2.3 Permanent Magnet Synchronous Machines

The PMSMs are more expensive in contrast to the IM because the rare earth materials. However, it has the advantage of a higher power and torque density, and its performance under a low speed is more promising.

2.3.1 Structures for Rotor-PM Machine

The technologies regarding on the permanent magnet (PM) materials are developing rapidly in recent years. It has been introduced in many types of machines [49]

and classified as the "rotor-PM machine" and the "stator-PM machine" depending on the PM location. The rotor-PM machine is the most famous structure. It has broad applications on the marine propulsion, electric vehicles (EVs) and hybrid EVs (HEVs). Generally speaking, there are three types of rotor-PM machines [50].

- Surface-mounted
- Inset
- Interior

The surface mounted and the interior are the two kinds that most widely used. The difference between them lies in how the PM is placed inside the rotor. Their differences in structure are shown in Figure 2.5. The circle in the figures represents the rotor, while the boxes and arrows show the magnet and its flux linkage flow, respectively. For the SPM, the magnets are located at the rotor surface (Figure 2.5 (a)); for the IPM, the magnets are buried inside the rotor, depending on its position, the type of IPM various (Figure 2.5 (b) and Figure 2.5 (c)). The inset PMSM is similar to the SPM, while the magnets are buried inside(Figure 2.5 (d)).

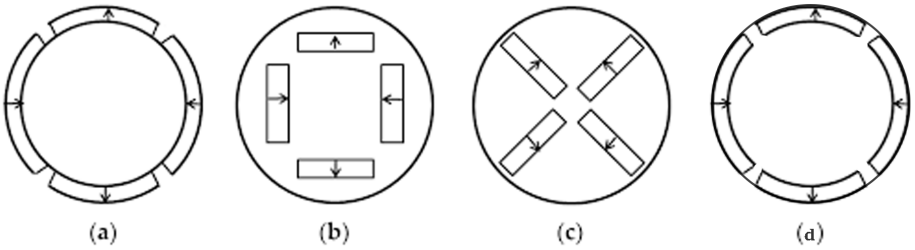

Figure 2.5: Rotor PM structures: (a) SPM; (b) IPM with radial magnetization; (c) IPM with tangential magnetization; (d) Inset PMSM machine [38]

Resulting from their structures, the inductance for d and q axis (L_d and L_q) in the SPM is equal while in the IPM they are not [51]. When the application requiement is searching for the largest torque output of the same current, the working conditions for the SPM and the IPM will be different. In SPM, the stator armature current vector is 90° ahead the rotor flux. In the IPM the angle is larger than 90°, and the machine is working under field weakening. From the cost point of view, the most expensive part in the motors are the rare earth

materials. It will cost about 40% more rare earth materials to build an SPM than an comparable size IPM [52].

2.3.2 Mathematical Model of PMSM

As a synchronous machine, the rotation speed of the PMSM is locked with the input current frequency. With no concern of the slip speed, the mathematical model is less complicated than the IM. Equation (2.5) [53] is the mathematical model of a PMSM. It is shown in a $d-q$ reference frame where $d-axis$ is aligned with the flux direction of the PM located in the rotor.

$$\begin{cases} \frac{d}{dt}i_d = \frac{1}{L_d}v_d - \frac{R}{L_d}i_d + \frac{L_q}{L_d}p\omega_m i_q \\ \frac{d}{dt}i_q = \frac{1}{L_q}v_q - \frac{R}{L_q}i_q - \frac{L_d}{L_q}p\omega_m i_d - \frac{\lambda p\omega_m}{L_q} \\ T_e = 1.5p[\lambda i_q + (L_d - L_q)i_d i_q] \end{cases} \tag{2.5}$$

where L_d and L_q refers to the d and q axis inductions. R refers to the stator resistance. i_d and i_q are the stator current of d and q axis. ω_m is the motor rotor mechanical speed in rad/s. λ is the rotor flux linkage that generated by the permanent magnet, its value usually remains constant and is only affected by the saturation of magnetic materials. p is the machine pole pairs.

2.3.3 PMSM Parameter Measurement

The methods of measuring L_q, L_d, R_s and λ are shown in this section. A 7.7 kW PMSM in the laboratory is applied for the test. The measurement results are utilized for the research in Chapter 4 and Chapter 6.

L_q, L_d and R_s

In an IPM, the inductances L_q, L_d change with the rotor position. The measurement of the inductance cannot be achieved when the machine is standing still. A conventional technique to measure the L_d and L_q is to draw a figure of the phase to phase inductance L_{ab} while manually rotate the rotor angle θ from 0 to 2π in electrical angle degrees [53]. The approximate curve of L_{ab} is drawn as Figure 2.6.

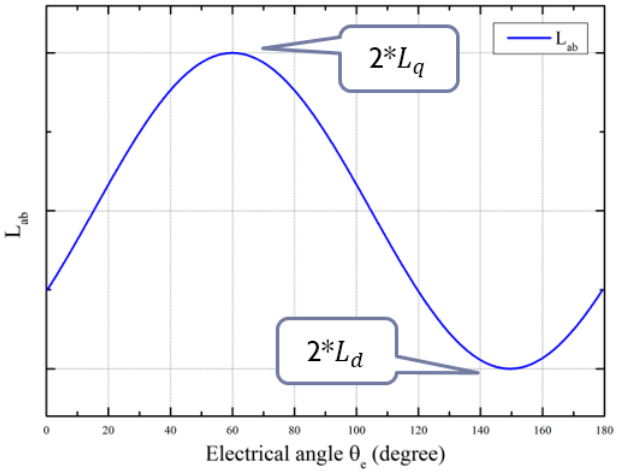

Figure 2.6: Offline measurement of L_d and L_q

The phase to phase results need to be divided by two before the real L_d and L_q value in the mathematical model are calculated (Equation (2.6)).

$$\begin{aligned} L_q &= \frac{max(L_{ab})}{2} \\ L_d &= \frac{min(L_{ab})}{2} \end{aligned} \tag{2.6}$$

The experiment of this test is performed on the 7.7 kW PMSM test rig (Specifications shown in Table 4.1). A Bode 100 vector network analyzer is applied to measure the inductance. Figure 2.7 shows the wire connections with the Bode 100. The cables are lefted on the motor side since in the experiments, the parameters that applied to digital controllers should also count the resistance and inductance of the cables.

The minimal and maximal value of the L_{ab} are logged. The reports generated by the Bode 100 are shown in Figure 2.8. Figure 2.8a shows the minimal value of L_{ab} while Figure 2.8b shows the maximal. The L_{ab} and R_{ab} are read from row "L_s" and "R_s" (Marked with the red boxes). It is observed in Figure 2.8a and Figure 2.8b that the resistance are almost the same. The final R_s is calculated with their average value. A 150 Hz injection source is applied in the test.

With the calculation method in Equation (2.6), the $d-q$ axis inductances are

Figure 2.7: Bode 100 vector network analyzer

as Equation (2.7).

$$\begin{aligned} L_q &= 2.606\ mH \\ L_d &= 1.089\ mH \end{aligned} \tag{2.7}$$

Similarly, the phase stator resistance R_s is found as

$$R_s = 0.176\ \Omega \tag{2.8}$$

Rotor Flux Linkage λ

The rotor flux linkage λ is generated by the permanent magnet. It will remain constant in the normal working conditions. Its value is significant to the PMSM drive design. There is a method that allows to measure λ offline.

This method is based on the back EMF of the machine. A prime mover to the PMSM is required. The prime mover can be either by hand or by another machine. Disconnect the inverter and rotate the machine rotor, when the motor is accelerated, record the motor stator output voltage (back EMF) with an oscilloscope. The experiment is carried on the same machine in Table 4.1. The result is shown in Figure 2.9. Both the frequency and the amplitude of the back EMF are read on a screenshot from the oscilloscope. If the rotor speed is changed

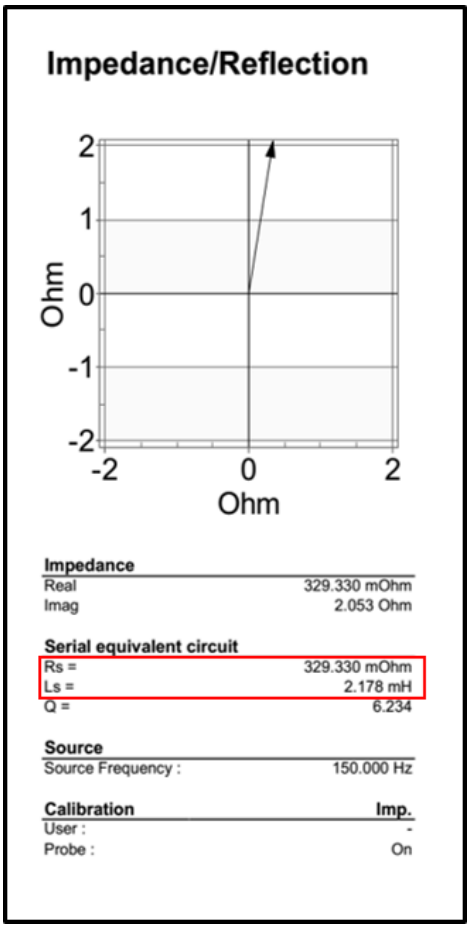

(a) Minimal value of L_{ab}

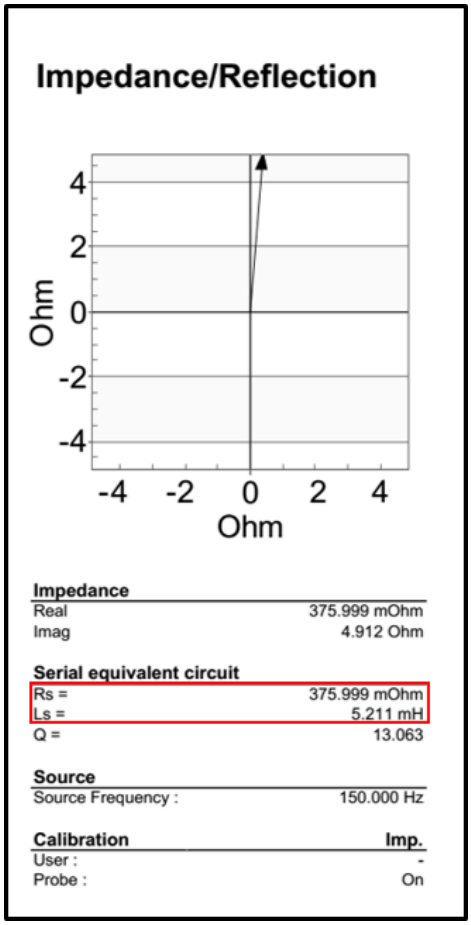

(b) Maximal value of L_{ab}

Figure 2.8: Phase to phase inductance measurement results

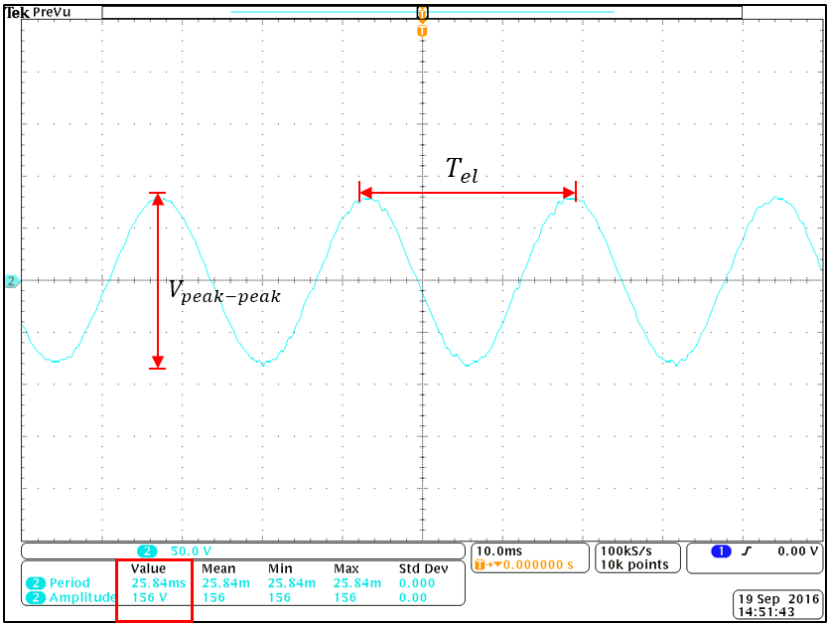

Figure 2.9: Experiment result on PMSM flux offline identification

greatly during the logging process, one should choose a short sampling period so that the matching $V_{peak-peak}$ and T_{el} are logged.

In Figure 2.9, the $V_{peak-peak}$ and T_{el} are marked with the red arrowed lines. The flux linkage λ is identified with Equation (2.9).

$$\lambda = \frac{V_{peak-peak} T_{el}}{4\pi\sqrt{3}} = 0.19735\ wb \tag{2.9}$$

The unit of flux linkage Weber or Wb can be expressed in many approaches. There are Tesla-square meter ($T \cdot m^2$), Volt-second ($V \cdot s$) and Joules per Ampere (J/A).

2.4 Novel Machine Structures

In addition to the IM and the PMSM, many novel machine structures have been proposed. However, due to the economic or robustness reasons, they have not been introduced to marine applications yet. The stator-pm machine, the brushless DC machine (BLDC) and the reluctance machines are briefly introduced in this section.

2.4.1 Stator-PM Machine

The history of the stator-PM machine is dated back to 1955 [54]. Three modern typologies for the stator-PM machine are popular at present. They are doubly salient PM (DSPM), flux reversal PM (FRPM) and flux-switching PM (FSPM) [55].

DSPM is based on the switched reluctance machine with a PM on the stator side [56]. For FRPM, the PM is mounted on the end of the stator windings. Similar to the rotor PM case, the FRPM has a surface mounted PM or an inset PM depends on the direction of PM placed [57]. As its phases are naturally isolated, the fault tolerance for the FRPM is excellent [58]. The stator of a FSPM consists of "U-shaped" magnetic cores with opposite flux directions, the coil is made in a concentrated technique and forms a sandwich structure with the magnets [59]. One advantage of the FSPM is that its phase EMF are naturally sinusoidal [60].

2.4.2 Brushless DC Machine

A PMSM is considered as a brushless AC (BLAC) machine in some literature. The operation of a PMSM requires PWM inverter drives. However, it is difficult for high frequency semiconductors to achieve power ratings as high as 10 MW [61]. In that case, the brushless DC (BLDC) machine is introduced as an alternative choice. The structure of a BLDC is shown in Figure 2.10. Similar with the PMSM, it has permanent magnets as the rotor and windings as the stator.

The brushed motors require a mechanical device called the "commutator" to change the current polarity with the rotor rotation. It brings many disadvantages like friction, voltage drop, fire hazard, and noise [63]. With the development of electronic devices, the mechanical commutator is replaced with a servo system that detects machine angle and switches current direction correspondingly [64].

Both the driven current and the back EMF readings for the PMSM are sinusoidal. For BLDC the signals are trapezoidal shaped pulses. The drive for a BLDC machine does not require a fully-fledged PWM inverter, in that case, the total cost is reduced. In addition, some high frequency harmonics introduced by the PWM switching are prevented.

There are also drawbacks with the BLDC machines. The most significant one is the torque ripple that injected by the phase current commutations [65, 66]. Many approaches have been made to reduce the torque ripple. On the machine

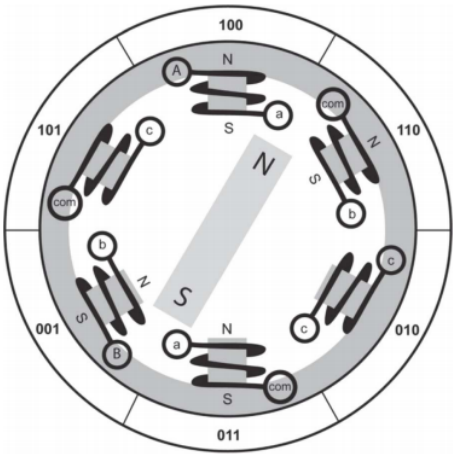

Figure 2.10: BLDC with star connection [62]

design, the connecting wire between the slot windings is considered in [67]. From the controller perspective, the direct torque control (DTC) method [68, 69] have been introduced. Additionally, several works that emphasize the optimization of the reference current signal is reported in [70, 71].

2.4.3 Reluctance Machines

Statistics data shows that about 90% of machines are applied in low power conditions [72], in which area the reluctance machine have a promising performance. The reluctance machine has no windings on the rotor. Its torque is generated by the phenomenon of magnetic reluctance. The switched reluctance motor (SRM) and the synchronous reluctance machine(SyncRel) are widely used types of reluctance machines.

For SRM, the power is delivered to the stator rather than the rotor. In this approach, the design in the mechanical part is greatly simplified, which leads to a lower cost. On the contrary, the electrical design is more complicated. The torque ripple becomes a severe problem when the machine is running in a low speed [73].

The SyncRel is proposed as an ideal replacement for the IM [74] and the PMSM [75]. Its torque density is higher than the IM with lower cost, also it is more efficient since the rotor loss is theoretically zero [76].

2.5 Fundamental Drive for Electric Machines

The fundamentals of electric machine drives are illustrated in this section. To begin with, the reference frame transformation procedures are shown. Next, two popular machine control algorithms, field-oriented control (FOC) and direct torque control (DTC) are introduced.

2.5.1 Reference Frame Transformation

The direct-quadrature-zero ($DQ0$) reference frame transformation is common in electrical engineering, the concept of changing the rotation three-phase AC signal to a DC one greatly simplified the calculation. Reference frame transformation applies to both IM and PMSM drives.

The $DQ0$ reference frame transform is a product of the Clarke and Park transform. The Clarke transform changes the three-phase signal into two phases, and the remain frame stand still, it is proposed by Edith Clarke [77]. The Park transformation, on the other hand, introduces an additional angle θ to the frame, shows the angle between the Park reference frame and the stand-still. With an increasing θ, the rotating reference frame is achieved. If θ is appropriately selected, the three-phase AC signals are turned into two-phase DC signals, which provides more intuitive approach to the researchers. The Park transformation was proposed by Robert Park in 1929 [78].

In the industrial applications, there are two types of $DQ0$ reference frame transforms, which are the power-invariant form and the power-variant form. Different refernece frames lead to different definitions of $d-q$ signals and further changes the corresponding torque equations.

Power-invariant Form

The idea behind the power-invariant form is described with Equation (2.10). In which, the i and u are the current and voltage vectors, i' and u' are the transformation results. It is shown in equation (2.10), the i and u are vectors, the T in i^T stands for matrix transpose. The calculated powers are preserved before and after the transformation.

$$P = i^T u = i'^T u' \tag{2.10}$$

The $abc \rightarrow dq$ transformation is as Equation (2.11) [79].

$$\begin{bmatrix} x_d \\ x_q \end{bmatrix} = \sqrt{\frac{2}{3}} \begin{bmatrix} \cos\theta & \cos(\theta - 2\pi/3) & \cos(\theta - 4\pi/3) \\ -\sin\theta & -\sin(\theta - 2\pi/3) & -\sin(\theta - 4\pi/3) \end{bmatrix} \begin{bmatrix} x_a \\ x_b \\ x_c \end{bmatrix} \tag{2.11}$$

In Equation (2.11), the meaning of x various. It can be the current, the voltage or the flux linkage. θ presents the misalignment between the a-axis in the abc reference frame and the d-axis in dq reference frame. In the electric machine background, if the θ angle is set exactly aligned with the rotor flux linkage vector, the decoupled d-axis vectors x_d will contribute to the flux, while the q-axis vectors x_q will be perpendicular to the rotor flux, which means the useful current vector who generates the electric torque.

Similarly, the reversed frame transformation is also required in the control process, that is after the output x_d and x_q are calculated through the controller, it needs to be transformed to the abc reference frame and sent to the machine, the $dq \rightarrow abc$ transformation is shown in Equation (2.12) [79].

$$\begin{bmatrix} x_a \\ x_b \\ x_c \end{bmatrix} = \sqrt{\frac{2}{3}} \begin{bmatrix} \cos\theta & -\sin\theta \\ \cos(\theta - 2\pi/3) & -\sin(\theta - 2\pi/3) \\ \cos(\theta - 4\pi/3) & -\sin(\theta - 4\pi/3) \end{bmatrix} \begin{bmatrix} x_d \\ x_q \end{bmatrix} \tag{2.12}$$

Take the IM as an example, with the i_{qs} and the flux Φ from the power-invariant frame transformation, the electric torque equation is written as

$$T_e = n_p \frac{L_m}{L_r} i_{qs} \Phi \tag{2.13}$$

In a PMSM, the torque equation is

$$T_e = n_p \left(\Phi_m i_q + (L_d - L_q) \, i_d i_q \right) \tag{2.14}$$

Power-variant Form

The power variant form transformation is also called a magnitude invariant form in some literature. As shown in Equation (2.15), the system D-axis vector is defined to share a same direction and a same magnitude with the A-axis.

$$x_d = x_a \tag{2.15}$$

The $abc \rightarrow dq$ transformation in power-variant form is shown as Equation (2.16) [79].

$$\begin{bmatrix} x_d \\ x_q \end{bmatrix} = \frac{2}{3} \begin{bmatrix} \cos\theta & \cos(\theta - 2\pi/3) & \cos(\theta - 4\pi/3) \\ -\sin\theta & -\sin(\theta - 2\pi/3) & -\sin(\theta - 4\pi/3) \end{bmatrix} \begin{bmatrix} x_a \\ x_b \\ x_c \end{bmatrix} \tag{2.16}$$

The definition of x and θ in Equation (2.16) remain consistent with Equation (2.11). The difference lies in the coefficient $\sqrt{\frac{2}{3}}$ before the matrix.

In a per-unit system where the i_b and u_b are defined by the magnitude of the phase voltage and current, the same coefficient $\sqrt{\frac{2}{3}}$ is also employed to convert the actual value to a per-unit value. It is applied here because one may consider the power variant system as a per unit system with the phase voltage and current as the base.

The reversed frame transformation is shown in Equation (2.17) [79].

$$\begin{bmatrix} x_a \\ x_b \\ x_c \end{bmatrix} = \begin{bmatrix} \cos\theta & -\sin\theta \\ \cos(\theta - 2\pi/3) & -\sin(\theta - 2\pi/3) \\ \cos(\theta - 4\pi/3) & -\sin(\theta - 4\pi/3) \end{bmatrix} \begin{bmatrix} x_d \\ x_q \end{bmatrix} \tag{2.17}$$

The electric torque equation of an IM under the power-variant frame transformation is written as

$$T_e = \frac{3}{2} n_p \frac{L_m}{L_r} i_{qs} \Phi \tag{2.18}$$

As in PMSM, the torque equation is like

$$T_e = \frac{3}{2} n_p \left(\Phi_m i_q + \left(L_d - L_q \right) i_d i_q \right) \tag{2.19}$$

In the simulation model and the hardware experiment, power variant and invariant transformations may mixed up. A common mistake is to apply wrong equations for the torque calculation, the resulting differences are usually beyond the controller's capability to fix.

2.5.2 Field-Oriented Control

The field-oriented control (FOC) is developed based on the idea of reference frame transformation. FOC is also called as the vector control in some literature. Although there are other vectors are applied as well, the vector in FOC is generally referred to the rotor flux vector.

A control method that suitable for the industrial standard must have superior dynamic performance and the capability of being implemented on a digital processor efficiently [79]. For the FOC, its implementation is simple and reliable as long as the rotor flux direction is appropriately identified. Regarding how to find the rotor flux direction, FOC is categoried as direct FOC (DFOC) and indirect FOC (iFOC).

The dFOC finds the rotor flux with the stator current and voltage. The stator flux is derived with Equation (2.20) [79].

$$\overrightarrow{\lambda_s} = \int \left(\overrightarrow{v_s} - R_s \overrightarrow{i_s} \right) dt \tag{2.20}$$

where the stator flux λ_s is calculated with the stator voltage v_s, the stator current I_s and the stator resistance R_s.

Next, the rotor flux λ_r in the dq reference frame is found with Equation (2.21) [79].

$$\begin{aligned} \lambda_{dr} &= \frac{L_r}{L_m} \left(\lambda_{ds} - \sigma L_s i_{ds} \right) \\ \lambda_{qr} &= \frac{L_r}{L_m} \left(\lambda_{qs} - \sigma L_s i_{qs} \right) \end{aligned} \tag{2.21}$$

where the λ_{ds} and λ_{qs} are the stator flux decoupled into a dq reference frame. L_r and L_M are the rotor and mutual inductance respectively. σ is the dispersion coefficient, which is calculated with $\sigma = 1 - \frac{L_m^2}{L_s L_r}$.

The problem with the DFOC is in the measurement of the stator voltage and current. In industrial applications, the three-phase stator current measurement is influenced by the sensor resolution and the signal transition latency. In addition, the stator voltage is in PWM signal, whose accuracy is compromised when restored to a continuous signal. The measurement error in both current and voltage will be amplified by the integral calculations in the DFOC. As a result, the overall performance of the DFOC is not reliable.

On the other hand, the indirect FOC (iFOC) obtains the rotor flux direction through calculation of the slip speed. It works as a more accessible approach to the industry.

The overall configurations of i-FOC for the IM and PMSM respectively are shown in Figure 2.11 and Figure 2.12. A typical machine control consists of a speed loop and a current loop. As discussed in Section 2.5.1, with a proper decoupling of the d-q axis, the current vector i_q that influences the generated torque is controlled directly. In Figure 2.11, the speed loop has the rotor speed as the reference value and the feedback. The output is either the torque reference or the i_q reference since those two have proportional relationships. On the other hand, the i_d reference is calculated based on the flux reference. The dynamic between the rotor flux to i_d is as Equation (2.22). As the flux reference is normally constant in the whole control process, the dynamic can be simplified as Equation (2.23). In some literature when the flux is not constant, an additional flux loop is applied to generate a more accurate i_d reference.

$$\lambda_r = \frac{1}{1 + \tau_r s} L_m i_{ds}^* \tag{2.22}$$

$$i_{ds}^* = \varphi^* / L_m \tag{2.23}$$

The current loop works as the inner loop of the speed loop. Its goal is to maintain the current feedback tracking the reference. It should be noted that the reference and feedback in the current loop are in dq frame. However, the decoupling of dq current requires the slip angle which needs the current i_q to find. In that perspective, a dq misalignment may caused. Fortunately, the structure of an IM is robust enough for a misalignment in a certain range. There will be a comprehensive discussion on this issue in Chapter 5. For PMSM, the misalignment is also possible due to the encoder failure or time delay in the sensorless control.

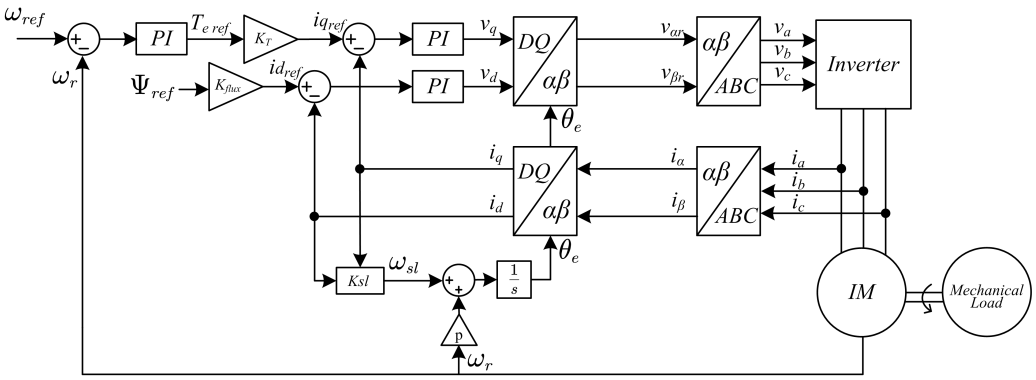

Figure 2.11: System configuration of indirect FOC: IM [79]

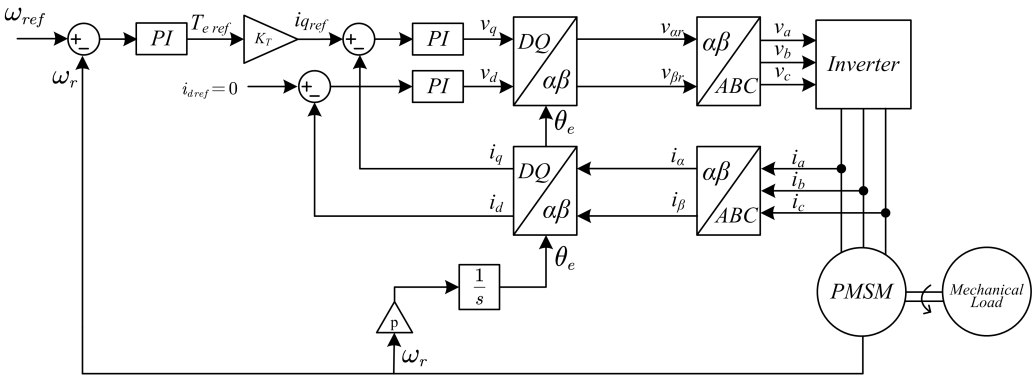

Figure 2.12: System configuration of indirect FOC: PMSM [53]

2.5.3 Direct Torque Control

The direct torque control(DTC) focus on another expression of the electric torque generated, expressed as Equation (2.24) [79].

$$T_e = \frac{3P}{2}\frac{L_m}{\sigma L_s L_r}\lambda_s \lambda_r \sin\theta_T \tag{2.24}$$

where θ_T represents the angle between λ_s and λ_r. In Equation (2.24), vector $\overrightarrow{\lambda_s}$ is related to the stator voltage vector $\overrightarrow{v_s}$ as

$$s\overrightarrow{\lambda_s} = \overrightarrow{v_s} - R_s\overrightarrow{i_s} \tag{2.25}$$

Equation (2.25) shows that the magnitude and angle of $\overrightarrow{\lambda_s}$ is adjustable through stator voltage vector $\overrightarrow{v_s}$, who is the output of the inverter that connected to the IM.

Take a typical two-level VSI fed IM drive as an example. The voltage vectors are divided into six sectors, labeled from I to VI, the voltage vectors are as $\overrightarrow{v_1}$ to $\overrightarrow{v_6}$. Note the time interval for single voltage vector as Δt. The influence of a voltage vector on the individual time interval is shown as Equation (2.26).

$$\overrightarrow{\lambda_s}' = \overrightarrow{\lambda_s} + \overrightarrow{V_x}\Delta t \tag{2.26}$$

On the other hand, the change of $\overrightarrow{\lambda_r}$ is much slower than $\overrightarrow{\lambda_s}$. Thus, $\overrightarrow{\lambda_r}$ is considered as constant during Δt. Selecting an appropriate voltage vector controls $\overrightarrow{\lambda_s}$ and θ_T means the torque is directly controlled.

The DTC have both advantages and disadvantages compared to the FOC [80]. Generally, the DTC scheme is simple. No field orientation is required means the installation of an encoder is not compulsory. Additionally, the stator current control is not required. At the same time, the torque response of the DTC is better than the FOC when the encoder is not available. On the contrary, FOC has better accuracy in both the torque and speed responses with the help of an encoder.

2.6 Summary

In this chapter, the background knowledge about the electric ship and on-deck electric machines are reviewed.

More electric ship and all electric ship are the trends for the ship development. In recent years, the technology about electric ships has been developing rapidly in both civil and military domains.

General electric ships would carry a shipboard power system and propellers powered by electric machines. The electric propulsion system has many advantages like efficiency, flexibility, and safety.

The core component for the electric propulsion system and the deck machinery module are the electric machines. In this chapter, IMs and PMSMs are comprehensively introduced. They are two of the most popular types of machines in the marine application. In addition, the research in this thesis is based on these two types.

In the last section, the fundamental knowledge about the electric machine drive is provided. The reference frame transformation methods are introduced as the foundation of machine drives. Next, the configuration of two common control algorithms, FOC and DTC, are shown.

The following chapters, Chapter 3 to Chapters 6 are focused on solving the present challenges of electric machines in marine applications. The optimal reset control is applied in Chapter 3 to improve the dynamic response. The equation deduction processes are shown, the simulation and hardware results are presented.

Chapter 3

Optimal Reset Controller

This chapter focuses on the dynamic response for marine electric machines. Complexity is a dominant feature of the maritime environment, which result from varying conditions of ocean currents, waves and wind [27]. Driven by the same factors, higher accuracy in speed reference trajectory tracking is always preferred.

To begin with, the background is reviewed for the present electric machine speed controller. Next, a novel control algorithm named the optimal reset controller (ORC) is introduced to improve trajectory tracking. This method is applied to the speed loop control of electric machines. The simulation results are shown. Then hardware in the loop (HIL) test and hardware test on a 15 kW induction machine (IM) are investigated.

Table 3.1: Comparison of simulation, HIL and hardware test

Method (Section No.)	Controller	Plant
Simulation (3.4)	SIMULINK (PC)	SIMULINK (PC)
HIL test (3.5)	DSP	Opal-RT
Hardware test (3.6)	DSP	3-phase inverter and 15 kW motor

A comparison between simulation, HIL test, and hardware test is made in Table 3.1. For all the tests there are controller and plant. In the simulation, both are modeled and run on software platform like PC. On the other hand, in HIL test, the plant (i.e., motor and inverter) is modeled with an OP5600 Opal-RT real-time digital simulator, while the controller uses a digital signal processor (DSP). "Real-time" in this context refers to the communication between DSP

and Opal-RT are synchronized in real clock time. HIL can perform more realistic simulation in this approach. The main body of the code in a HIL test can be applied to the hardware test without any further modification. In the hardware test, a 15 kW IM controlled with SEMIKORN inverter is applied.

3.1 Industrial Machine Speed Drives

In industrial applications, proportional plus integral (PI) controllers are widely used due to their straightforward operation [81]. In addition, much effort has been spent on finding the optimal PI gain. Mostly, the approach requires knowledge of the mathematical model of the working condition of the controller plant [82]. Swarm optimization [83] and artificial neural networks [84] have been introduced to make a self-tuning PI algorithm. For model-based tuning methods, the major drawback is that these methods may become less reliable when the machine parameters are uncertain. Based on that concept, model-free methods are developed later. In [85–87], a self-tuning fuzzy algorithm is applied to the control strategy of various types of motors. Advanced methods inevitably lack the PI controller's straightforward operation, thus strengthening the foundation of the PI controller in industrial applications. Beside the model parameter variations, the sensor output as the feedback signal is also important to the controller performance. A method to counter sensor fail of the IM is proposed in [88].

When applied to electric machines, a typical control system scheme is a cascaded dual-loop PI controller based on vector control or field oriented control (FOC) [89]. the scheme for an IM is shown in Figure. 2.11 and PMSM in Figure. 2.12. For the outer loop (speed loop), many advanced control algorithms have been applied. Sliding-mode control (SMC) is applied to improve the system robustness and accommodate system uncertainties [90–92]. An optimal controller is applied for the IM FOC scheme in [93]. Additionally, an optimal law is employed to find the largest stability region for a reduced-order observer in [94]. Furthermore, the model reference adaptive system (MRAS) observer-based method is implemented in [95–97]. Its stability and dynamic performance have been proven.

3.2 Optimal Reset Controller

In both traditional PI control schemes and linear advanced control algorithms, a tradeoff between the response speed and overshoot is unavoidable, as it is rooted in

the nature of the controller. To overcome this limitation of linear controllers [98], the concept of the reset controller has been proposed [99,100] and developed [101]. In the reset controller, the states are reset to a certain value at a particular time to obtain a control result that is not viable in the linear controller. The stability analysis was carried out in later publications [102, 103]. In contrast to the other nonlinear control strategies (e.g., sliding mode control, relay control), the control law for reset control is consistent on both sides of the switching surface [104]. In other words, the reset controller works as a linear system with continuously updated state information. The advantages of the reset controller are presented in [105], and the improvement is shown with an elementary example.

Many continuous works have been carried out on the conventional reset controller. The stability analyses of conventional reset controller and first-order reset element (FORE) are given in [106]. In [107], a reset controller with fixed reset step is investigated and implemented to a networked control system. The reset value is calculated to minimize the quadratic performance index on the signal error. A later paper [108] focuses on finding the tuning method of the reset parameters. The stability of the reset time-dependent control system is discussed in [109]. When the base control system cannot achieve its best performance without reset controller, the system stability analysis becomes a time-varying discrete time problem, whose reset time must set in a bounded interval. In [110], the reset controller has been introduced into multi-input multi-output (MIMO) system. Besides, a method of manual reset is introduced to air-conditioning control system in [111].

The ORC was first proposed in [112]. The maintains constant reset intervals, which is different from the traditional reset controllers. An optimal operation strategy would suggest that for each time interval, the reset state be calculated based on a certain performance index to ensure the optimized controller output. In a later work [113], the performance index is expanded to the whole time interval instead of only the following one in [112]. It is proven that the system is asymptotically stable with the designed reset law. In [112] and [113], an ORC is applied to the track-seeking process in a hard disk drive (HDD), and the dynamic performance is significantly improved. In [114,115], where the reset law is applied to a discrete time solution, an ORC is introduced to a dual-stage HDD drive. In [116], an ORC is further applied to the current loop control of PMSMs, and the uncertainty estimation issue is illustrated in particular.

3.3 Optimal Reset Law Design

The method of implementing ORC to electric machine speed control is introduced in this section. The system model is shown in Figure. 3.1. Here, ω_r represents the machine rotor speed feedback, while ω_r^* is the rotor speed reference, the error between them would be the input of the speed controller. The output of the speed controller is electrical torque reference T_e^*. As the current loop bandwidth is much larger than the speed loop bandwidth, the difference between T_e and T_e^* is ignored. The machine model is written as $\frac{1}{Js+B}$. T_L represents the load torque, which is considered as the disturbance in this case.

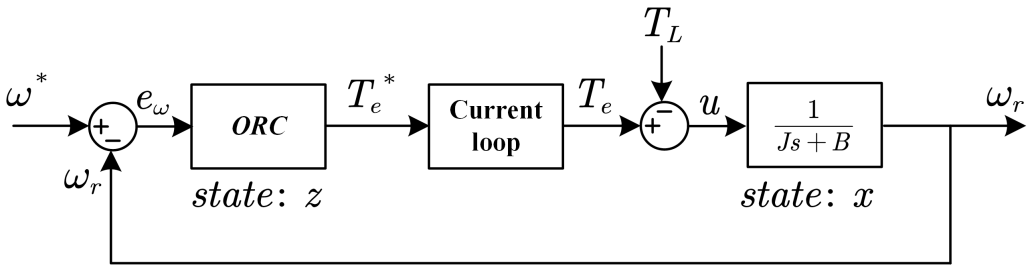

Figure 3.1: Configuration of ORL for electric machines

The "ORC" box in Figure. 3.1 is the optimal reset controller, which consists of a base linear controller (PI controller) and an optimal reset law. The equation for the ORC is designed as Equation (3.1).

$$\begin{cases} \dot{z} = e_\omega & t \neq t_k \\ z(t^+) = \rho_k(z, r) & t = t_k \\ u = k_i z + k_p e \end{cases} \tag{3.1}$$

where k_p and k_i are the PI controller parameters and ρ_k, or the reset law, is defined as

$$\rho_k = -K\left(x\left(t_k\right) - x_r\right) + z_r \tag{3.2}$$

Equations (3.1) and (3.2) describe the structure of a optimal reset law. $t_k(k = 1, 2, 3, ...)$ here refers a time series with equal intervals. When t equals to t_k, z is reset to an optimal value according to the reset law, otherwise the controller output follows the base linear controller. r in the subscript refers the to steady-

state value of the cooresponding parameters x and z.

Industrial implemention of the ORC is concluded in the following procedure. Firstly, take the PI controller parameters k_p and k_i designed for a particular controller and introduce them as the base liner controller. Next, calculate the parameters for the optimal reset law (Equation (3.2)). In particular, the optimal parameter K, the steady-state value z_r and the cost function weight Q and R are the parameters to identify. Lastly, the ORC in a form of Equation (3.1) is introduced as the speed controller replacing the original PI controller.

The methods of identifying the essential parameters are discussed in Section 3.3.1 to Section 3.3.4, with a more specific example given in Section 3.6. The effectiveness of ORC is proved through simulations (Section 3.4) and experiments (Section 3.6).

3.3.1 Base System k_p and k_i

The conventional design of PI parameters in the electrical machine speed loop depends on the machine mechanical parameters. The design should be robust while drawing a compromise between the dynamic response and overshoot. Due to the existence of the reset controller, the requirements for designing the base linear system with PI parameters are less strict than in other cases. There are several points that need to be highlighted.

First, a more aggressive setting of k_p and k_i is suggested. With the help of the reset controller, the benefit of dynamic performance is kept while the overshoot is eliminated.

Second, in the definition of the reset law, the controller output u in Fig. 3.1 is the electric torque. However, if the q-axis current is chosen as output, an additional gain k_g is multiplied to k_p. For the IM and PMSM, the gains are (3.4)and (3.6), respectively.

For IM,

$$T_e = \frac{3}{2} n_p \frac{L_m}{L_r} i_{qs} \Phi \tag{3.3}$$

$$k_g = \frac{3}{2} n_p \frac{L_m}{L_r} \Phi \tag{3.4}$$

As in PMSM, the torque equation is like

$$T_e = \frac{3}{2} n_p \left(\Phi_m i_q + \left(L_d - L_q \right) i_d i_q \right) \tag{3.5}$$

$$k_g = \frac{3}{2} n_p \Phi_m \tag{3.6}$$

Here, $(L_d - L_q) i_d i_q$ is relatively small.

Third, during the reset law design, the PI controller parameters are put in a continuous form. In this approach, the value of $k_i k_p$ is influenced. However, in hardware implementation, k_i should be transferred to the discrete time form depending on the time intervals.

The basic idea behind the above-stated three points is to ensure that the optimal law design is aligned with the base controller.

3.3.2 Optimal Parameter K

The optimal problem is solved as a standard LQR problem. The optimal law parameter K is found by solving the Riccati equation in an LQR problem.

First, the state-space model for the speed loop transfer function is presented as

$$\begin{cases} \dot{x} = -\frac{B}{J} x + \frac{1}{J} u \\ y = x \end{cases} \tag{3.7}$$

A new system is rewritten as Equation (3.8), which is a combination of Equation (3.7) and Equation (3.1).

$$\frac{d}{dt} \begin{pmatrix} x \\ z \end{pmatrix} = \begin{pmatrix} -\frac{B}{J} - \frac{k_p}{J} & \frac{k_i}{J} \\ -1 & 0 \end{pmatrix} \begin{pmatrix} x \\ z \end{pmatrix} + \begin{pmatrix} k_p \\ 1 \end{pmatrix} r \tag{3.8}$$

As shown in Figure. 3.1, x and z represents to the state of the speed loop plant and the reset controller respectively. The system matrices A and B are defined as Equation (3.8) to set up a general form of the LQR problem.

$$A = \begin{pmatrix} -\frac{B}{J} - \frac{k_p}{J} & \frac{k_i}{J} \\ -1 & 0 \end{pmatrix}, B = \begin{pmatrix} k_p \\ 1 \end{pmatrix} \tag{3.9}$$

Next, a coordinate transform is applied. Compare x and z to their reference values x_r and z_r to enable ζ_x and ζ_z to be found, respectively.

$$\begin{cases} \zeta_x = x - x_r \\ \zeta_z = z - z_r \end{cases} \tag{3.10}$$

Define $\zeta = \begin{pmatrix} \zeta_x \\ \zeta_z \end{pmatrix}$

Equation (3.8) is transferred into

$$\begin{cases} \dot{\zeta} = A\zeta & t \neq t_k \\ \zeta_z\left(t_k^+\right) = \overline{\rho} & t = t_k \end{cases} \tag{3.11}$$

where $\overline{\rho_k} = \rho_k - z_r$.

A cost function is defined as Equation (3.12). The purpose for optimization is to find an optimal value of K, which will lead to a minimal value of J_k within a single reset interval t_k to t_{k+1}.

$$J_k = \oint_{t_k}^{t_{k+1}} \left[e_\omega^T(s) Q_k e_\omega(s) + (u(s) - u_r)^T R_k (u(s) - u_r) \right] ds \tag{3.12}$$

According to the coordinate transformation, the following equations are achieved.

$$\begin{cases} e_\omega = -\zeta_x \\ u = K_p e_\omega + K_i z \\ u - u_r = -K_p \zeta_x + K_i \zeta_z \end{cases} \tag{3.13}$$

Substituting Equation (3.13) into Equation (3.12), The performance index of

single reset interval is acquired.

$$J_k = \int_{t_k}^{t_{k+1}} [\zeta_x{}^T(s) Q_k \zeta_x(s) + (-K_p\zeta_x + K_i\zeta_z)^T R_k(-K_p\zeta_x + K_i\zeta_z)]ds \tag{3.14}$$

Define

$$\xi\left(t_{k+1}\right) = e^{A\triangle t_k}\xi\left(t_k^+\right) \tag{3.15}$$

$$\Theta_k = \int_0^{\Delta t_k} e^{A^T\Delta t_k}\Omega_k e^{A\Delta t_k}ds \tag{3.16}$$

$$\Omega_k = \begin{pmatrix} Q_k + (-Kp)^T R_k\left(-Kp\right) & (-Kp)^T R_k Ki \\ (-Kp)^T R_k Ki & Ki^T R_k Ki \end{pmatrix} \tag{3.17}$$

where e is the base of the natural logarithm, the cost function Equation (3.14) is rewrite as

$$J_k = \begin{pmatrix} \zeta_x(t_k^+) \\ \zeta_z(t_k^+) \end{pmatrix}^T \Theta_k \begin{pmatrix} \zeta_x(t_k^+) \\ \zeta_z(t_k^+) \end{pmatrix} \tag{3.18}$$

In the infinite time case, the cost function $J(\infty)$ is the sum up of J_k in all time intervals. The goal of optimization is to design the control sequence $\overline{\rho}_k$ to minimize the performance index of $J(\infty)$, while the system is asymptotically stable Additionally, Q_k and R_k are the cost function weights, whose design will be discussed in Section 3.3.4. Ω_k is a constant that is calculated with Q_k, R_k and some system parameters. Thus, the value of Θ_k is constant throughout the whole process, and its subscript k can be removed $\Theta_k = \Theta$, $k = 0, 1, ..., N-1$. In addition, as $\overline{\rho_k} = \rho_k - z_r$ and $\zeta_z = z - z_r$. The quadratic performance index becomes Equation (3.19). The controller goal is to design a control sequency ρ_k, $k = 0, 1, ..., N-1$ so that Equation (3.19) is minimized.

$$\mathrm{J}\left(\infty\right) = \sum_{k=0}^{\infty}\left(\zeta_x(t_k)^T\overline{\rho_k}^T\right)\Theta\begin{pmatrix}\zeta_x\left(t_k\right) \\ \overline{\rho_k}\end{pmatrix} \tag{3.19}$$

The next step is finding the optimal parameter K through the Riccati equations so that $\mathrm{J}\left(\infty\right)$ in the cost function Equation (3.19) is minimized.

Calculate the value of $e^{A\Delta t_k}$, and define Γ_A and Γ_B as in Equation (3.20).

$$e^{A\Delta t_k} = \begin{pmatrix} \Gamma_A & \Gamma_B \\ * & * \end{pmatrix} \tag{3.20}$$

Additionally, Θ is defined as $\Theta = \begin{pmatrix} \bar{Q} & \bar{T} \\ \bar{T}^T & \bar{R} \end{pmatrix}$,

Calculate $\bar{\Gamma}_A$ and $\tilde{Q}$ with

$$\bar{\Gamma}_A = \Gamma_A - \Gamma_B \bar{R}^{-1} \bar{T}^T \tag{3.21}$$

$$\tilde{Q} = \bar{Q} - \bar{T}\bar{R}^{-1}\bar{T}^T \tag{3.22}$$

S is the solution of Riccati Equation (3.23).

$$\mathrm{S} = \tilde{Q} + \bar{\Gamma}_A^T S \bar{\Gamma}_A - \bar{\Gamma}_A^T S \Gamma_B \left(\Gamma_B{}^T S \Gamma_B + \bar{R}\right)^{-1} \Gamma_B{}^T S \bar{\Gamma}_A \tag{3.23}$$

K is calculated with Equation (3.24) substituting the solution of S in Equation (3.23) .

$$K = \left(\Gamma_B{}^T S \Gamma_B + \bar{R}\right)^{-1} \left(\Gamma_B{}^T S \Gamma_A + \bar{T}^T\right) \tag{3.24}$$

The minimum value of the quadratic performance index is given as

$$J^*(\infty) = \left(x(0) - x_r\right)^T S \left(x(0) - x_r\right) \tag{3.25}$$

3.3.3 Steady State z_r

In the PI controller, the integral state value works as feedback to the system disturbances. To properly implement the reset law to the integral state, compensation needs to be made for the potential disturbances. Taking the electric machine speed loop controller as an example (see Fig. 3.1), the major disturbance to the system is expected to be the load torque (T_L) and fraction (fraction factor B multiplies by the rotor mechanical speed ω_r). Considering the steady state, when $\omega_r^* = \omega_r$, the state is $z = z_r$. In addition, z_r is found as Equation (3.26).

$$z_r = \frac{Bx_r + T_L}{k_i} \tag{3.26}$$

In Equation (3.26), load torque T_L need to be found with a simple observer

based on Equation (3.27). The observer is connected to a low pass filter in the hardware test.

$$T_L = T_e - B\omega - J\frac{d\omega}{dt} \tag{3.27}$$

In [116], the observer applied for the current controller is discussed thoroughly. As the major disturbance in the current loop is the coupling between the d-q components, control success depends relatively strongly on the observer. In the speed loop control, the disturbance changes at a slower rate. In hardware tests, a lowpass filter (LPF) is necessary against noise in the sensors. Here, an LPF with a cutoff frequency of $\omega_c = 2.5\ rad/s$ is applied. It is proven in the experimental results that the load torque observer design with Equation (3.27) is sufficient.

3.3.4 Cost Function Weight Q and R

The cost function is defined in Equation (3.12). In the cost function, the controller error and input are the two factors set for Linear-quadratic tracker. Q_k is the weight for error e and R_k is the weight for input signal u. The selection of Q and R will influence the calculated optimal law gain K in Equation (3.2). Regarding the physical meaning, Q represents how important the system error is to the final result, while R represents a weighting to apply as little energy as possible to achieve the control result. As weight factors, the absolute values of Q and R are not important. It is their ratio $\frac{Q}{R}$ that matters. A series of $\frac{Q}{R}$ values are sent to calculate the offline reset law parameter, and the results are compared in Fig. 3.2.

For the speed loop control, the trajectory tracking error is much more important than the energy. In Fig. 3.2, the optimal gain K is shown. It is calculated with $\frac{Q}{R}$ in the range of 20 to 50. The result shows that reset law gain K is linear to $\frac{Q}{R}$. Additionally, the results with $Q = 10$ and $Q = 100$ as base values are calculated. The result shows that the $Q = 10$ and $Q = 100$ curves overlap, which means that the value of Q does not impact the reset law gain.

In the hardware tests, $R = 0.03 * Q$ is selected as the cost function weight ratio.

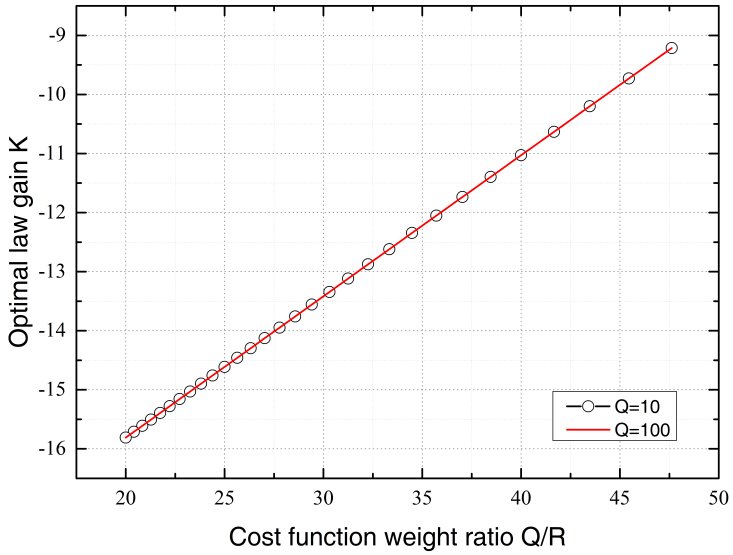

Figure 3.2: Calculation result of different Q-R ratio

3.4 Simulation Results

A simulation is carried out with Matlab Simulink. For comparison to hardware results in later section, the model uses the matching parameters with the 15 kW IM test rig. The motor parameters are presented in Table 3.2.

In the simulation, the test is carried out on both traditional PI controller and the ORC.The PI parameters for the traditional PI controller has been calculated with the machine mechanical parameters, with the damping ratio $\xi = 0.707$ and the natural frequency $\omega_n = 10\ rad/s$, $k_p = 1.96$ and $k_i = 14.00$. The motor reference speed is set to 600 rpm with an acceleration ramp of 600 rpm/s. Load torque of 10 Nm is added after the rotor speed is stabilized. In that case, the controller performance in sudden load change is tested.

The speed tracking performance for both controllers are compared in Figure 3.3a and Figure 3.3b. The following observations are made.

- The error between the reference and feedback speed for both conditions are shown in Figure 3.3a and Figure 3.3b. For PI controller in Figure 3.3a, the maximal error is about 40 rpm, while the same for ORC (Figure 3.3b) is reduced to 20 rpm.

Table 3.2: Specifications of the 15kW IM

Specifications	**Value**
Rated power	15 kW
Stator voltage	415 V
Stator current	28 A
Rotor resistance R_r	0.2212 Ω
Stator resistance R_s	0.2788 Ω
Stator leakage inductance L_{ls}	2.814 mH
Rotor leakage inductanceL_{lr}	3.719 mH
Mutual inductanceL_m	82.130 mH
Moment of inertia J	0.14 kg.m^2
Friction factor B	0.01 N.m.s
Pairs of poles	2

- At $t = 1s$, when the shape turn is made on the reference, overshoot on ORC feedback is removed immediately, showing the signature of a non-linear controller. On the other hand, with PI controller, overshoot is eliminated in a longer process.
- At $t = 2.5s$, load change of $+10Nm$ is applied to both conditions. On PI controller, the speed error induced by sudden load change is about 5 rpm. On the ORC case, torque tracking is smooth, and the speed change induced by load change is neglectable.

The torque curves are shown in Figure 3.4. The electric torque is the blue curve, and the load torque is red. Nonlinear characteristic of ORC is observed at both acceleration period ($t = 0\ s\ to\ t = 1\ s$) and load change period ($t = 2.5s$) . The electric torque response in Figure 3.4b is stabilized at around 45 Nm, while for traditional PI controller in Figure 3.4a the electric torque is changing rapidly with the system dynamic response. In sudden load change at $t = 2.5s$, the difference is more obvious. the electric torque is tracking the load torque for Figure 3.4b while in Figure 3.4a a 50% overshoot (5 Nm) is observed.

In Section 3.5 and Section 3.6. Further experiment results of ORC are shown,

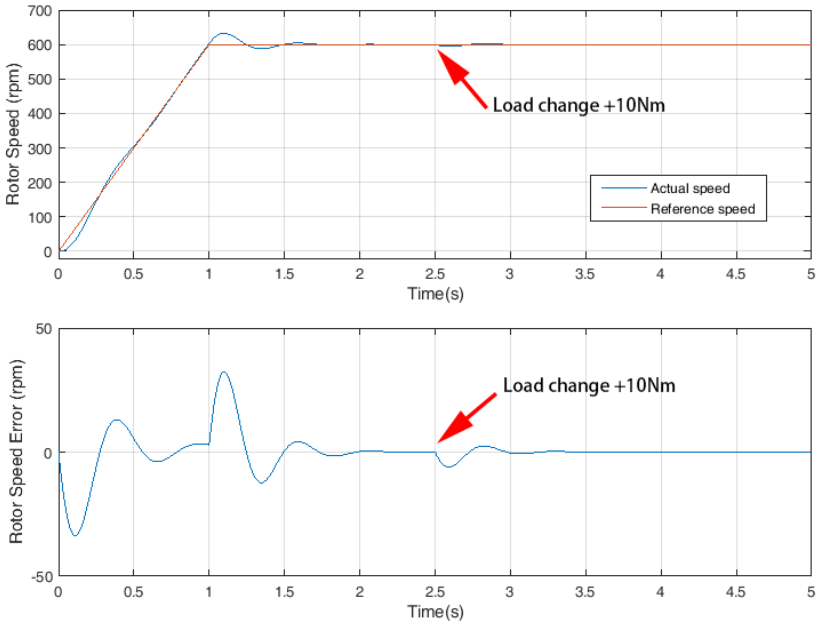

(a) PI Controller

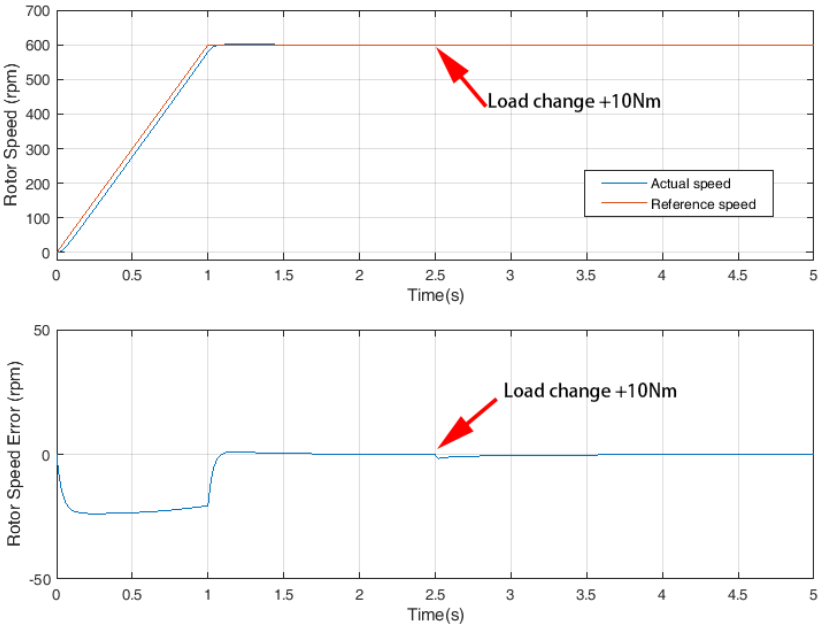

(b) ORC

Figure 3.3: ORC simulation results: speed tracking

more remarks about ORC and its industrial applications will be established. For each section, the introduction on both test rigs is given before the test results.

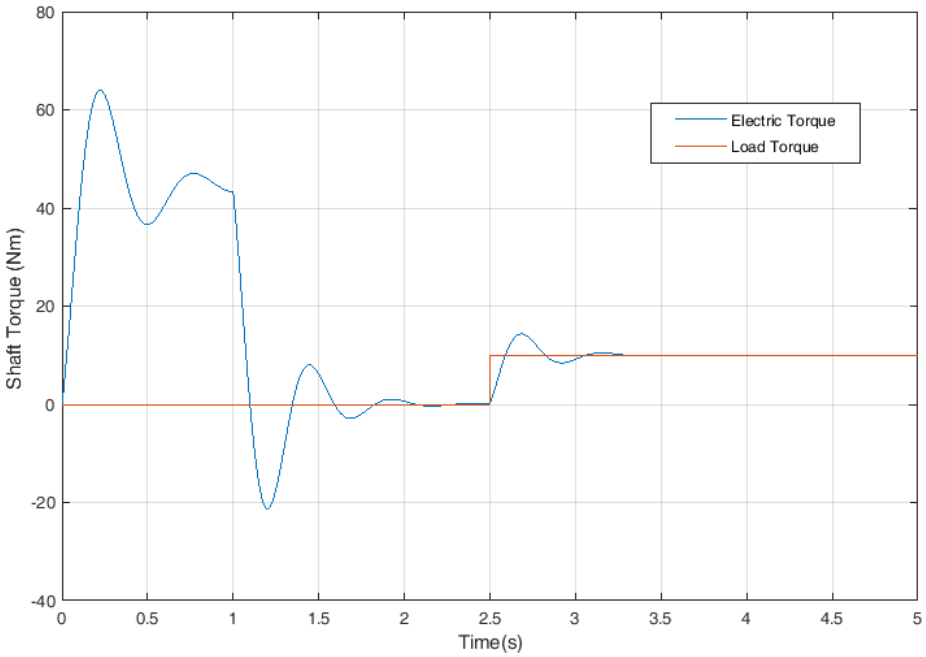

(a) With PI Controller

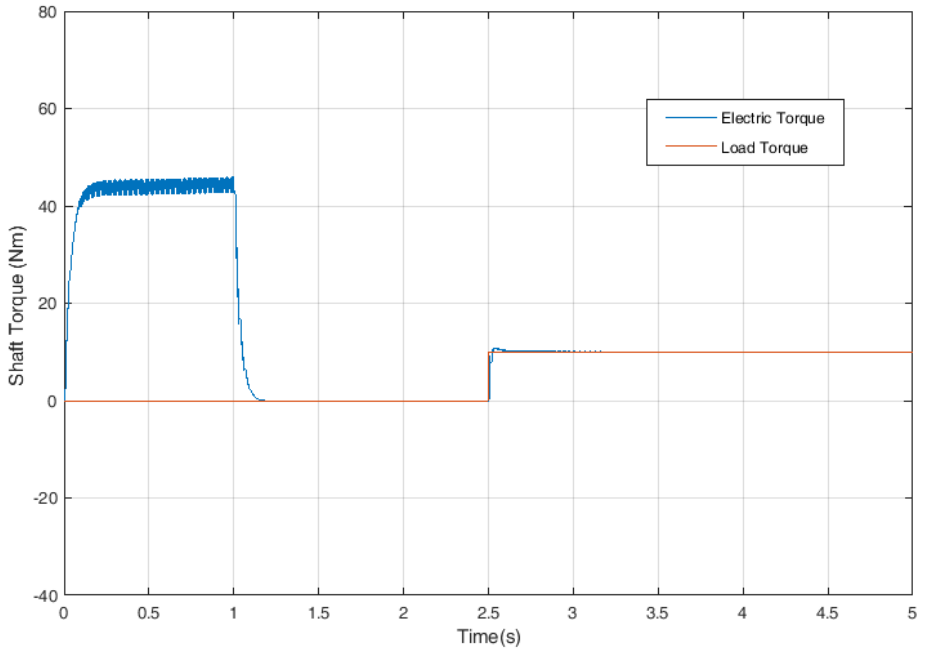

(b) With ORC

Figure 3.4: ORC simulation results: shaft torque

3.5 Hardware in the Loop (HIL) Test

HIL test is widespread in industrial applications. In this section, its background and hardware rig set up is shown. The performance of the ORC is further proved.

3.5.1 Introduction to HIL

The hardware in the loop (HIL) test rig is a practical tool to test motor controllers. HIL test is widely used in other fields like automotive and aircraft industries. In power electronic system related tests, it has only been applied for the past decade [117], OPAL-RT real-time simulators are considered more suitable for power electronic HIL tests. For the power system area, Yunwei et al. in [118] show a decent demonstration on applying real-time digital simulator (RTDS) to a multibus microgrid system simulation.

In an HIL test, the hardware system and a software system are combined in a closed loop. It is usually considered as a method between software simulation (or software in the loop) and hardware test. In contrast to them, The advantages and disadvantages of HIL are listed as follows.

- The HIL test can yield more information than the offline simulation. Many disturbances in the analog to digital conversion, the encoder signal transformation are hardly shown in offline simulations. With HIL test these conditions will be considered, and researcher can gain more confidence in the algorithm before it goes to hardware test.

- To test an algorithm on an HIL platform is safer, the system is capable of reset any required moment without obliging to concern about hardware damages.

- Some severe working conditions are very difficult or even impossible to test on real motors. For example, to test a controller performance against resistance variation, the traditional approach is to run the motor for a long time to heat it up, which risks damaging the motor. In addition, it is not suitable for multiple tests, and it is hard to define the parameter variation.

- HIL test runs in real time, i.e., the simulation clock follows the real clock. The system state will update regardless the DSP 's computation statues. For complicated control algorithms, HIL can test the DSP capacity for the

algorithm. Additionally, HIL can test the system behave when the controller signal is not complete.

For a system of very high power, run a HIL test before full hardware test is a valuable evaluation for the controller. In [119], A power hardware in the loop (PHIL) test is made for a five-megawatt scale motor drives. In PHIL test, the output signal from the simulator is amplified before it goes to the hardware system.

The synchronous between hardware and software system is very important in the HIL test. In [120], HIL test is introduced to power electronics systems. The real-time digital simulator is applied to simulate a voltage source converter. The synchronous issue is solved by applying a time average method.

HIL tests are also instrumental in grid size tests. A very large scale power grid is tough to build in a laboratory environment. Instead, it is much easier to make a model with HIL, which is flexible and its test conditions are very similar to real working conditions [121].

3.5.2 HIL with Opal-RT Real-time Simulator

An OP5600 Opal-RT real-time digital simulator is applied in this project. This real-time simulator is based on a PC/FPGA structure. The system setup is shown in Figure 3.5. The HIL testing platform contains a real-time simulator, a target PC, a TMS320F28335 DSP controller, and necessary interface circuits. The model running in a real-time simulator is coordinated with software called RT-Lab. Model is downloaded to Opal-RT with Ethernet cable. After the simulation is started, Opal-RT communicates directly with DSP, and PC only works as a monitor to the system.

Take the motor control test for an example, the motors and inverters simulation are based on the Simulink model. A model that is ready for compile looks like Figure 3.9. The model needs to be modified with certain blocks provided by RT-lab software. Normally, the add-on blocks are required by input/output task, which is distinctive in HIL test in contrast to the software in the loop (SIL). Occasionally, the original Simulink blocks need to be replaced with a simplified one in order to save the calculation time. For example, the block marked with "A" in a red circle in Figure 3.9 manage signals received or sent through one of the hardware communication blocks. On the other hand, "B" in the red circle is a simplified model of a 2-level inverter to enable the simulation running in real-time.

"C" is the "OpComm" module, which enables the user inputs to the system while the real-time simulation is on.

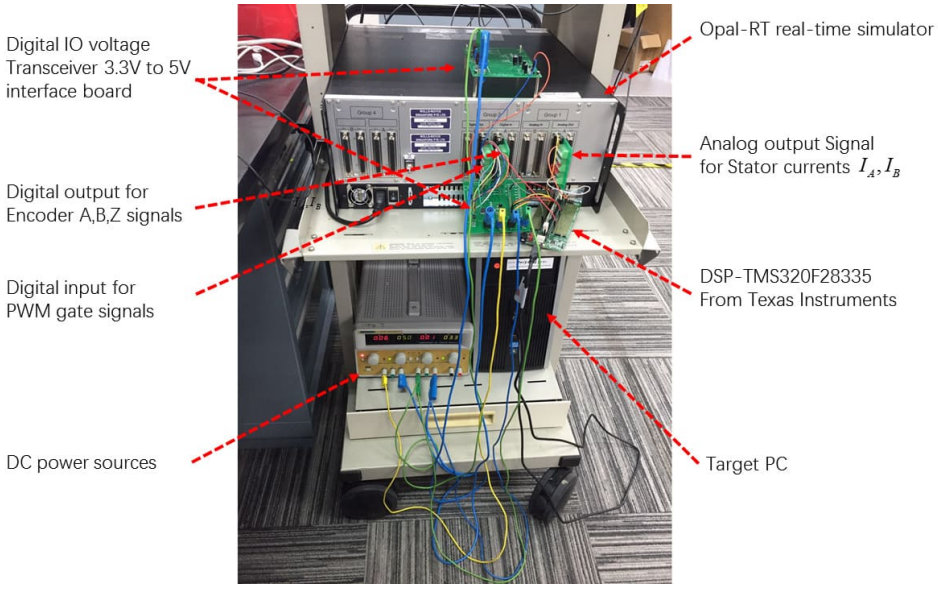

Figure 3.5: Opal-RT real-time simulator in laboratory

Because of the PC/FPGA structure of the OP 5600, the environment of the DSP controller in an HIL test is comparable to the real motor tests. The interface between Opal-RT and DSP controller is shown in Figure 3.6. Due to the different voltage levels between the DSP controller and the simulator, voltage shifters of 5V to 3.3V are equipped. The ADC block here refers to the built-in ADC on F28335 DSP.

The HIL test results of induction motor running in stepped speed reference are shown in Figure 3.7 and Figure 3.8. They are plotted on the monitor PC during simulation. In both figures, the upper subfigure is the rotor speed of the motor in *rpm*, and the lower subfigure shows the three-phase current in Ampere.

In Figure 3.7, the motor speed response of a step reference signal is shown. Standard PI controller is applied in this test. Overshoot is observed whenever there is a sudden change to the speed reference.

In Figure 3.8 the zoom in view of constant speed at 600 rpm is shown. There is a small flutter in the speed reading, and steady-state error is within 1 *rpm*. In addition, three-phase voltage is not perfectly balanced. This error may be induced by the offset error in analog to digital converter (ADC) of the stator current sensor. This kind of error could not be observed in pure software simulation, but they

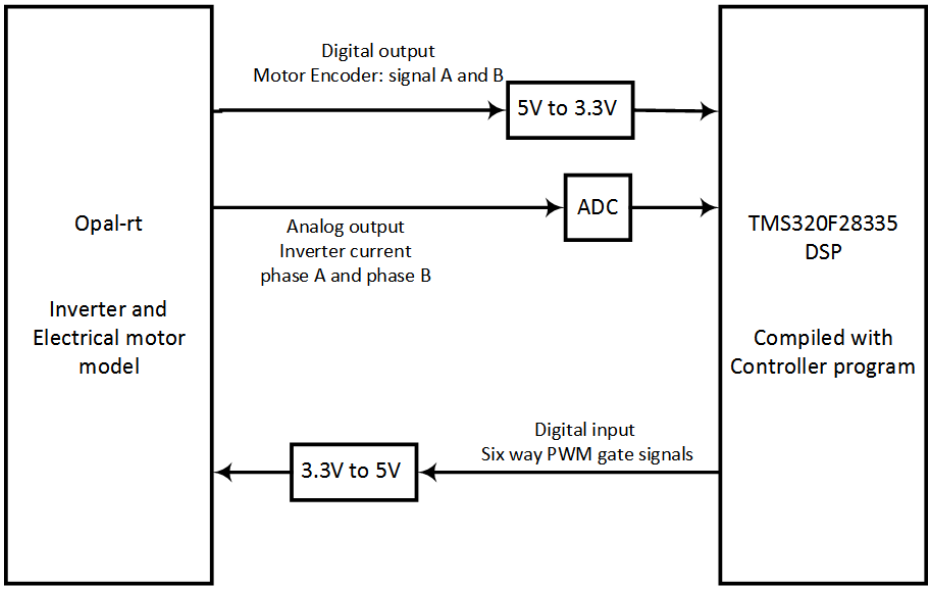

Figure 3.6: Opal-RT and DSP interface configuration

should not be ignored in a hardware test. An advantage of HIL is to value the influences of this kind of error before real hardware tests.

3.5.3 HIL Test of the ORC

With the HIL test rig introduced in Section 3.5.2, the performance of the ORC is tested in this section. ORC is coded with C and compiled into TI F28335 DSP, the parameters of 15 kW Teco motor (Table 3.2) are applied on the hardware plant model. The model compiled in Opal-RT simulator can be found in Figure 3.9.

For the DSP programming, the switching frequency is set to 10 kHz. The Simulink model runs in continuous time while in DSP it runs in discrete time. Due to the difference in the environment, the controller parameters have been redesigned. Due to the communication lag of the DSP to the real-time simulator, it is necessary to design system control parameters with a more robust method.

A stepped speed test and a constant speed test are implemented to show the performance of the speed controller on the HIL. During the HIL test, the PC that connected to the OPAL-rt with an ethernet cable is working as a " virtual oscilloscope", the real-time results are shown in Figure 3.7 and Figure 3.8. In both figures the results are only applied as the real-time signal that monitoring the

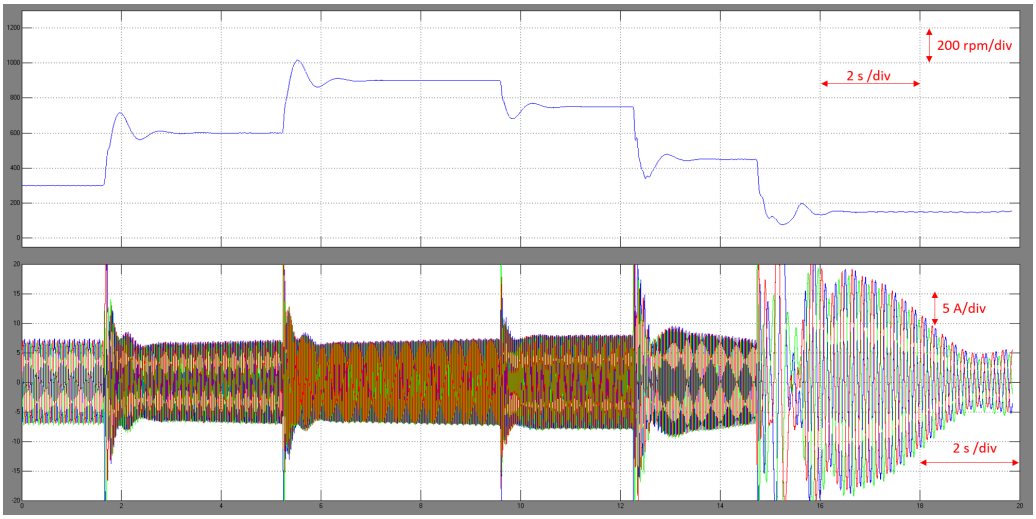

Figure 3.7: Induction motor HIL test: stepped speed

system, their resolutions are not very high as a compromise to achieve system fast response. More accurate results are read with a real oscilloscope which connected to the analog-digital conversion (ADC) module on the Opal-RT.

The experimental results of PI controller are given in Figure 3.10a and Figure 3.10b. The step reference is given as 300 rpm, 600 rpm, 900 rpm, 450 rpm, 150 rpm respectively. Reference speed switches every 1.5 Second. The x-axis of the oscilloscope shows the time in 2s/div, and the y-axis shows the analog signal of rotor speed with a $\frac{1}{400}$ gain. The unit on the oscilloscope is 500 mV/div.

The corresponding stator current is shown in Figure 3.10b. This signal is used as the feedback in the current loop from the Opal-RT real-time simulator to the DSP. As a result, it will be read by the analog-digital conversion (ADC) module. Note that only a voltage between 0 V to 3.3 V is readable to the ADC module, higher voltage will damage the circuit. The signal firstly went through a gain of $\frac{1}{70}$ to keep between -1.5 V to 1.5 V, then added 1.5 V offset to achieve the desired voltage. It is noted that this gain needs to be changed according to the current range for different motors.

The rotor speed and stator current response of reset controller are shown in Figure 3.11a and Figure 3.11b. Except for the controller, these two tests share the same environment, including the switching frequency, communication gains, etc. For the reset controller, the reset interval is chosen as five times of the base time interval.

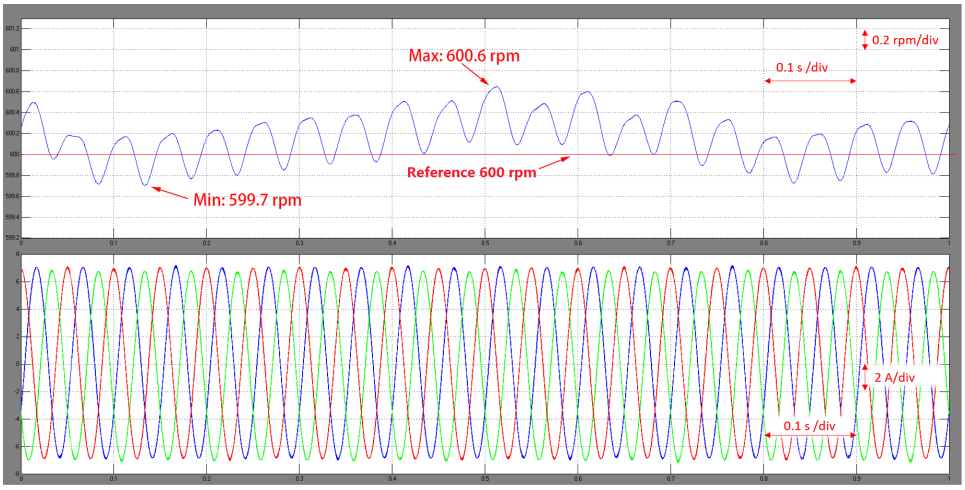

Figure 3.8: Induction motor HIL test: constant speed

The speed response from the PI controller in Figure 3.10a shows that when a step reference is applied to the speed loop, there is an overshoot about 20 % whenever the speed increases or decreases. On the other hand, in Figure 3.11a, the speed response of the same step reference, the overshoot is eliminated while the overall setting time is decreased by 50%. Moreover, from the current results, the current ripple in Figure 3.11b is reduced, the maximal current for reset controller is also smaller than the PI controller.

The HIL test results proved that with the help of the ORC, the dynamic response for the base PI controller is improved. It is possible to apply the ORC to an existing industrial PI controller to improve its dynamic response. This characteristic is further proved in the hardware test in Section 3.6, where ORC is applied to two linear systems with different damping ratios.

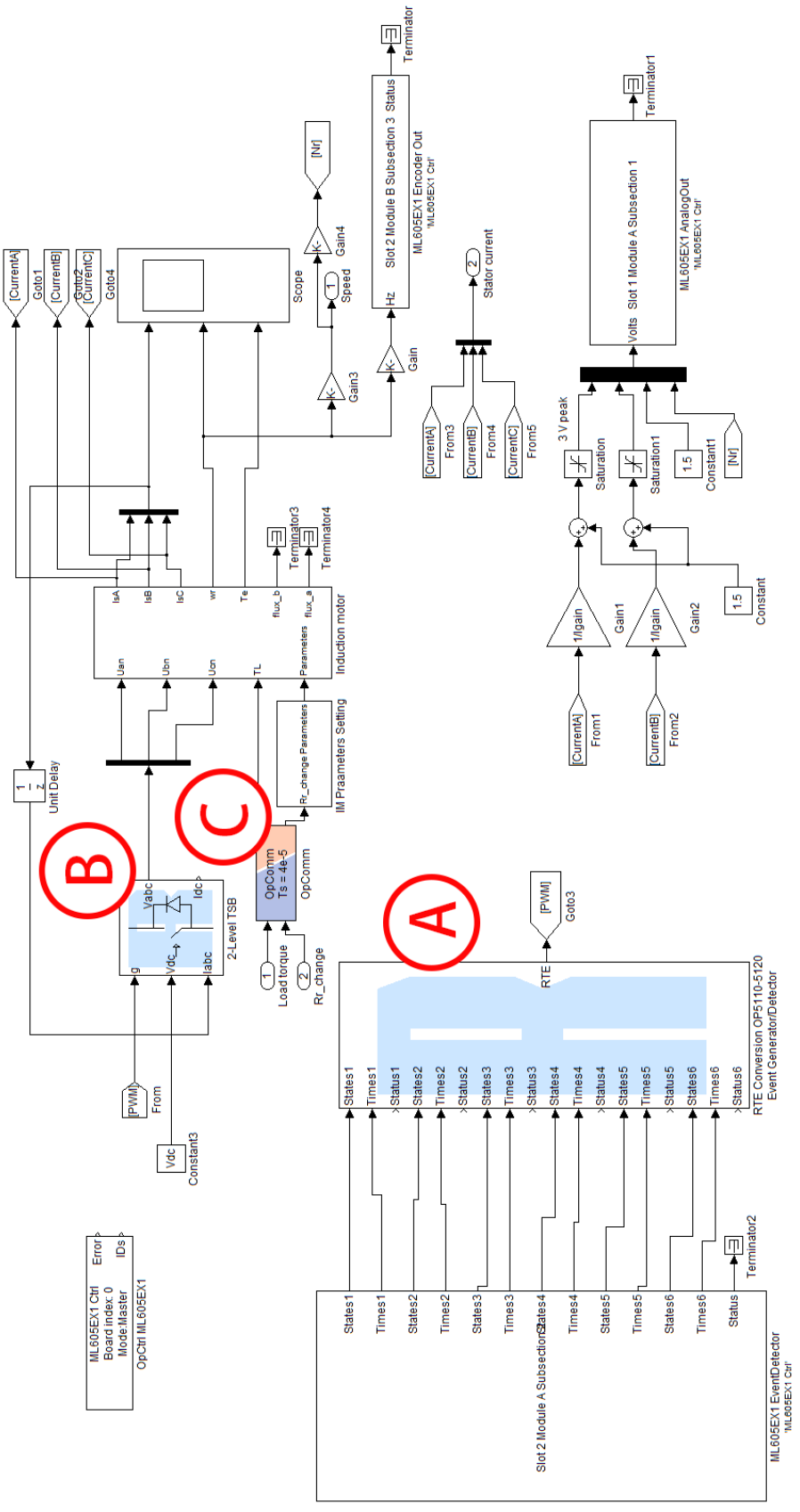

Figure 3.9: IM modeling with RT-LAB
(A: Event generator, signal exchange with hardware communication blocks; B: simplified model of 2-level inverter; C: “OpComm” module for on-line tuning.)

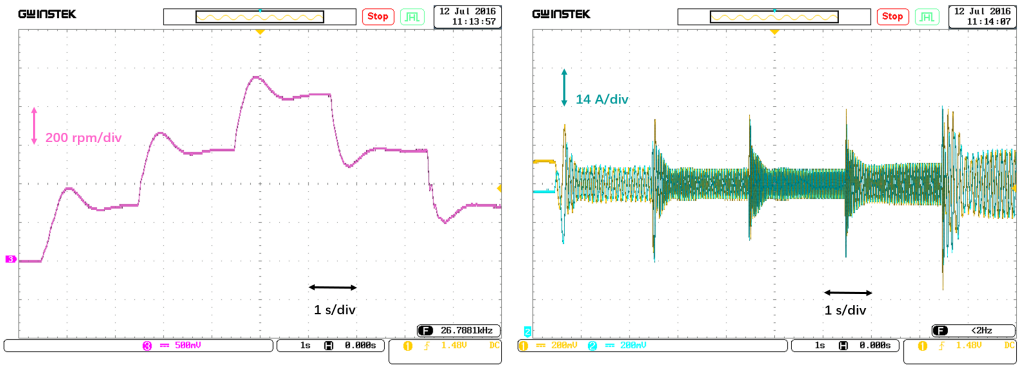

(a) Speed response of PI controller

(b) Two-phase stator current of PI controller

Figure 3.10: HIL test results with base PI controller

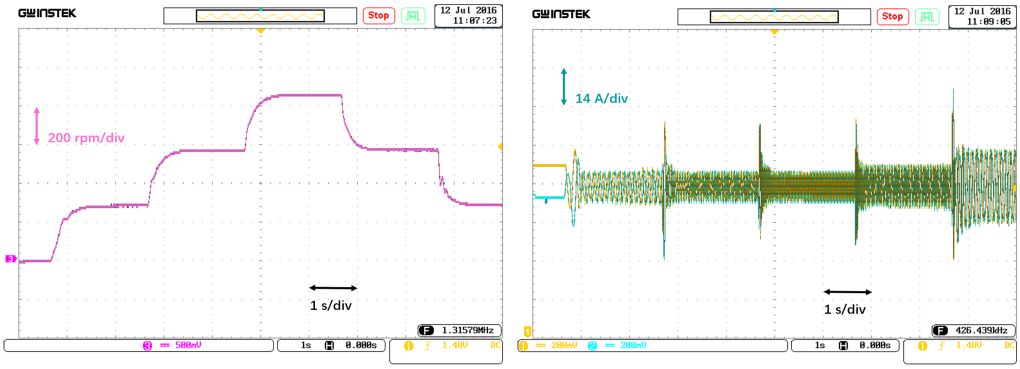

(a) Speed response of ORC

(b) Two-phase stator current of ORC

Figure 3.11: HIL test results with ORC

3.6 Hardware Test

Following HIL test, full hardware test is made with a 15 kW test rig. The test rig is introduced before the test results are shown.

3.6.1 Hardware Test Rig

The hardware test platform setup for induction motor controller are shown in Figure 3.12 and Figure 3.13. A SEMIKORN three phase IGBT inverter is used. This inverter is equipped with a water cooling system. A 15 kW motor is implemented in the test rig. As shown in Figure 3.12, the left end shaft of the motor is connected to an encoder, and the right end is connected to a load motor with a torque sensor. The torque sensor signal is sent to the computer who controls the load motor.

A 20 kW induction motor is installed as the load machine. Its inverter and controller are integrated and shown in Figure 3.13, along with an interface PC. The load motor uses a built-in PI controller in the PC. There are several options for operation mode. The controller can work under both speed or torque mode with the help of speed and torque sensors.

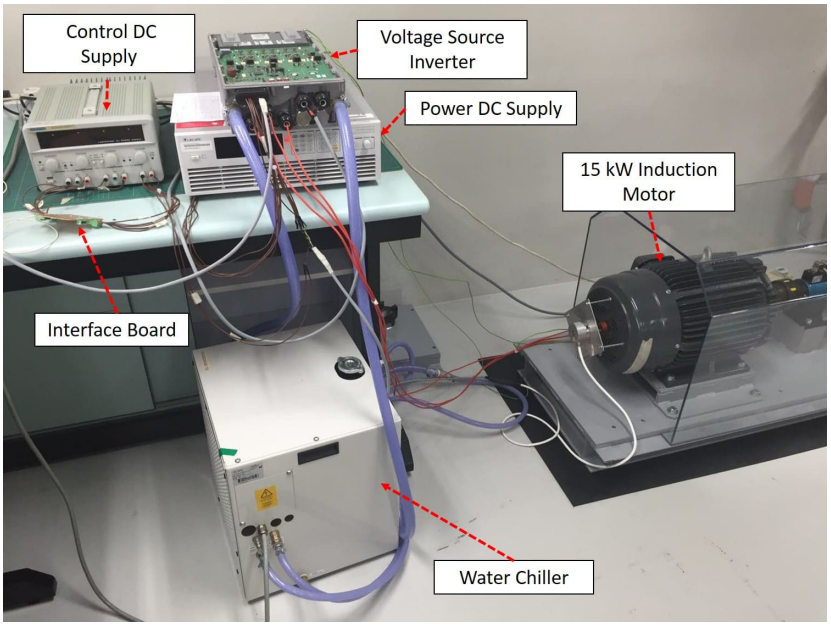

Figure 3.12: Semikron Invertor and Teco induction motor

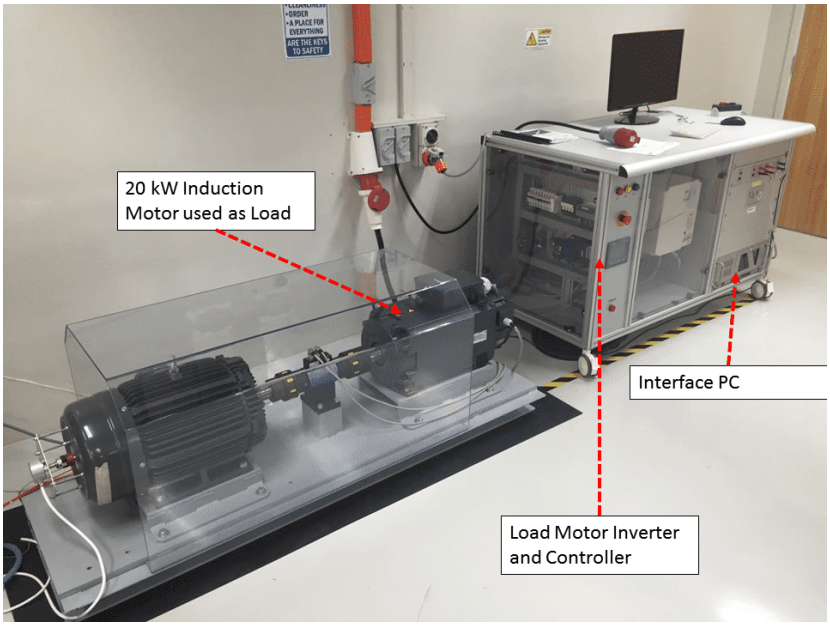

Figure 3.13: The load machine and its controller

3.6.2 Three-phase IGBT Inverter

The Semikorn SKAI2-HV three-phase IGBT inverter (Figure 3.14) is applied for the test rig. The input DC cable and output three-phase cable is observed in the picture. For this compact inverter, it is ideal for mobile applications such as electric vehicles, agriculture machinery. Additionally, water cooling is essential for the working condition of high power.

A programmable TMS320F28335 DSP from Texas Instruments is built-in as the microcontroller. The program is downloaded through a 12 pin JTAG connector. An external emulator is required.

The X1 connector shown in Figure 3.14 has 35 pins. This multifunction connector serves for both input and output signals. The control DC power source is applied to the 24 V auxiliary power supply, and the hazardous voltage interlock loop (HVIL), which is a current loop that works as a monitoring circuit for system connections. Other pins provide functions like the resolver or encoder signal transmission, CAN communication, RS232 communication, output ports for internal sensors, etc.

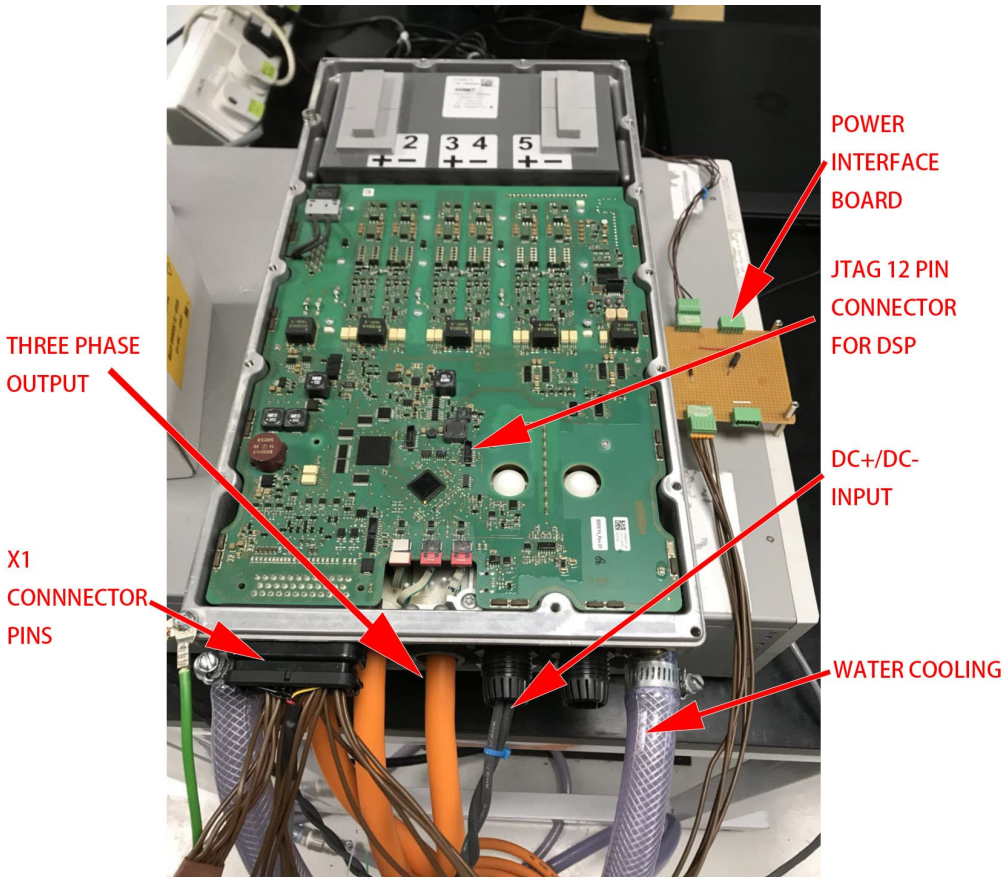

Figure 3.14: The Semikorn inverter setup

3.6.3 Rotor Position and Speed Sensors

Both encoder and resolver are designed to measure the rotor speed of an electrical machine. They are essential for closed-loop control in speed.

Encoder

In this experiment rig, an optical incremental encoder is implemented to measure the rotor position and speed (Figure 3.15a). For most type of encoder, there three output signals, A, B, and Z. All of them are differential signals. Thus there are six cables in total.

The working principle of an optical encoder is illustrated in Figure 3.15b. There is a plate with multiple slots that rotating with the motor rotor. On one side of the plate, there is an LED while there are sensors on the other.

A and B are the quadrature pulses generated from the slots that around the plate, signal B has a phase lag to signal A. In this approach the rotating direction can be found by the combined signal. The pulse signal is counted by DSP, refering to the total number of pulses, the rotor speed is calculated.

Z pulse (also known as the index signal "I pulse") is introduced to obtain the rotor position. Z pulse can be considered as a special slot that occurs once a mechanical rotation. Once the encoder is installed on the electrical machine, its Z pulse position is fixed, which implies it is possible to convert the relative position to the absolute position. Absolute position is not essential to IM control because the rotor flux direction is not fixed. However, when it comes to permanent magnet machines, the rotor flux direction is obtained once rotor physical position is found, the value of the latter should not be underestimated.

Resolver

Another kind of rotor speed/position sensor is called resolver. It is also used for another test rig shown in Figure 3.16a. Resolver works like a transformer. The primary and secondary windings are placed on the stationary part of the resolver. The rotor of the resolver is a metal in a particular shape, like Figure 3.16b. The metal works as the insulating medium for the transformer, and particular shape leads to a distinctive transformer ratio in various rotor positions. The rotor of the resolver is connected to the motor shaft. An excitation voltage is given to resolver by DSP controller. The exciting voltage and output voltage waveform are shown in Figure 3.17. Exciting voltage (green) is the sinusoidal input to the resolver.

(a) Installed Encoder

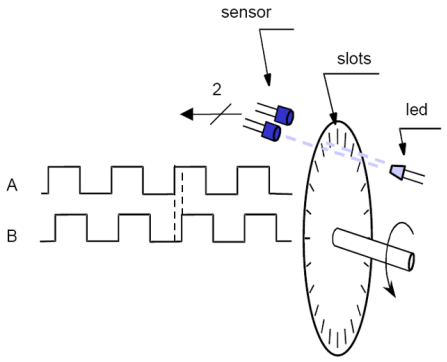

(b) The working principle of encoders

Figure 3.15: Encoder

Both yellow and red are the output voltage. As the output of a transformer, their frequency is not deciding, their magnitude is. With the rotor position shift (x-axis of Figure 3.17), the envelope for the output voltage magnitude is a sinusoidal waveform. The rotor position and speed are calculated with the relationship between the yellow and red curve.

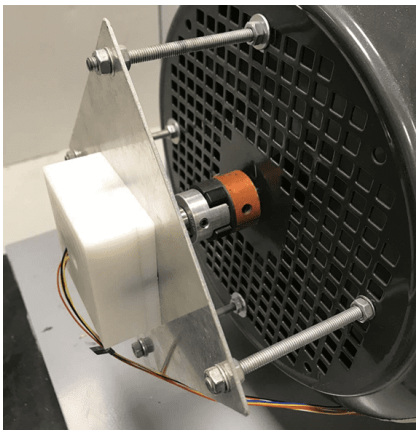

(a) Installed resolver

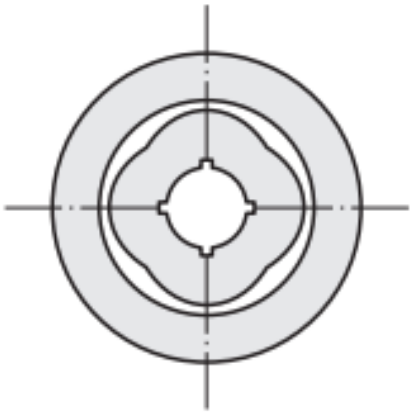

(b) 4X rotor shape [122]

Figure 3.16: Resolver

A Compare Between Encoder and Resolver

Chose the right speed/position sensor is really important in various working conditions. The difference lies in the following perspectives.

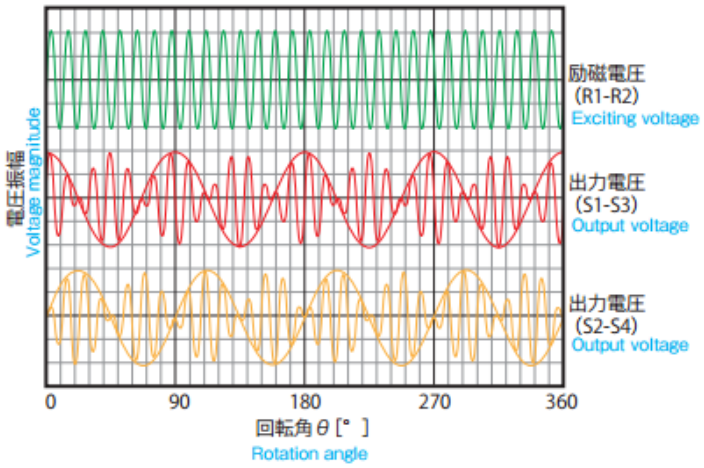

Figure 3.17: Resolver: stator side voltage and rotor side voltage [122]

Firstly, the accuracy for a encoder is higher than a resolver. The encoder installed in this test rig (Figure 3.15a) has a resolution of 5000. Which means there are totally 20000 (counting signal A and B, for both rising edge and falling edge) pulses in single mechanical rotation. Theoretically, it can detect as small as 0.018° change in the mechanical angle. However, as resolver output is in analog , its results are less accurate. Furthermore, resolvers' rotor have various shapes. For example, the resolver in Figure 3.16b has 4 multiples, that means the output is an absolute angle within 90°, but in which quadrant it lies is uncertain.

Second, for the encoder, its output is a comparative value, the absolute angle is unknown until the first Z pulse is caught. For resolver, an absolute angle is achieved once the device is powered on, it is possible even if the rotor is stood still.

In the end, the encoder is more fragile in contrast to the resolver. Small physical damage, for example, falling to the ground from more than one meter, is possible to disable an encoder. On the other hand, resolver has vibration resistance of 20G and shock resistance of 100G [123]. It can work under high temperature and humidity. Given that many motors are designed to operate under extreme conditions, resolver has a significant advantage in this point.

3.6.4 Selection of Base Linear System Parameters

The PI controller designed for both current loop and speed loop is designed by pole placement method. The closed-loop transfer function of the current loop and

speed loop is like Equation (3.28) and Equation (3.29).

$$G(s) = \frac{i_q}{i_q^*} = \frac{i_d}{i_d^*} = \frac{K_p s + K_i}{L_s s^2 + (R_s + K_p) s + K_i} \tag{3.28}$$

$$G(s) = \frac{\omega_r}{\omega_r^*} = \frac{K_p s + K_i}{J s^2 + (B + K_p) s + K_i} \tag{3.29}$$

The closed loop characteristic equation of both control system is given as

$$D(s) = s^2 + 2\xi\omega_n s + \omega_n^2 \tag{3.30}$$

where ξ is the designed damping ratio and ω_n is the natural frequency. In this, chapter the focus is on the speed loop, the current loop PI parameter is kept constant. Motor mechanical and electrical parameters used are shown in Table 3.2. For speed loop ORC, the PI parameters are used as the base linear system, two sets of parameters with different damping ratios are selected to show that the ORC can provide an improvement to both. Two sets of PI parameters are shown in Table 3.3. Their corresponding speed loop response are observed in Section 3.6.5.

Table 3.3: PI controller parameter design

	$\omega_n(rad/s)$	ξ	K_p	K_i
Speed loop #1	70	0.200	0.622	109.180
Speed loop #2	70	0.707	2.204	109.180

3.6.5 Hardware Test Results

The performance of the ORC is determined from the combination of the base linear system and the reset law design. In this section, the ORC is tested under two sets of PI controllers. The speed tracking diagram is given, the speed error is compared, and the hardware test results are shown in Fig. 3.18 and Fig. 3.19. The speed loop reference is given from zero to +600 rpm, followed by a drop to -600 rpm and a return to zero. Here, a 600 rpm/s ramp is introduced to both the acceleration and deceleration processes to protect the hardware.

In Figure 3.18, the speed loop PI parameter #1 in Table 3.3 is employed, the

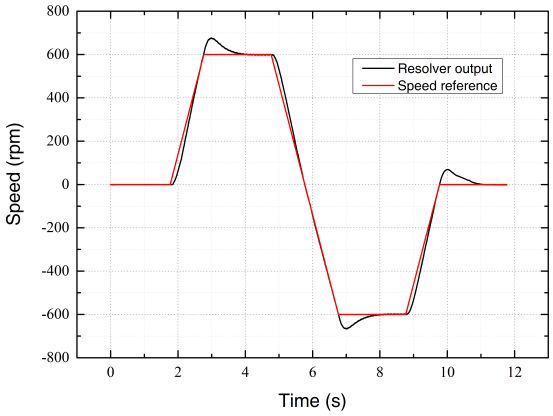

(a) PI controller

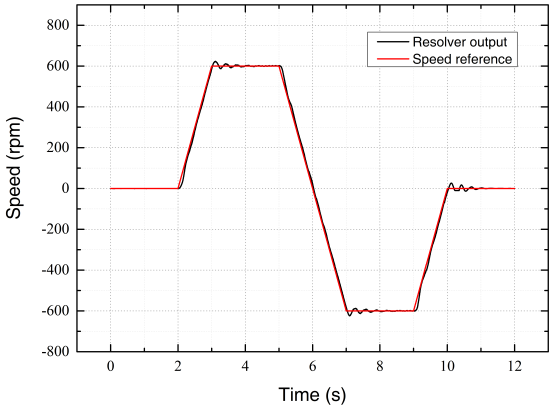

(b) Optimal reset controller

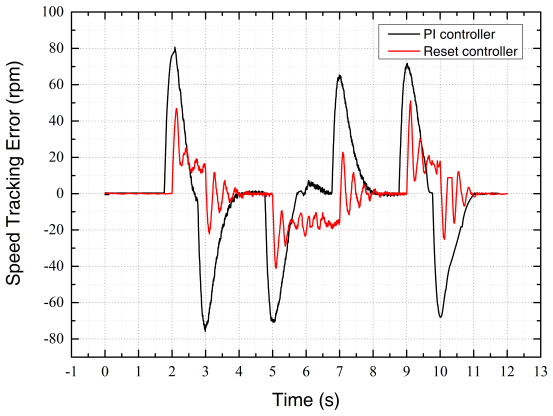

(c) Tracking error compare

Figure 3.18: Speed tracking results for speed loop #1

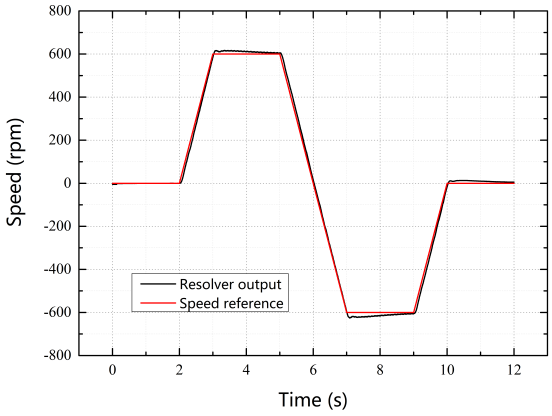

(a) PI controller

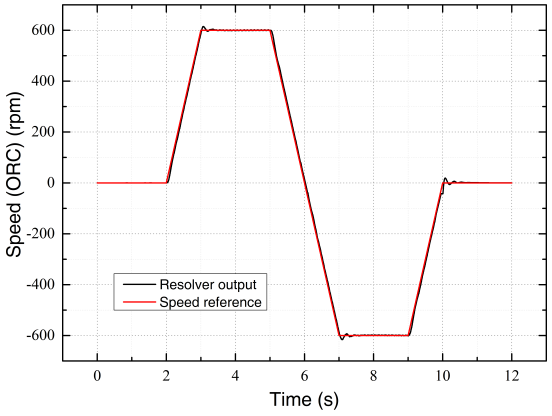

(b) Optimal reset controller

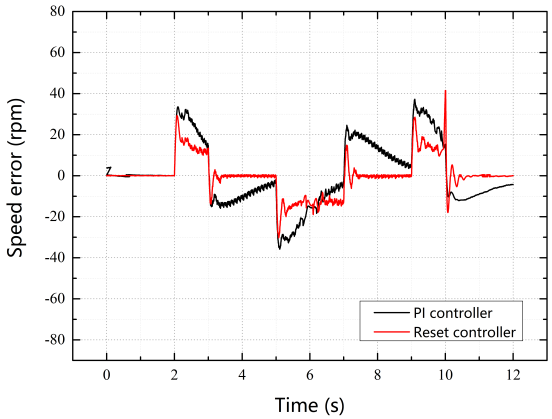

(c) Tracking error compare

Figure 3.19: Speed tracking results for speed loop #2

optimal reset law is calculated as

$$K_1 = -10.1622$$

Similarly, Figure 3.19 shows the optimal reset results in speed loop PI parameter #2, with the corresponding optimal reset gain calculated as

$$K_2 = -4.9695$$

The hardware results show that the ORC can be introduced as an add-on to a stable base PI controller. For different damping ratios, the ORC can provide an improvement to the system dynamic response.

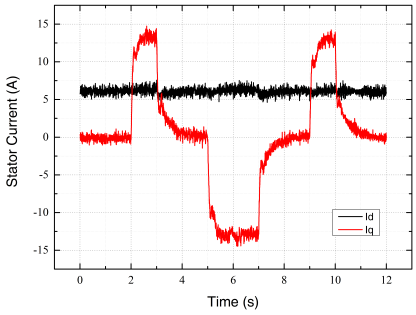

(a) Stator current under PI controller: speed loop #1

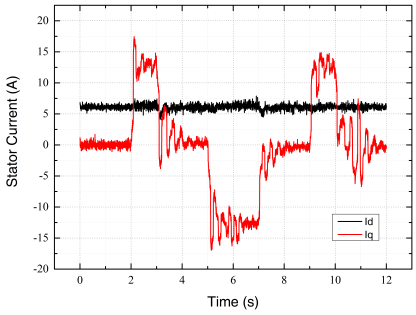

(b) Stator current under ORC: speed loop #1

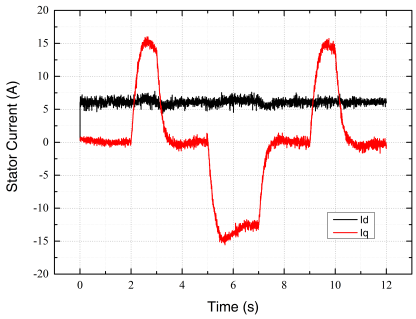

(c) Stator current under PI controller: speed loop #2

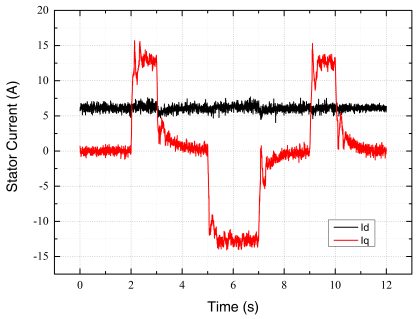

(d) Stator current under ORC: speed loop #2

Figure 3.20: Stator current in dq reference frame

The dq-axis current is recorded in d-q reference frame from DSP. Results are shown in Figure. 3.20. The current signals are logged for two PI controller sets

(speed loop # 1 and # 2 in Table 3.3) and corresponding ORCs. i_q has a linear relationship with the output of the speed loop controller. In a comparison of the q-axis currents (red-curves) in Figure. 3.20a to Figure. 3.20b, and Figure. 3.20c to Figure. 3.20d, the sudden changes in the q-axis currents introduced by the optimal reset law are observed. This sudden changes reveal the non-linearity of the ORC. Which is the characteristic that enabled the ORC to increase dynamic response while eliminating the overshoot.

The d-axis current remains constant since the constant rotor flux reference of $\phi = 0.5\ Wb$ is applied in all the tests.

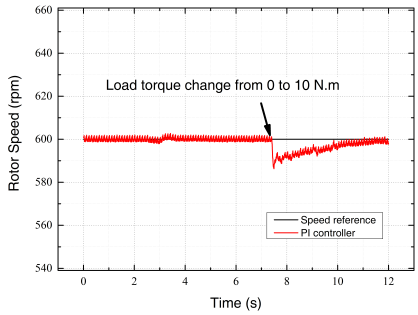

(a) Adding load on PI controller

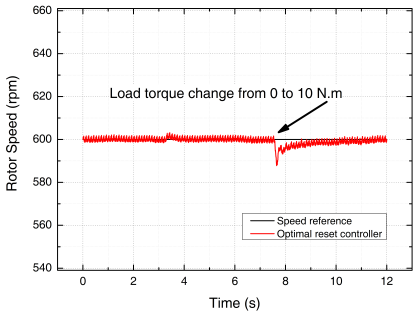

(b) Adding load on ORC

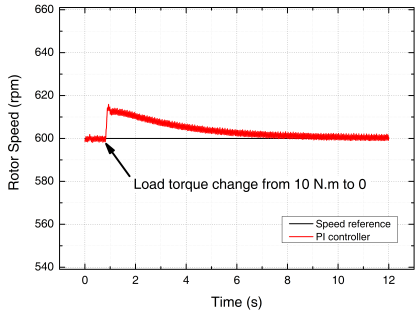

(c) Removing load on PI controller

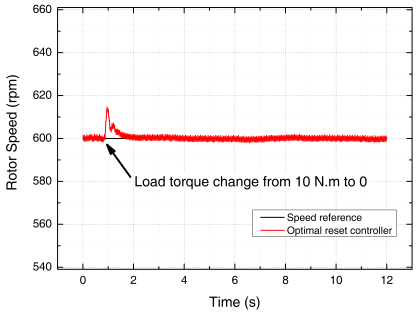

(d) Removing load on ORC

Figure 3.21: Sudden load change test for PI and ORC

To further evaluate the dynamic performance of the ORC, a sudden load change test is introduced. A 10 Nm load is added and then removed, and the test results are shown in Fig. 3.21. The PI parameter used in this test is the speed loop PI parameter #2 in Table 3.3. It is shown in Fig. 3.21a and Fig. 3.21b that for both controllers, the speed drops when a sudden load change is applied, and

the recovery time for the ORC is shorter than that for the PI controller. The same occurs when the load is removed in Fig. 3.21c and Fig. 3.21d.

3.6.6 Robustness Against System Parameter Variations

In this section, the influence of parameter variation to the performance of ORC is discussed. For the ORC implemented on the machine speed control loop, the system model is as

$$\begin{cases} \dot{x} = -\frac{B}{J}x + \frac{1}{J}u \\ y = x \end{cases} \tag{3.31}$$

where the moment of inertia J and friction factor B are the system parameters.

A. Moment of inertia J

The machine moment of inertia $J = 0.14\ kg.m^2$ is identified with an off-line method in the hardware test rig shown in Figure. 3.12 and Figure. 3.13. Additionally, the inertias of the load machine and the shaft are not considered in the optimal law design. In industrial applications, it is equally challenging to track the accurate inertia of the shaft and the load.

B. Friction factor B

In most industrial applications, the friction factor B is neglected due to two reasons. Firstly, most machines are well lubricated, and friction is minimal compared to inertia. It has a minimal influence on the system. Secondly, the actual value of B is not simple to measure. The torque induced by B is ordinarily proportional to rotor speed. In higher speed ranges, windage resistance increases and make the friction-speed curve distorted.

ORC is a model-based method. It is sensitive to the parameter error. However, the influence of error is compensated with the help of load torque observer. An electrical machine can store or release energy when its speed changes. The amount of this energy depends on the machine inertia J. Similarly, when there is a J_{err} between machine J and controller J, one can consider J_{err} equivalent to an additional load to the system in dynamic. In that case, when the additional load is observed and compensated by the load observer, it is equivalent to the J_{err} is compensated.

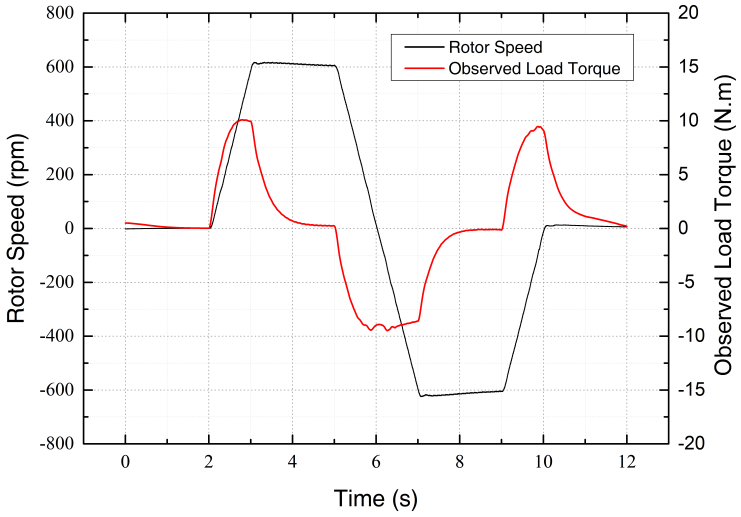

Figure 3.22: Load torque observer output

This phenomenon is observed in a hardware result in Figure. 3.22, where the load torque observer output under a no-load acceleration and deceleration test are shown. The load torque observer requires the knowledge of system inertia, and its output should remain zero under no load condition. However, the red curve in Figure. 3.22 is obviously not zero. This result is explainable through J_{err}. In this particular hardware test, it is caused by the inertia of the loading machine since it is not calculated in optimal reset law design. This load torque observer result is applied to z_r in Equation (3.26) to compensate the dynamic tracking error caused by J_{err}.

3.7 Summary

In this chapter, a novel algorithm is provided to improve the dynamic performance for electric machine speed loop controller. The background review is made on the methods that have been introduced to solve the dynamic response issue. Then the ORC is presented. As a non-linear method, ORC is designed to overcome the limitation from the conventional linear controller, to eliminate overshoot while maintaining high response speed. The previous implementations of ORC have been reviewed.

Next, the design procedure for ORC is illustrated in detail. There are three sets of parameters that essential to the reset law, which are base system PI values, optimal law gain K, and steady-state z_r. Even though there is no quantitative approach to decide the cost function weight Q and R, their relation and the designing guideline are discussed.

Next, ORC is tested on an IM. In the beginning, simulation results are carried out. Then an HIL test is carried out, where the controller is replaced with DSP, and the hardware rig is running on an OPAL-RT real-time simulator. In the end, OPAL-RT is replaced with a three-phase inverter and a 15 kW IM. HIL provides a method to verify the controller without damaging the hardware, protecting the researchers from potential risk and gain their confidence. These three tests present a whole process of carrying simulation to hardware test. The simulation and test results align with each other, showing that ORC significantly decreases the speed tracking error in speed increasing and decreasing processes. ORC is also tested with sudden load change tests. It shows that the speed recovery time for both adding and removing load is shorter than pure PI controller.

For ORC, the real-time rotor speed is applied in the feedback. Thus speed sensor (i.e., resolver or encoder) is still required. In many particular industrial applications, a speed sensor is not available. In the next chapter, the issue of sensorless control will be discussed.

Chapter 4

Sensorless Control for Permanent Magnet Synchronous Machine

In this chapter, the sensorless control for PMSM is discussed. A smooth transition method is proposed to improve the transient performance between the open loop and the FOC. The smooth transition method is designed based on an analysis of the relationship between the q-axis current and the error angle. In addition, the open loop starting and sensorless closed-loop FOC based on the back-EMF approach is illustrated respectively to show the transient issue.

In Section 4.1, the importance of the PMSM sensorless control is highlighted. A thorough review is made on the present-day approaches. The estimation of the back-EMF is the foundation of the majority the speed estimation algorithms. However, the sensorless control that based on the back-EMF estimation has limited performance in low-speed operation when the back-EMF is very small. To overcome this drawback, an open loop approach is proposed to start the machine. After the PMSM has accelerated to a reasonable speed ("controller switch point"), the controller would switch the controller to back-EMF based sensorless FOC.

A diagram of this process is shown in Figure 4.1, which also illustrated the scope of this chapter with the section numbers labelled on it. The arrow in Figure 4.1 is the physical sequency of the PMSM starting. Section 4.2 and Section 4.3 are the background knowledge. The major contributions of this chapter are in Section 4.4 where the smooth transition method is proposed and the analysis to the openloop start process is made.

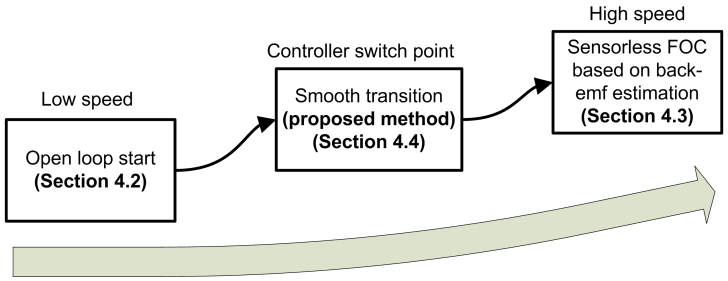

Figure 4.1: PMSM sensorless starting scheme

The smooth transition method is based on the analysis of the current misalignment between open loop and sensorless FOC. Its proposed is to reduce the q-axis current in a closed-loop way with the angle error as the feedback. Simulation verification and experiment results are shown in Section 4.5 and Section 4.6 respectively. It is proved that the proposed smooth transition method can improve the transient current, torque performance. Also the noise mechanical reduction is observed in the hardware tests.

4.1 Background of PMSM Sensorless Control

Permanent magnet synchronous machines (PMSMs) have been applied to many successful applications in recent years. The flux linkage of a PMSM is built by the permanent magnet inside the rotor. As a result, the power density of a PMSM is outstanding and its overall efficiency is excellent. In addition, there is no slip speed involved, their control algorithms are more straightforward. PMSMs have better performance in delicate position control applications

In marine applications, PMSMs are widely used due to their efficiency and high power density. However, in some specified working conditions, the machine must be controlled sensorlessly. The tunnel thruster is a typical application of PMSM. It is designed to place inside the tunnel of a ship bow or stern (see Figure 4.2). The purpose of this design is to provide a propulsion when the ship is docking or generate a thrust to maintain the vessel's position or adjust its heading (dynamic positioning) [124].

For the design of a tunnel thruster, the size and the efficiency are critical due to its limited space. For the latest design of tunnel thrusters of Rolls-Royce (shown in Figure 4.3), PMSM is introduced to gain higher efficiency and more compact installation [125]. This thruster is capable of generating equal thrust in

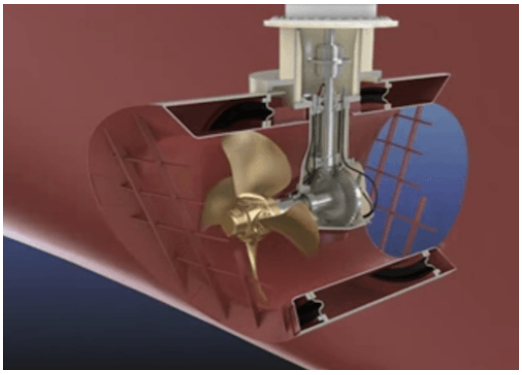

Figure 4.2: Installation of tunnel thruster [125]

both directions. Its power rating is 1000 kW to 1600 kW.

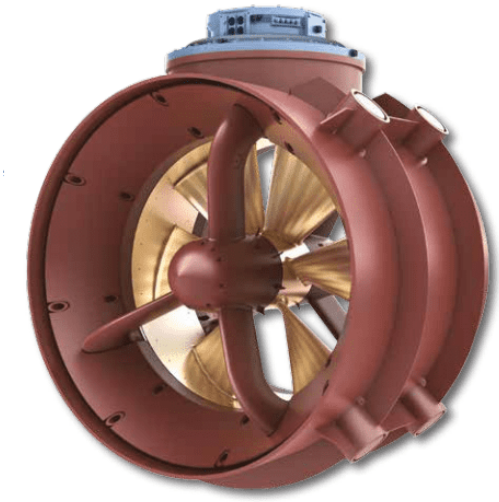

Figure 4.3: Rolls Royce TT PM Tunnel thruster [125]

In this tunnel thruster, the variable frequency drive is housed in the thruster, which frees the space on board. On the other hand, this design makes it impossible to fit a speed sensor on the machine. As a result, sensorless control is the only choice.

Generally, the rotor position estimation methods can be categorized into two classes, namely the model-based method and the non-model based method [126]. The model-based method estimates the machine back EMF with the help of the machine parameters. The back EMF direction can be used to estimate the rotor position since it is generated by the PM whose position is aligned to the physical

position of the rotor. The back-EMF based methods can be categorized as open loop [127] and the closed loop observers [128]. As the estimated back-EMF normally containing noise, the open loop method is not promising. literature review shows that the closed loop method is prefered by many papers. In [129–132], sliding mode observers are applied since they are easy to implemented and they are robust against the parameter variations. In [133], the MRAS control scheme is applied, where the real machine is considered as the reference, the output signal from an adjustable model and the reference are compared, and the estimation speed is calculated. The SMO is also a very commonly used method. In [134], a super-twisting algorithm based second order sliding-mode observer (STA-SMO) is applied. The super-twisting algorithm has a solid immunity against the chattering issue which is commonly faced in a first-order SMO. In [135,136], extended kalman filter (EKF) is applied to the sensorless observer for a valve control.

With the speed sensor installed, the risk of sensor failure should not be neglected. An EKF based sensor fault detection and isolation method is proposed in [137]. To detect the speed sensor fault, one can compare the speed sensor output with the speed observer output [138,139].

On the other hand, in an anisotropy-based (non-model based) method, high-frequency (HF) signal is injected to the machine to provide more rotor position information [140–142]. All HF injection methods take advantage of the saliency of the PMSM. That means the HF injection method is able to detect motor position even the motor is standing still. Both pulse signal and sinusoidal signal are applicable for signal injection [141]. According to [143], the pulse injection method has better accuracy and it is more robust against the dead time effect [144]. In [145], the advantages of sinusoidal and pulse signal are discussed respectively under two kinds of motor configurations. The saturation and magnitude of high-frequency injection signal are discussed. The influence of the analog to digital convertion (ADC) in the signal injection is discussed in [146], the safety operation area is explored. The frequency of the injection is usually set to ten times of the inverter fundamental frequency. In that case, it will resulting to a pulsating torque, and the machine remains to stand still due to the inertia and friction. The PMSM rotor may start to rotate if the injection frequency is not high enough.

The downside for HF injection method is that the additional losses are caused and the torque ripple are created [134]. Additionally, as mentioned above, these methods are only applicable for interior PMSM (IPMSM) [147, 148]. Since the PMSM that targeted by the industrial project in this chapter is not an IPMSM,

the HF injection method is not considered. Next, the convergence for the observer is questionable, which will cause a large estimation error. In the end, introducing an injection signal is a challenge to the power converter used, the cost for the whole system is increased.

In industrial applications, the model-based methods are more commonly applied because they are easy to implement. However, the performance of the model-based methods are poor at low speed. In such condition, the back-EMF became very small, and the voltage drop on the resistor and inductance became dominate [149]. In that case, the model-based methods are not an ideal approach to identify the rotor position.

Fortunately, the only inevitable low speed operation is when the machine is starting up. If the machine is already accelerated, the model-based algorithms are reliable. A feasible approach is to start the PMSM with an open loop controller, then switch to a sensorless closed loop when the rotor speed is high enough. The open loop start method is introduced in Section 4.2.

4.2 PMSM Open Loop Start

The rotor flux of a PMSM is built with permanent magnets (PMs) in the rotor. The FOC method demands a accurate rotor flux direction so that the $d-q$ axis current can be properly decoupled. In the process, the vector diagram is shown in Figure 4.4. However, when the rotor flux direction is not properly identified, the stator currents (I_{s1} or I_{s2}) will still be decoupled by the rotor dq reference frame, shown in d_{rotor} and q_{rotor} in Figure 4.4. In that moment, only the current vector that perpendicular to rotor flux, i.e. i_{q1} or i_{q2}, will contribute to the torque generation, and the torque direction is decided by the direction of i_q . The d-axis currents i_{d1} or i_{d2} will not influence the torque direction. They are not shown in the diagram.

The main idea of starting a PMSM in an open loop way is to keep the torque direction constant in the process. The method proposed by M.Fatu in [150] suggests to apply a rotating stator current vector I_s with a ramping speed. In this way, the machine is started by the generated torque, and as the rotor and the I_s are rotating together, the i_q can be kept in a constant direction so that the torque direction will also be constant. This method is referred to as the “I-f” method.

For the ”I-f” starting, the stator current frequency ramp should not be too steep. The purpose of the ramping frequency is to guarantee that the rotating

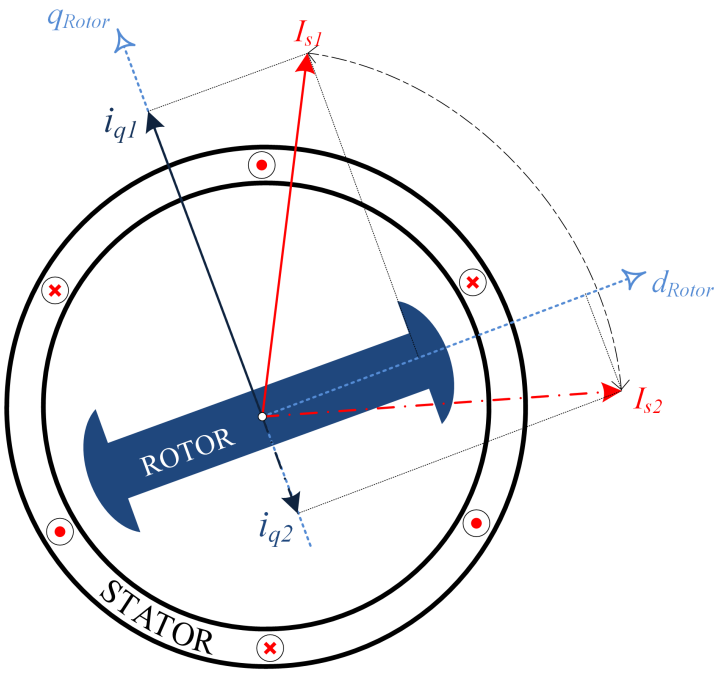

Figure 4.4: PM open-loop start vector diagram

speed of the stator current vector is comparable with the rotor speed. Otherwise, when the relative position of I_s and the rotor in Figure 4.4 changes from I_{s1} to I_{s2}, the torque generate current component changes from i_{q1} to i_{q2}, and the generated torque becomes negative. This whole start up process is in the same manner as dragging the rotor with a spring. The rotor speed and torque will become consistantly oscillation. This characteristics are clearly observed in the hardware test results in the next section.

4.2.1 Hardware Tests for "I-f" Starting

The "I-f" Starting is widely introduced in industrial applications. Its performance depends on particular physical conditions of the machine, which cannot be perfectly shown in the simulation. Hardware experiments are carried out on a 50 kW test rig in this section.

In the tests, the PMSM is started with the "I-f" method, three frequency ramps are applied, results are shown in Figure 4.5 to Figure 4.7.

For slower speed ramp (Figure 4.5), the starting process is more smooth. However, oscillation can be observed during the acceleration process. As a continuous

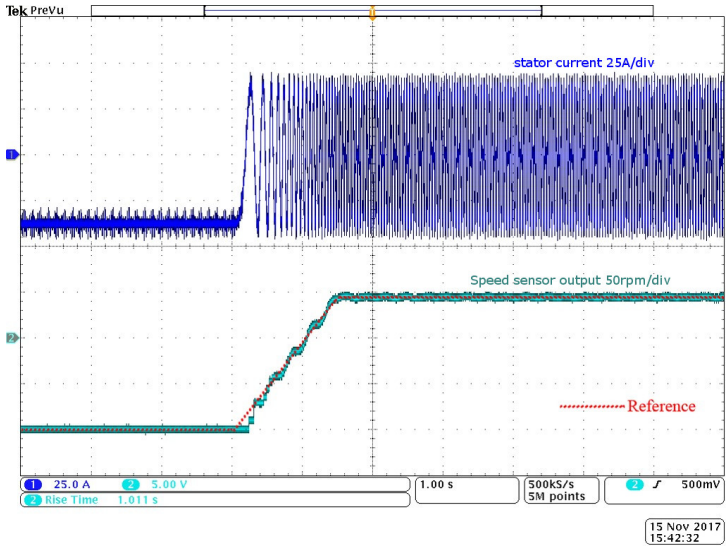

Figure 4.5: PM open-loop start hardware test (100 rpm/s)

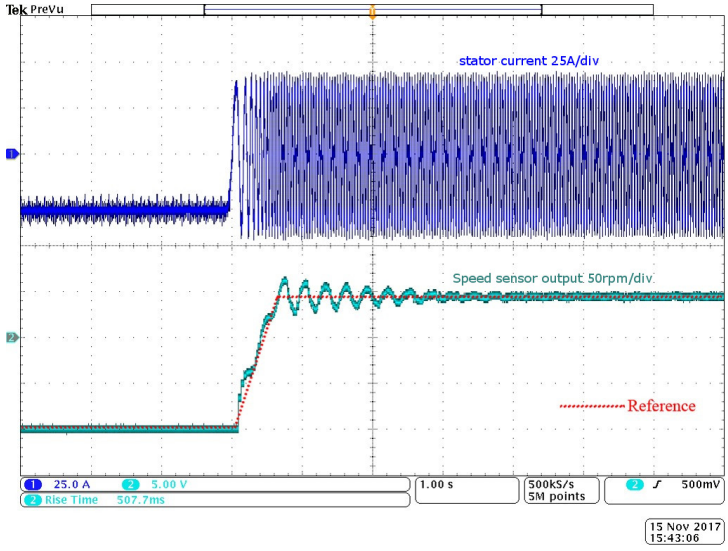

Figure 4.6: PM open-loop start hardware test (200 rpm/s)

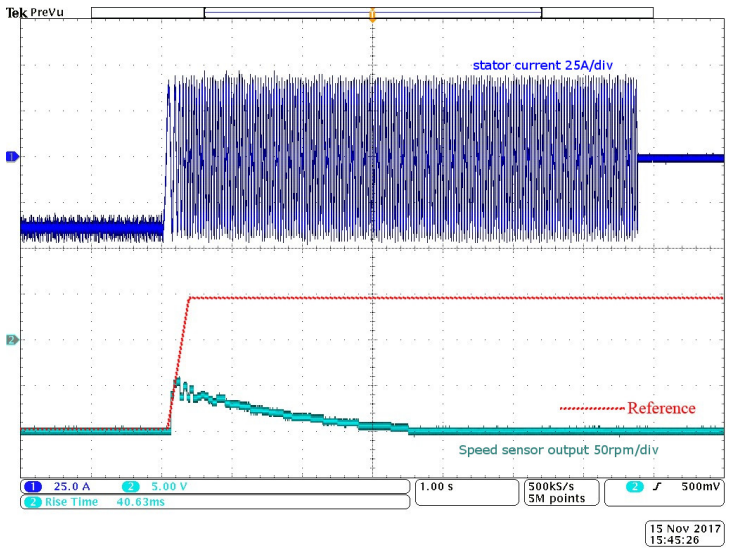

Figure 4.7: PM open-loop start hardware test (350 rpm/s)

test, steeper accelerate ramp are tested, shown in Figure 4.6 and Figure 4.7.

In Figure 4.6, when the acceleration ramp is doubled (200 rpm/s), the oscillation is larger, which lasted after reference speed is reached. In Figure 4.7, the ramp increases to 350 rpm/s, the rotor stopped tracking the reference. After a short oscillation session, the rotor speed dropped to zero, since the positive and negative torque is equal in each period, the rotor stopped by freewheeling.

In Figure 4.5 to Figure 4.7, the stator current figure (upper figure in the oscilloscope screen shots) is only showing one phase of the three-phase stator currents. In this open-loop tests, before the beginning of the process, a d-axis DC current reference is given to the stator so that the machine rotor position is aligned to the initial position of the stator flux linkage. In that case, before the machine starts ($t < 3s$), all of the three-phase currents are DC currents. They are the results of the reversed Park transformation of the DC d-q currents. It is normal that one or two of the phase current(s) is negative.

In conclusion, when starting PM machine with the "I-f" method, the selection of a proper acceleration ramp is very important. The ramp should not be too steep. The load torque and the magnitude of a given voltage vector should also be taken into consideration.

In most marine application cases, PMSM is the propeller, in which the load is proportional to the square of rotation speed, which means that when the motor is starting, the load torque is very small. Thereby, the "I-f" starting method is

achievable in low torque working conditions.

4.3 Back EMF Based Sensorless Control

After the machine is accelerated with the "I-f" starting method, its controller will be switched to a sensorless FOC. Model-based rotor position estimation has been achieved with multiple approaches. In this section, the sliding mode observer (SMO) is introduced.

4.3.1 Back EMF Estimation with Sliding Mode Observer

The SMO for rotor position observation consists of a nonlinear current observer, and the control signal is applied in the estimation of the back EMF. The current observer is derived from the mathematical model of PM, shown in Equation (4.1).

$$\begin{cases} \frac{d\hat{i}_\alpha}{dt} = -\frac{R_s}{L_1}\hat{i}_\alpha + \frac{1}{L_1}v_\alpha - \frac{1}{L_1}Z_\alpha \\ \frac{d\hat{i}_\beta}{dt} = -\frac{R_s}{L_1}\hat{i}_\beta + \frac{1}{L_1}v_\beta - \frac{1}{L_1}Z_\beta \end{cases} \tag{4.1}$$

where $\hat{i}_\alpha$ and $\hat{i}_\beta$ are the observed value of stator currents. Reference signal of v_α and v_β are applied to the equation. L_1 and L_2 can be calculated as Equation (4.2) with inductances L_d and L_q in rotor flux reference frame.

$$\begin{aligned} L_1 &= \frac{L_d+L_q}{2} \\ L_2 &= \frac{L_d-L_q}{2} \end{aligned} \tag{4.2}$$

Z_α and Z_β are the control signal which is presented in Equation (4.3).

$$\begin{cases} Z_\alpha = k \cdot sgn\left(\hat{i}_\alpha - i_\alpha\right) \\ Z_\beta = k \cdot sgn\left(\hat{i}_\beta - i_\beta\right) \end{cases} \tag{4.3}$$

In Equation (4.3), *sgn* stands for the signal function whose result equals to ± 1 depending on the sign of current estimation error. k is the coefficient of the current SMO.

If convergence is achieved with the current SMO, the current error $\widetilde{i}_{\alpha,\beta} =$

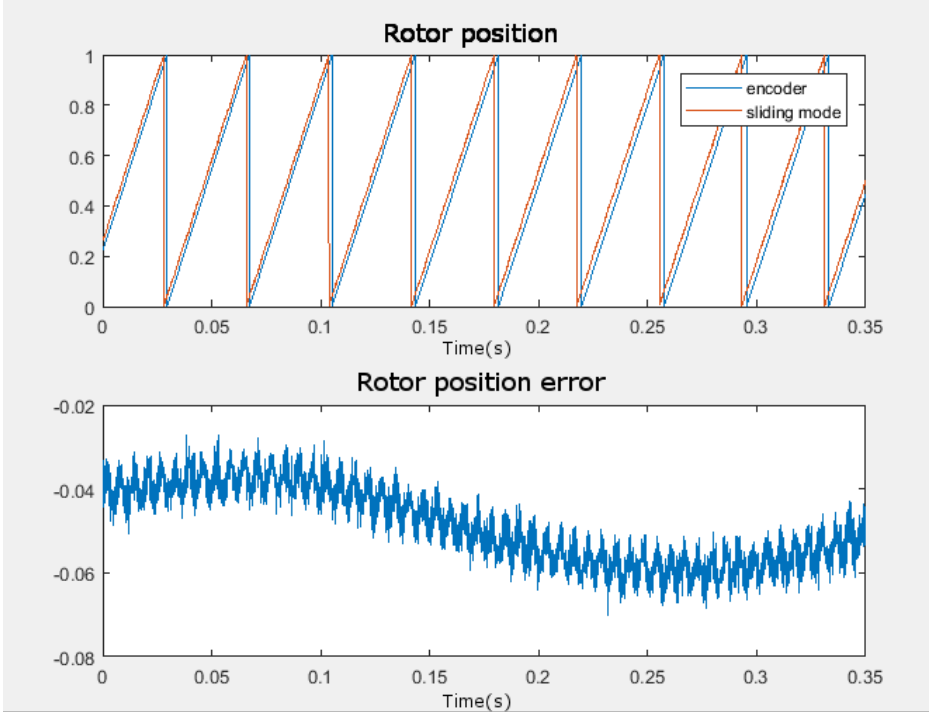

Figure 4.8: Sliding mode observer time delay

$\hat{i}_{\alpha,\beta} - i_{\alpha,\beta}$ become zero. Equation (4.4) is achieved.

$$\begin{cases} z_\alpha = e_\alpha = -\phi\omega_e \sin(\theta_e) \\ z_\beta = e_\beta = \phi\omega_e \cos(\theta_e) \end{cases} \tag{4.4}$$

The control signal in Equation (4.4) is equivalent to the back EMF value in the $\alpha - \beta$ axis. As the rotor position share the same direction with the rotor flux, its angle $\hat{\theta}_e$ can be found with Equation (4.5).

$$\hat{\theta}_e = \arctan\left(-\frac{z_\alpha}{z_\beta}\right) = \arctan\left(\frac{-\phi\omega_e \sin(\theta_e)}{\phi\omega_e \cos(\theta_e)}\right) \tag{4.5}$$

The rotor speed is the differential of the rotor position. On the 50 KW test rig in Section 4.6.2, the SMO is applied, the estimation results are compared with the encoder outputs (Figure 4.8). The estimation error is caused by multiple reasons, one of them is the time delay introduced by the low pass filter (LPF), which will be introduced in the next section.

4.3.2 Low Pass Filter Applied for Sliding Mode Observer

Chattering need to be reduced when the SMO is implemented. A low pass filter (LPF) is necessary. At the same time, a time delay will be introduced to the estimation result. As the position information is applied to the decoupling of $d-q$ axis current, the error introduced by time delay will be amplified.

In the experiment test, the parameter $k_{slf} = 0.3$, which lead to a transfer function of

$$sysz = \frac{0.3z}{z - 0.7} \tag{4.6}$$

The cut off frequency is about 500 Hz, in 144 rpm, the theoretical time delay is about 0.0108 pu.

The rotor position error is shown in Figure 4.8 is around 0.04 pu. However, this error may not caused by the LPF time delay entirely. For example, the error in the measurement of stator current will lead to an error in the SMO result. Additionally, there is a chance that the encoder output has an error. Nonetheless, compensation on the low pass filter time delay will reduce the error.

From another perspective, the motivation of introducing the LPF is to avoid chattering issue. It is not necessary to introduce a LPF otherwise. One method is to replace the e signum function with a sigmoid function [151]. Another approach is to replace the SMO with a super-twisting algorithm [134]. In that case, the low pass filter is not compulsory anymore, neither the time delay compensation.

4.3.3 Robustness Test for Sliding Mode Observer

As a model-based method, the robustness test against parameter variation is necessary. The robustness of L_s and R_s are tested.

In this hardware test, it is difficult to change the actual motor parameters. Instead, the parameter used in the observer is changed intentionally. Their values are changed $\pm 50\%$ each. This parameter variation is reasonable in real conditions due to a change in temperature. The experiment test results are shown in Figure 4.9. In all conditions, the identified rotor angle is similar. Since encoder output is trustworthy, the error is kept within a certain range, which implies the SMO output is robust against parameter variations.

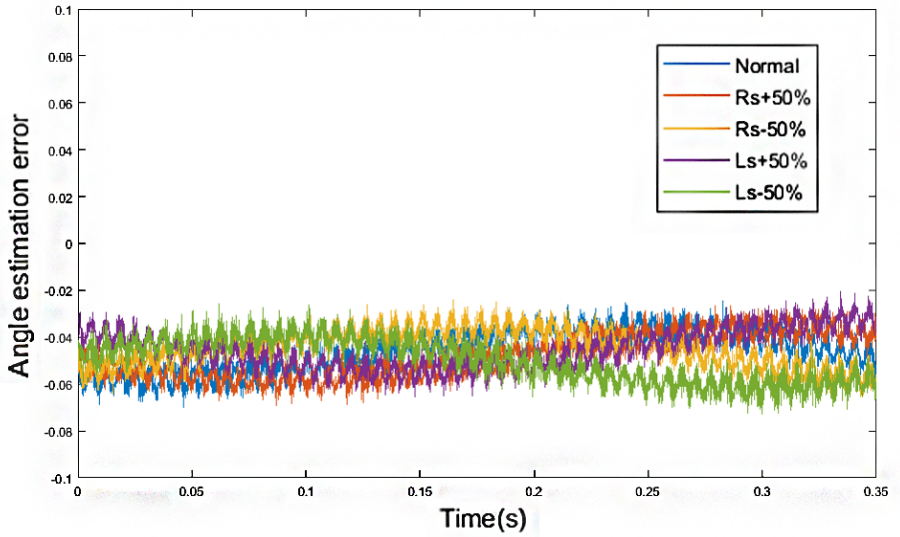

Figure 4.9: Sliding mode observer robustness test

4.4 Smooth Transition Method

In Section 4.2 and Section 4.3, the open loop start "I-f" method and sensorless control based on back EMF are proved to be reliable. In this section, the transition method between these two control algorithms will be discussed.

When the machine is accelerated, the back EMF is large enough so that position can be appropriately estimated. The control loop is closed with the estimated value as the feedback. In general industrial applications, the transition from open loop to closed loop is the direct switch, i.e., change the stator current i_d and i_q directly from "I-f" method reference to the SMO controller's output. Since their difference in both magnitude and direction are large, sizeable transient current peak is created. This current peak also triggers noise and potential physical damage to the machine.

In this section, a novel method is proposed for a more smooth transition procedure. This method is derived from the open loop operation characteristics. Firstly, the transient issue from open loop to FOC is discussed, and the proposed smooth and fast transition method is illustrated. Next, the simulation and hardware test results are shown.

4.4.1 Transient Issues From Open-Loop to FOC

In the transient from the open loop to close loop FOC, the reference signal will suffer a large variation in a short time. This sudden change will lead to multiple consequences.

- Large current transient
- Large torque vibration.
- Noise during the transition

This transient issue can be illustrated by the sudden change in reference current. As introduced in Section 4.2, when the motor is running in open loop, the stator current can be considered as a vector with ramp increasing frequency. It will be decoupled by the actual rotor position. The electric magnetic torque is generated as Equation (4.7). It should be pointed out that the rotor direction is not necessarily aligned with this stator current vector.

$$T_e = \frac{3}{2} P \left[\Psi i_q + (L_d - L_q) \, i_d i_q \right] \tag{4.7}$$

Note that the actual electric magnetic torque T_e generated should always be following the torque balance, i.e., $T_e = T_L$. When a motor is starting the load torque T_L is very small, thus T_e required is very small as well. In the meantime, in a open loop start with the "I-f" method, the magnitude of the current vector I_s is given as constant, and it is set exceedingly large than the I_q required to guarantee the motor start.

After the motor started, the torque balance is achieved in an electric mechanical process. The current vectors relationships in both reference frames are shown in Figure 4.10. Take the condition when T_e is larger than T_L as an example, the rotor will accelerate and θ_{err} will become larger. When θ_{err} is larger, the i'_q component will become smaller and T_e will also become smaller. The condition when T_e is smaller than T_L is similar. The same process repeats until T_e and T_L is finally balanced, the θ_{err} becomes constant.

It can also be derived from this small signal analysis that when the motor is started in an open loop approach, the stable operation point can be reached only when i_q located at the I-quadrant of the coordinate system composed by q_{rotor} and d_{rotor} in Figure 4.10. The electric torque equation that contains θ_{err} can be

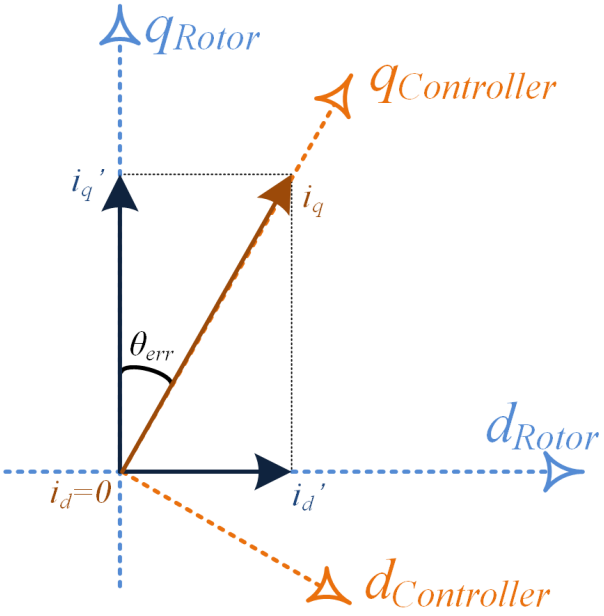

Figure 4.10: θ_{err} in open loop operation

derived as Equation (4.8).

$$T_e = \frac{3}{2}P\left[\Psi i_q \cos\left(\theta_{err}\right) + \frac{1}{2}\sin\left(2\theta_{err}\right)\left(L_d - L_q\right) i_q^2\right] \tag{4.8}$$

Two assumptions are made to simplify the analysis. Firstly, the current reference vector will keep a constant frequency once the desired speed is achieved. Second, the reluctant torque of PMSM is minimal. In another word, $L_d - L_q \approx 0$, so that the second part in Equation (4.8) can be neglected.

Find the differential of Equation (4.8) against θ_{err} as Equation (4.9).

$$\frac{dT_e}{d\theta_{err}} = -\frac{3}{2}P\Psi i_q \sin\left(\theta_{err}\right) \tag{4.9}$$

It is obvious in Equation (4.9) that if $\theta_{err} \in (-90°, 0°)$, the value of $\frac{dT_e}{d\theta_{err}}$ is positive, while it should be negative to maintain the motor system work stable. It is proved that when the motor is running in a steady-state open loop, i_q is always located at I-quadrant in Figure 4.10.

4.4.2 Proposed Smooth and Fast Transition Method

The machine conditions before the transition are discussed in Section 4.4.1.

Before transition, the motor is started in open loop, and its stator flux vector direction could only locate at I-quadrant in Figure 4.10. In order to guarantee the machine start, an extensive magnitude of i_q reference will be introduced to the motor. The sufficient current will contribute to the torque while the exceeding is decoupled as the d-axis components.

After switched to a closed loop FOC, i_q is the reasonable value which is enough to counter the load torque, while the reference of i_d is commonly set to zero in a PM machine controller. During the switching process, the current will change violently.

The critical point for the smooth transition from position open loop control to FOC is to find a method that can reduce the dq-axis currents and error angle θ_{err} smoothly.

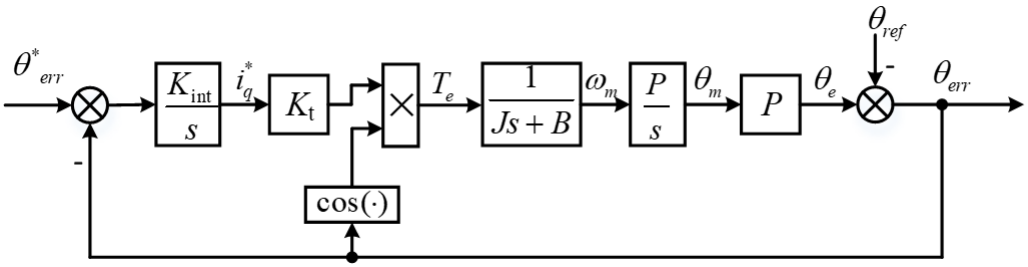

Figure 4.11: Proposed smooth transition method

An integral closed-loop method is proposed to reduce the current command before the switching. The proposed control diagram during the transition process is shown in Figure 4.11. Where the current loop of the motor system is treated as a proportional block K_t for the simplicity. And the control law can be shown as Equation (4.10), where K_{int} represents the integral gain designed for the transition, T_s is the sampling time of this discrete time system.

$$i_{q(K+1)} = i_{q(K)} - K_{int}\theta_{err}T_s \tag{4.10}$$

In Figure 4.11, the initial value of the integrator is set to the reference value of i_q in the open loop start method. The reference value $\theta_{err}*$ is a small value defined, which means it is safe to switch to closed loop.

The proposed method works with the natural saturation that built in the

current i_q loop. With the θ_{err} drops, the q-axis current reference i_q^* drop gradually. The drop of i_q will make the rotor misalignment angle smaller as described in Section 4.4.1.

One can also decrease the i_q^* by manually giving a changing ratio limitation so that its value will drop linearly. However, due the variable load conditions, it is impossible to decide a perfect ratio in industrial applications. On the other hand, the proposed method is realized in closed loop, which is more robust. It is verified in two hardware test rigs with largely divergent power ratings (3 kW and 50 kW) to show the robustness of the proposed switching approach.

4.5 Simulation Results

The simulation is carried out with MATLAB SIMULINK. The same machine parameters of the 50 kW PM rig are applied to the PM motor model to keep the simulation results more comparable to industrial applications. The machine and test rig is introduced in a later Section 4.6.2, and the motor parameters are given in Table 4.2. Figure 4.12 shows direct transition results. The controller transition speed is set to 15% of the motor rated speed, which is about $144rpm$. Transition time is set at $t = 2s$. Figure 4.13 show the results with smooth transitions. The transition process also starts at $t = 2s$, however, with the help of the smooth transition algorithm, the i_q current decrease gradually , After about 1 second, the controller switched to the closed loop FOC (Figure 4.13a).

From the simulation results, the following observations are made.

- Firstly, when the machine is started with an open loop approach, both Figure 4.12a and Figure 4.13a show that the speed oscillates in the rising process. This result demonstrates the analysis made in Section 4.2. Additionally, it visualizes the expression of "dragging the rotor with a spring". It is also observed when the motor operates to an open loop steady state, the speed oscillation turn smaller with time.

- Secondly, in the simulation result, only the transient currents are shown. In the hardware test results (Figure 4.21c), the direct transition also brings noise and physical vibration, these phenomenon cannot be observed from simulation.

- Thirdly, from the rotor speed point view in Figure 4.12a and Figure 4.13a,

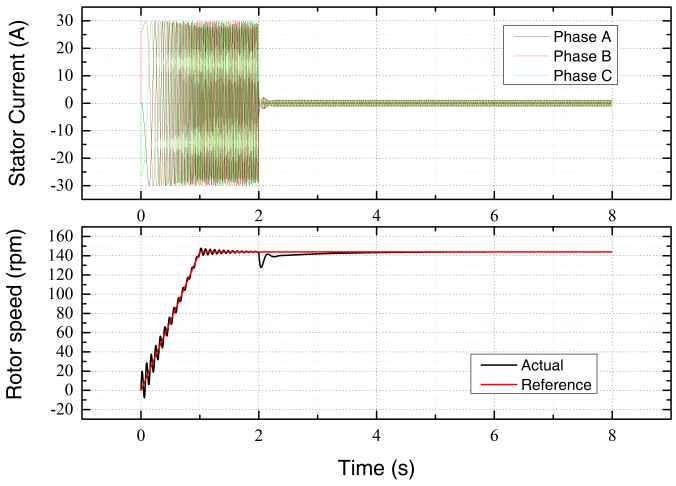

(a) Stator current and speed

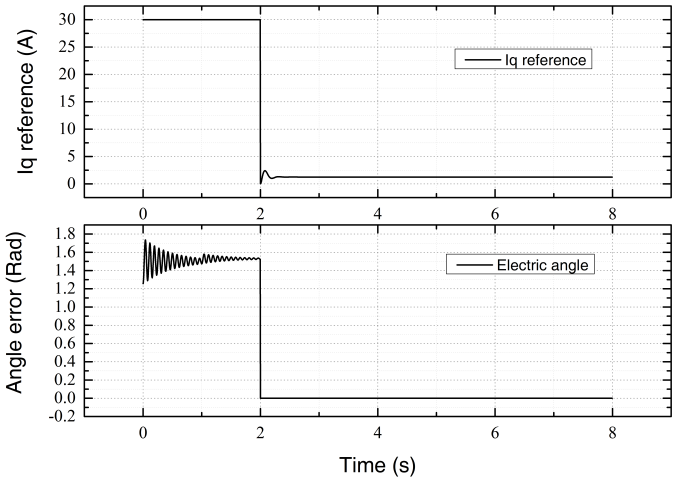

(b) Q-axis reference current and angle error

Figure 4.12: Simulation on open loop to FOC: direct transition

after applying a smooth transition, the speed variation during the switching transient is smaller.

- Lastly, the angle error in Figure 4.12b and Figure 4.13b are close to $1.5rad$ when the motor is starting. In electric angles, it is about 85.94°, which is really close to 90°. That implies the i_q reference current is far larger than the real i_q required. Most of the current vector is decoupled to the i_d vector. The real i_q that contributes the torque to counter friction and load can be

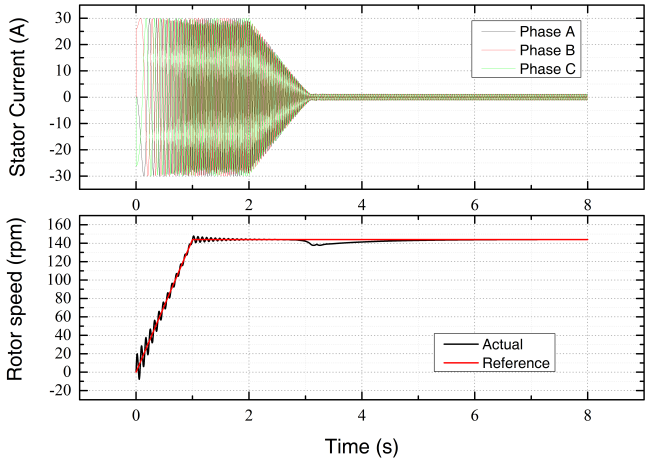

(a) Stator current and speed

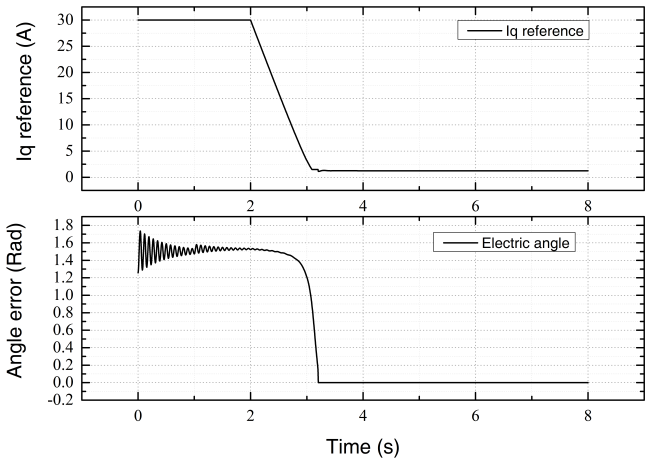

(b) Q-axis reference current and angle error

Figure 4.13: Simulation on open loop to FOC: smooth transition

calculated as Equation (4.11). i_{q-q} share the same definition from Figure 4.10.

$$i_{q-q} = cos(85.94°) * i_q \simeq 0.071 * i_q \tag{4.11}$$

In the simulation model, the friction factor is constant, when the motor is starting, the friction can be ignored. However, in the hardware test, the friction is large particularly in the starting stage, thus a large starting curent i_q is required.

To simulate real conditions, the open loop starting current i_q is set very large.

Another important factor is the initial position. If the motor starts with the stator current vector overlaps with the rotor flux direction, the initial torque will be zero. In that case the torque is increased gradually and the speed oscillation is minimized. Thus it is proved to be an ideal initial position. The simulation results are shown in Figure 4.14. In Figure 4.14, initial position is set to $\theta_{ini} = k * 90°$. It is shown that oscillations are smaller when k is closer to 1.

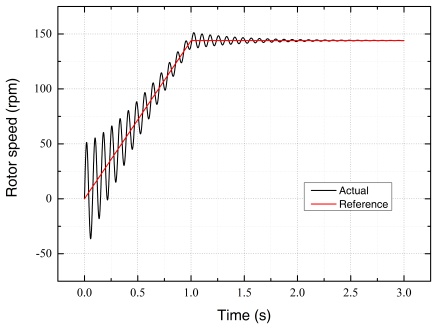

(a) Initial position $k = 0.5$

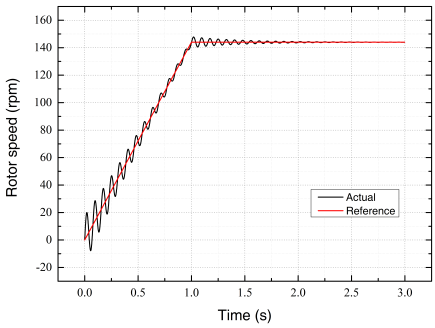

(b) Initial position $k = 0.8$

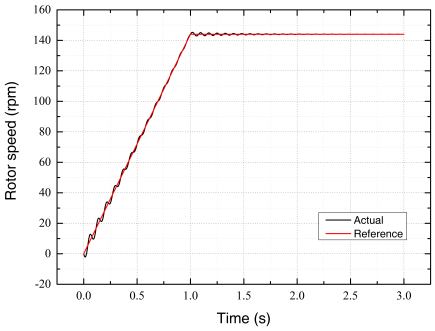

(c) Initial position $k = 1$

Figure 4.14: Open loop start with different initial position

In the hardware test, the ideal initial position is reached after the DC current is injected. The target is to set the initial angle to $\theta_{ini} = 90°$. However, since the machine has 11 pole pairs, an electric angle 90° converted to the physical angel is only 8.18°, whose accuracy is hard to guarantee. In the simulation, the comparable condition of $k = 0.8$ is applied, which is a close to the ideal initial position, but not exactly the same.

4.6 Hardware Test

The experiments for the smooth transition method are carried out on both the 7.5 kW and 50 kW PMSM. In this section, the hardware rigs are briefly introduced. Then the hardware test is carried out on both hardware test rigs. Experiment results are shown in Figure 4.16 to Figure 4.22.

4.6.1 Test Results on the 3 kW PMSM

3 kW PMSM Test Rig Setup

The 3 kW PMSM test rig is shown in Figure 4.15. On the motor side (Figure 4.15b), a $7.7kW$ PMSM is coupled with a 3 kW hysteresis brake dynamometer (Magtrol HD 810-8N). The specifications of the PMSM are listed in Table 4.1. It should be pointed out that the $7.7kW$ PM machine inertia is not provided by its manufacture. The Magtrol HD 810-8N dynamometer has inertia 0.006 kgm^2. considering that the PMSM and the dynamometer share the equivalent size, the combined inertia is estimated as $0.012kgm^2$.

Table 4.1: Specifications of 7.7 kW PMSM

Specifications	**Value**
Rated current (A)	27.7
Rated speed (rpm)	3150
Rated torque (Nm)	31.8
Inductance L_d (mH)	1.089
Inductance L_q (mH)	2.606
Measured Resistance R_s (Ω) @150 Hz	0.176
Inertia J (kgm^2)	0.012
Calculated PM flux (Wb)	0.18
Pairs of poles	3

Dynamometers are ideal equipments for tests under low to medium power. It can provide a torque without speed due to its hysteresis brake characteristics [152]. This installed model is capable of generating load torque at a maximal of $14N.m$.

The controller system configurations are shown in Figure 4.15a. The setup for

inverter and DC power source are similar to the IM test rig introduced in Section 3.6.1. It is not repeated here for conciseness.

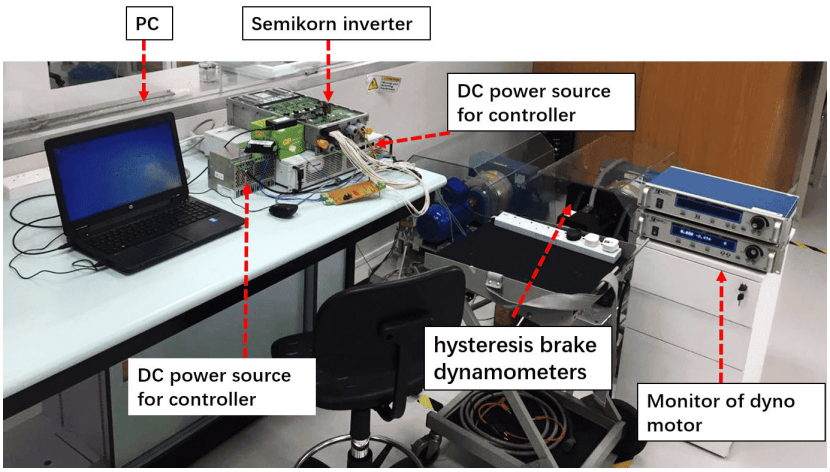

(a) Inverter and DC power source

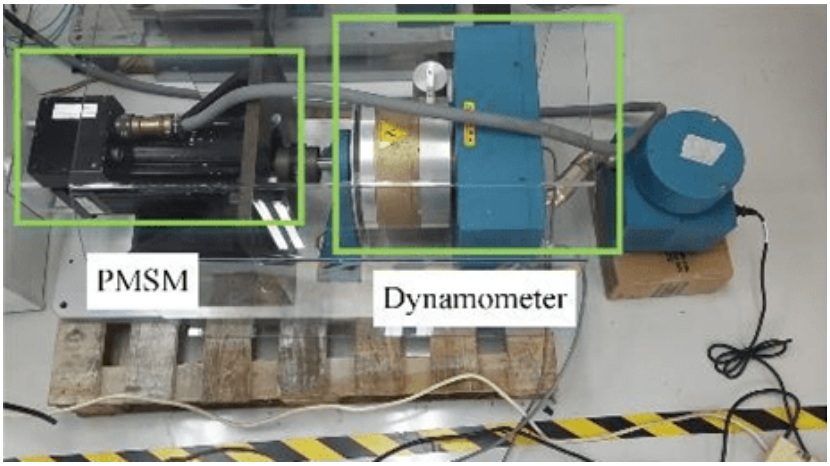

(b) PMSM and dynamometer

Figure 4.15: 3 kW PMSM test rig

Test Results on the 3 kW PMSM

For the 3 kW PMSM machine, the experiment results on the proposed smooth transition method are provided in Figure 4.16 and Figure 4.17, the direct transition method is also tested for comparison. In both methods, transition time is set to $t = 1s$.

In Figure 4.16(a), before the transition the initial error angle is around 65°. While the proposed method reduces the error angle gradually to zero, the direct

transition method just switches the angle directly . Although it seems the direct transition method is faster than the proposed method, it introduces much higher speed overshoot and larger current oscillations. Test results are shown in Figure 4.16 (b)-(d). If the system has smaller inertia, the speed overshoot will be even larger.

On the contrary, the speed response of the proposed method is much smoother during the transient process, the speed variation is within 50 rpm. Although there is a spike in the estimated velocity of the direct transition method (Figure 4.16(c)), it is not observed in real velocity (Figure 4.16 (d)). The reason for this phenomenon is that the currents and voltages are oscillating under the direct transition method, speed estimation result is not correct in transient. One should be noted that the speed calculation and control period is $1ms$, rather than the current measurement and control period $0.1ms$.

The stator current result gives a better view of the improvement of the smooth transition method. The single phase stator current variation during the transition is logged by the oscilloscope, shown in Figure 4.17. For both methods, it is clear on the scope that when the motor is running under the open loop strategy, the stator current is very large, after the transition, the stator current required is depend on the torque balance and guided by the FOC algorithm. The experiment results match the analyses in Section 4.4.1. The proposed method focuses on improving the transient, the current spike caused by direct transition is marked with a red oval in Figure 4.17a. As a comparison, in Figure 4.17b, smooth transition algorithm is applied, and the current spike is eliminated.

4.6.2 Test Results on the 50 kW PMSM

The 50 kW PMSM test rig provides a test environment which is more close to industrial applications. Transition noise is more evident on larger machines than the small ones. Additionally, with the help of a torque sensor, the torque transient is observed more clearly.

50 kW PMSM Test Rig Setup

The 50kW PMSM and IM rig is shown in Figure 4.18. The PMSM consists of six-phase windings and surface mounted PMs. In the test, the six-phase windings are connected two by two in parallel and form into two ordinary three-phase machines. The stator winding configuration is as Figure 4.19. In future works,

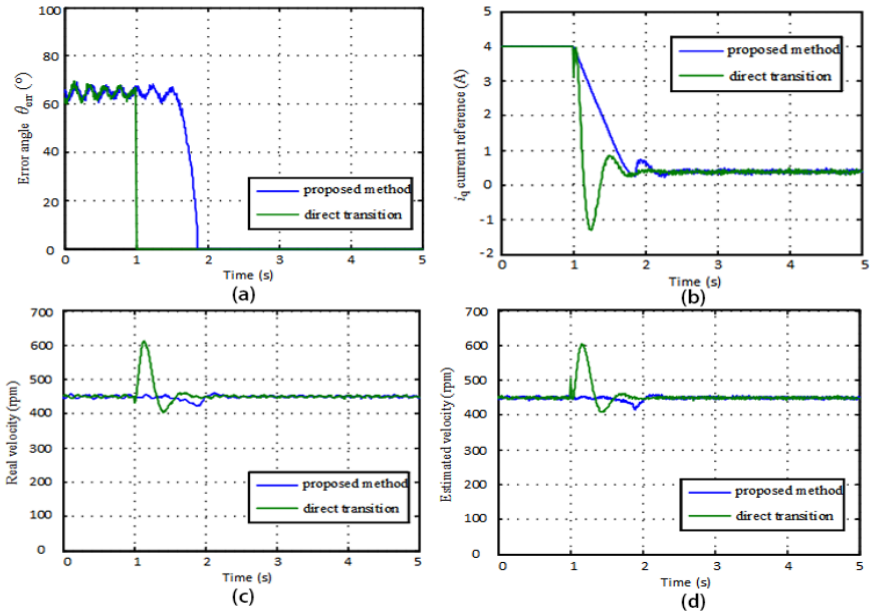

Figure 4.16: Hardware results for transition control: 3kW.
(a) is the error angle Θ_{err}, (b) is the i_q current reference, (c) is the actual speed response and (d) is the estimated speed response.

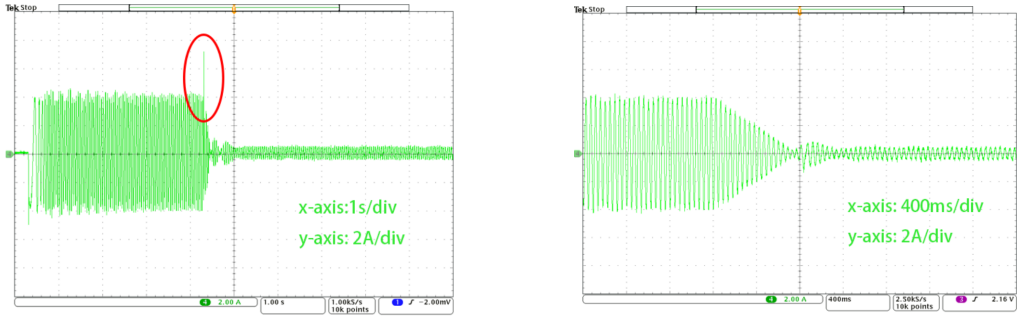

(a) Direct transition (b) Smooth transition

Figure 4.17: Single phase stator current comparison: 3kW
Red circle: current spike during direct transition

the connection will be decoupled to test as a dual stator winding PMSM. This PMSM is also equipped with temperature sensors, and search coils for machine health monitoring.

An IM is coupled on the shaft as load. However, both machines can be used as either generator or motor. There is a "KISTLER" torque sensor placed along

the shaft, which will log the shaft torque.

The specifications of this PMSM are listed in Table 4.2. The inertia here represents the estimated inertia for the PMSM only. Since the PM machine rotor has larger radius, its inertia is larger than the IM with equivalent size. Additionally, the combined inertia of the whole test rig should be considering the inertia of the shaft.

Table 4.2: Specifications of 50kW PMSM

Specifications	**Value**
Rated current (A)	84.65
Rated speed (rpm)	960
Rated torque (Nm)	583.4
Inductance L_d (mH)	880
Inductance L_q (mH)	880
Measured Resistance R_s (Ω) @26.4Hz	0.015
Inertia J (kgm^2)	4
Calculated PM Flux (Wb)	0.253
Pairs of poles	11

Test Result on 50 kW PMSM

The hardware test results are shown in Figure 4.20. As required by the industrial applications, the PM motor is accelerated to 15% of the motor rated speed (144 rpm) with an open loop controller. Then motor controller switched to a sensorless FOC with SMO. In both smooth and direct transitions, they are made at $t = 1.6s$ after data logging begins.

Figure 4.20(a) shows the change of i_q reference value in both transition methods. With smooth transition (black curve) the i_q reference gradually drops to the closed loop reference value, on the other hand during the direct transition (red curve), the i_q reference drop immediately. As a result, a large overshoot is caused. Figure 4.20(b) shows the angle error between the open loop reference angle and the sliding mode observed angle. In open loop, the angular misalignment is around 70 degrees (electrical angle). The smooth transition shows a gradual

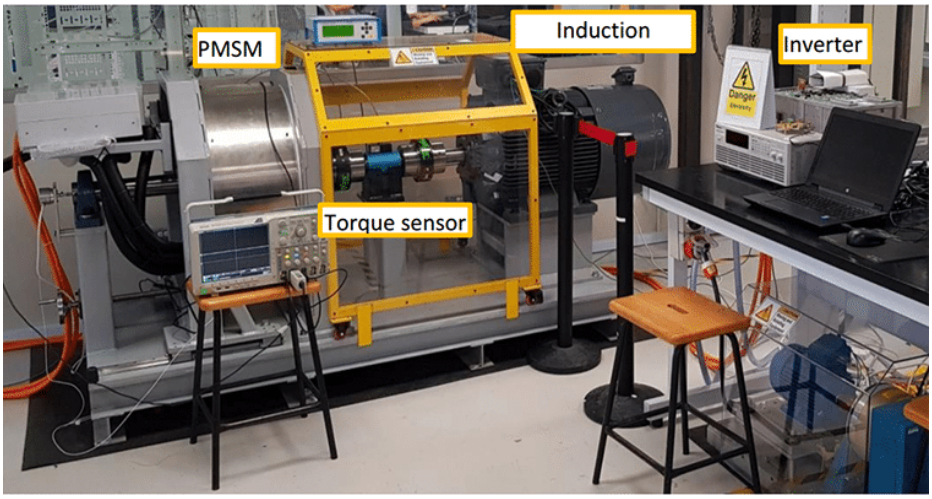

Figure 4.18: 50 kW test rig of PMSM and IM

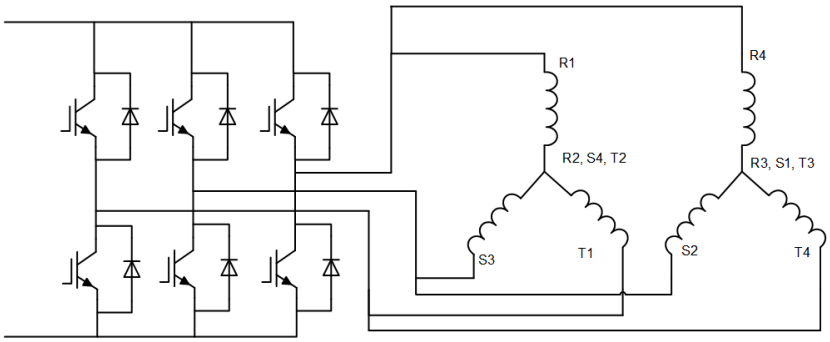

Figure 4.19: The stator windings of the 50 kW PMSM

drop in the error angle similar to i_q current. These hardware results are close to the simulation results in Figure 4.12 and Figure 4.13. The difference is that in hardware test, the initial angle difference is about 70°, while in simulation it is about 86°. Since the difference is constant, the difference is most likely to be caused by the time delay in the speed estimation.

Figure 4.20(c) and Figure 4.20(d) show the speed variation observed by the encoder and the SMO respectively. Although the encoder information is not applied to the algorithm, it is captured for comparison. Both results show that speed fluctuation is larger in direct transitio than in smooth transition. In contrast to the test in 3 KW rig, the difference is not very obvious. That is because the motor is working on a lower speed. However, it is observed clearly from the oscilloscope measurements.

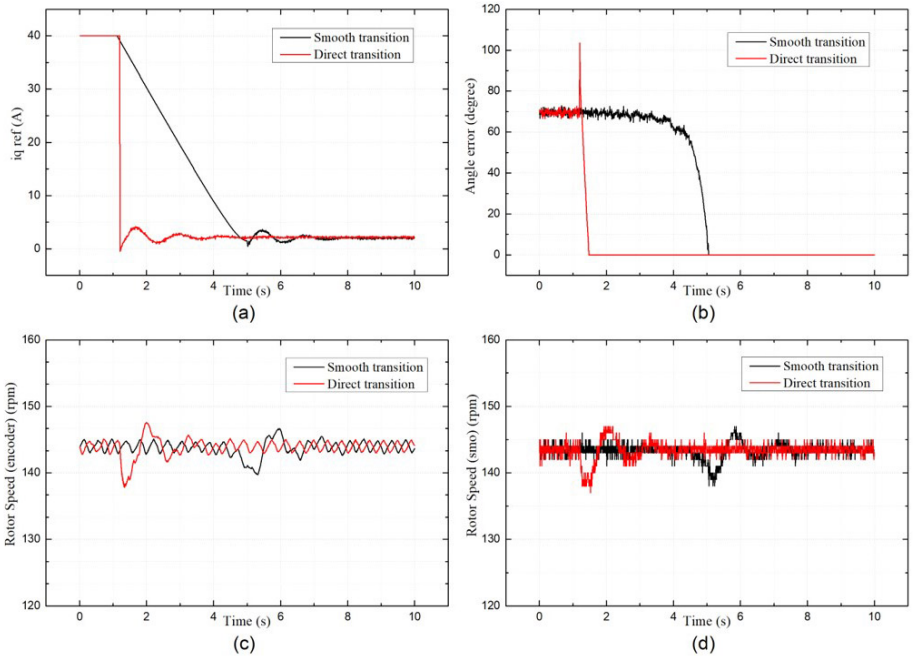

Figure 4.20: Hardware results for transition control: 50kW.
(a) is the error angle θ_{err}, (b) is the i_q current reference value, (c) is the actual speed response and (d) is the estimated speed response.

The oscilloscope screenshots that taken from the same experiment are shown in Figure 4.21. Figure 4.21b is from smooth transition, while direct transition is shown in Figure 4.21a and Figure 4.21c. Figure 4.21c is a zoomed-in view of Figure 4.21a. In the scope screenshots, channel one is the single-phase stator current. Channel two show the speed. Channel three shows the torque signal read from the torque sensor placed on the shaft between the two motors. It is observed in Figure 4.21c that during the direct transition there is a $106A$ overshoot. Although the duration period is very short, a clear and heavy sound can be heard during hardware experiment. Channel two represents the speed read from the torque sensor. This speed results cannot be used for any control proposes due to the poor resolution ($60 pulses/rotation$), it is shown on the scope plotting just as a reference. By comparing Figure 4.21a and Figure 4.21b. There is a significant torque ripple (violet curve) during the direct transition.

The smooth transition is also tested in lower speed conditions. In lower speed, the challenge is that the SMO cannot achieve accurate rotor angle. Experiments are done for the rotor speed of 10% and 5% of the rated rotor speed. The exper-

iment results are shown in Figure 4.22. Figure 4.22a and Figure 4.22b show the results at 10% of the rated rotor speed (96 rpm). The smooth transition method works well under this condition. Figure 4.22c and Figure 4.22d show the results for smooth transition and direct transition at 48 rpm, respectively. Results show that in 5% of the rated rotor speed, the direct transition method stopped working (Figure 4.22c), the speed drops to zero rapidly while the system suffers a large oscillation. On the contrary, this issue is fixed by introducing the proposed smooth transition method, as shown in Figure 4.22d. For lower rotor speed, the system is more vulnerable to the current pulses during the transition, the potential minimum transition speed is decided by the motor set up and the particular experimental conditions.

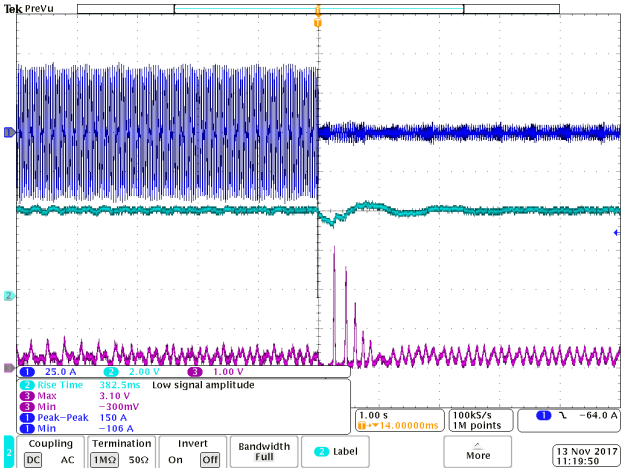

(a) Direct transition

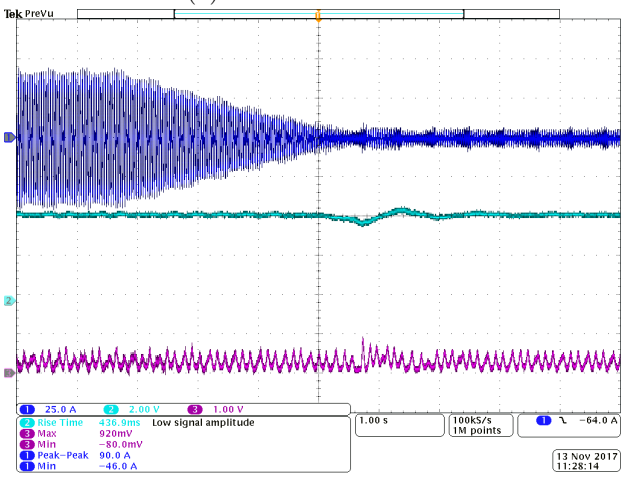

(b) Smooth transition

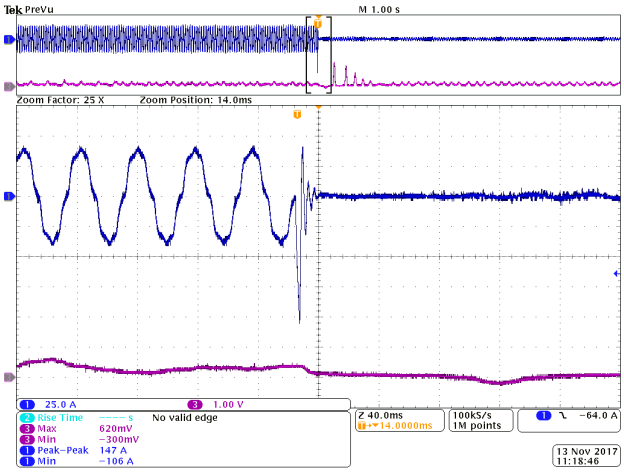

(c) Smooth transition: zoom-in

Figure 4.21: Single phase stator current comparison: 50kW (15% rated speed. Blue curve: stator current in 25 A/div. Green: rotor speed in 10 rpm/div. Purple: torque sensor in 10 Nm/div. Time: 1 s/div for (a)(b), 40 ms/div for (c))

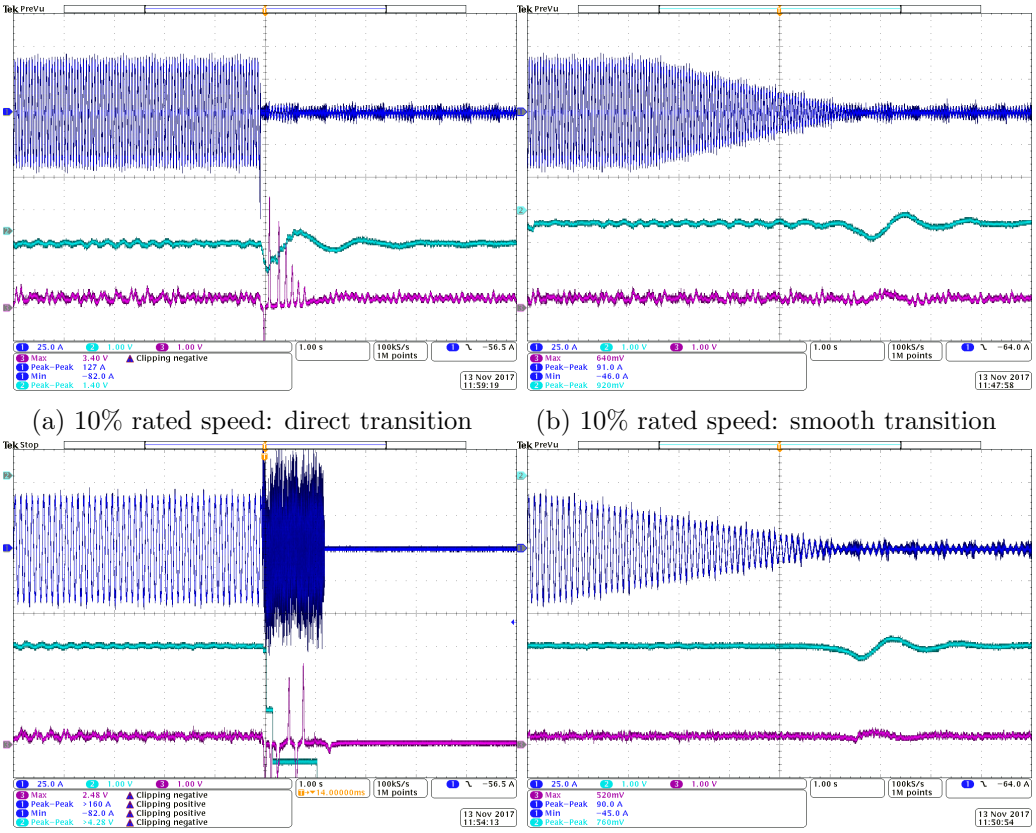

(a) 10% rated speed: direct transition (b) 10% rated speed: smooth transition

(c) 5% rated speed: direct transition (d) 5% rated speed: smooth transition

Figure 4.22: Smooth transition test on lower speed: 50kW
(Blue curve: stator current in 25 A/div. Green: rotor speed in 10 rpm/div.
Purple: torque sensor in 10 Nm/div. Time: 1s/div)

4.7 Summary

In this chapter, the issue of PMSM sensorless control is discussed.

To begin with, the background knowledge on PMSM sensorless control in marine applications are investigated. Thrusters made by PMSM are benefited from its high efficiency and compact design. On the other hand, the speed sensor is not available in many marine applications. The design of tunnel thrusters is a perfect example.

The sensorless control approaches can be categorized as the model-based and the non-model based. The performance of the model-based methods are not guaranteed in low-speed conditions. The non-model based methods, on the other hand, require high-frequency (HF) signal injection, they may introduce torque ripple to the system. A possible solution is to apply a model-based method with an open loop start.

Next, the PMSM open loop starting method ("I-f" method) and a model-based rotor position estimation approach (the back EMF method) are introduced. For the "I-f" method, its principle is provided, and the hardware test results are shown. For the back EMF method, the equations are shown. Additionally, some discussions are made on the time delay that caused by the low pass filter. The robustness tests on PMSM parameter variations are given.

The transition issue between the open loop start and the closed loop FOC is considered. A novel smooth transition method is proposed based on theoretical analyses. It is shown that the sudden change in the misalignment angle is the reason for the transient current overshoot. The proposed method decreases the q-axis current based on a closed-loop control with the error angle as its feedback. Simulation is carried out with Simulink.

Lastly, experiment results on a 3 KW and a 50 kW PMSM are shown. The hardware results are compared with simulation results. It is proved that the proposed smooth transition method improves the transient performance on the current, torque, and reduces the noise. Moreover, for the 50 kW PMSM, the direct method stop working under extra low transition speed. This issue is fixed by introducing the proposed smooth transition method.

In the next chapter, the discussion about parameter identification is made on the IM in marine applications. In that case, the $d-q$ axis misalignment is most likely caused by parameter variations, and it is possible at steady state operations. A proper parameter identification for IM is critical to improve its overall efficiency.

Chapter 5

Induction Machine Parameter Identification in Marine Applications

In this chapter, the parameter variation and its identification are discussed in the context of the induction machine (IM). The parameter variation and its identification is a large topic. This chapter will be focused on the parameters that have a significant effect in marine applications.

Rotor resistance R_r is the most important parameter since it is sensitive to temperature and also has a significant influence on efficiency. As Introduced in Chapter 2, the IM field-oriented control (FOC) requires the slip speed information. The slip speed is critical to the current loop $d-q$ axis decoupling. Error in the slip speed calculation will lead to a mismatched between the actual rotor flux and the controller rotor flux. In this chapter, the causes and consequences of the machine parameter variation are discussed. A method is proposed to find the rotor flux misalignment angle. The method is based on an analysis on the d-q axis current.

5.1 Parameter Identification in Marine Applications

For the electric propulsion module on an MES, the parameter identification for electric machines is significant. The reasons are listed as follows.

- **Extreme working conditions:** The temperature is one of the key factors that would impact the machine parameters. The electric ship sails to various

Figure 5.1: Russian nuclear icebreaker "Yamal" [154]

parts of the ocean, the large variation in temperature brings a challenge to the machine controller design. Take the icebreakers (Figure 5.1) as an example, they are required to work under the air temperature of $-35°C \rightarrow 30°C$ or the sea temperature of $-1°C \rightarrow 32°C$ [153].

- **Difficulty in maintenance:** In many electric machine applications, their robustness against parameter variation is gained through a routine of tuning and maintenance. It is easier to run the parameter identification and tuning offline than online. However, in marine applications, each operative term is as long as weeks or even mounts. On-line parameter identification is more applicable.

- **Highly integrated propulsion systems:** In the highly integrated podded structure thrusters or the tunnel thrusters. Many traditional parameter identification methods are not suitable where current injection or rotate the machine with a prime mover are required.

5.2 Induction Machine Parameter Variation

In this section, a literature review about the IM parameter variation is carried out. The rotor resistance R_r and inductance L in the IM are discussed in particular.

Their values changes with working conditions and environments, for example, temperatures, frequency and magnetic saturation levels.

5.2.1 Rotor Resistance

Rotor resistance R_r have a significant influence on the FOC. Its identification has been linked to the sensorless control algorithm in many works [155–157]. Many approaches have been proposed to find its actual value [158].

There are many off-line identification methods proposed for R_r. The method in [159] measures R_r with the machine disassembled. In [160], an electrical excitation on the stator is used to find R_r. A trial-and-error method is introduced in [161].

The "self-commissioning" is another kind of offline identification. In general industrial applications, the PWM inverter that carries the control algorithm is from one manufacturer while the target machine is from another. In that case, once the inverter and the machine are installed on site, the inverter controller needs to run a program to identify the machine parameter automatically [162,163]. This test process is referred to as "self-commissioning".

More works are focused on the online identification methods. The dynamic slip estimator is proposed in [164, 165]. In [166], a recursive method is developed to find the machine speed and the rotor time constant. It is estimated in [167] that the error of the other parameters should be kept below 10% to guarantee the accurate tracking of R_r according to the temperature change.

The extended kalman filter (EKF) based approaches are introduced in [168] and [169]. The testing signal is not required in the EKF. Instead, the harmonics of the inverter serves as the excitation. The rotor time constant is treated as the "extended" state variable in addition to the stator and rotor currents, the estimated results are applied to the FOC controller auto-tuning. The main limitation of EKF lies in its strong requirement on the matrix calculation [170]. The matrix becomes very complicated if there are multiple parameters to be identified.

Another important group of methods is based on the MRAS. In MRAS, a system variable need to be defined. There must be two approaches to calculate this pre-defined variable, with one approach contains the parameter to be identified. By comparing of the computation results from two approaches, the parameter's estimated value is tuned until it reaches the final result. In [171–173] the chosen system variable is the reactive power while in [174] and [175] it is the air gap power. The drawback for MRAS is that the identification is model based so that

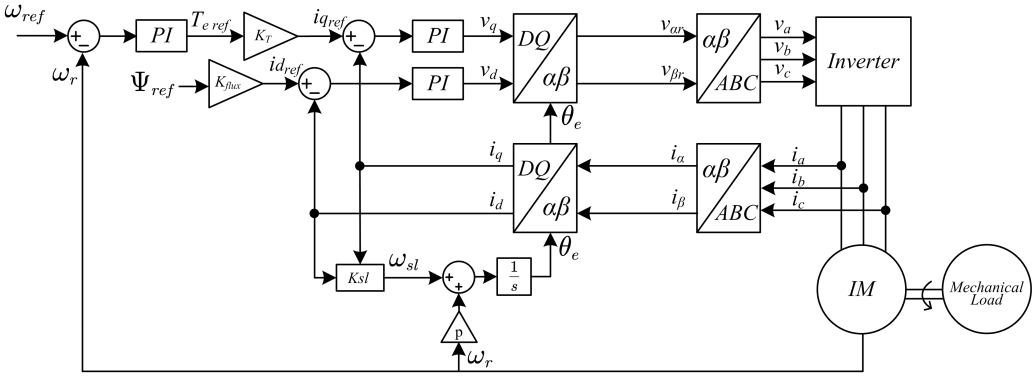

Figure 5.2: Indirect FOC for IM

it requires the other parameters to be accurate [176, 177].

5.2.2 Inductance

The inductance is another important parameter. In [178], the mutual inductance is corrected with the information of third harmonic voltage in the stator winding. Due to the saturation effect, the air gap flux is found with the third harmonic component. In a continuous work [179], the rotor flux linkage $\hat{\lambda_r}$ is identified under the same method. By comparing this $\hat{\lambda_r}$ with the λ_r that calculated by the voltage equations, the speed and mutual inductance are estimated simultaneously.

Although the rotor and stator leakage inductance L_{ls} and L_{lr} are considered less important in the rotor flux orented controllers, they are consequential in the air-gapflux-oriented control [180]. A method to identify L_{ls} and L_{lr} through the inverse stator transient inductance a (Equation (5.1)) is introduced in [181].

$$a = \frac{1}{\sigma L_s} \tag{5.1}$$

5.2.3 The Effect of Slip Speed Error

In the IM case, the FOC is introduced as an efficient and high-performance control method. In most industrial applications, the indirect FOC (IFOC) is chosen since it has less demand on the accuracy of the voltage and current measurement. The system configuration for the IFOC is shown in Figure 5.2.

As shown in Figure 5.2, the decoupling of the stator three-phase current depends on the slip speed (ω_{sl}), which is the speed difference between the electric

and physical speed. ω_{sl} is calculated with Equation (5.2).

$$\omega_{sl} = \frac{L_m}{\tau_r} \cdot \frac{i_{sq}}{\lambda_{dr}} \tag{5.2}$$

In Equation (5.2), the calculation of slip speed ω_{sl} depends on the motor parameters like the rotor time constant τ_r, the magnetizing inductance L_m and the rotor flux linkage λ_{dr}. Among which, the rotor time constant τ_r (calculated with Equation (5.3)) suffers more influence due to parameter variations.

$$\tau_r = \frac{L_r}{R_r} \tag{5.3}$$

where R_r normally draws more attention than L_r. A sensitivity analysis about R_r and L_r is made in [182]. In steady state, the rotor flux linkage λ_r is obtained with

$$\lambda_r = L_M \cdot i_{ds} \tag{5.4}$$

In contrast to the mutual inductance, the leakage inductance is negligible, L_r is considered equal to L_M. In that case, Equation (5.2) is transformed into

$$\omega_{sl} = \frac{1}{\tau_r} \cdot \frac{i_{qs}}{i_{ds}} \tag{5.5}$$

In conclusion, the rotor time constant τ_r impacts ω_{sl} and influences the torque and flux through the $d-q$ axis current. L_M directly influences the flux, which will also impact the torque.

Their relationship are revealed clearly with numbers. In [183], 100% change is applied to both rotor resistance and mutual inductance. Result in Table 5.1 shows system is more sensitive about error in R_r.

Table 5.1: Sensitive analysis on R_r and L_M

	R_r +100%	L_M +100%
Torque change	1.2%	0.43%
Flux change	66%	8.3 %

In another perspective, R_r it is significantly influenced by the environment. The variation of R_r can up to 100% due to a changing temperature [184]. In parameter identification of IMs, some literature would choose a full order observer of all major parameters like L_m, L_r, R_r, and flux [185]. However, as all the pa-

rameters are coupled in the observer, the error is larger when multiple parameters are estimated together. On the other hand, the estimation is more accurate when a single parameter is estimated, while the rests are considered as constant [184]. In this approach, normally the rotor resistance R_r is chosen as the one for estimation,since the adaptive control based on a changing R_r is more likely to show more noticeable results.

5.2.4 Sensorless Control

The sensorless control and parameter identification are frequently discussed jointly. Their correspondence is twofold.

- In a model-based sensorless control, the accuracy is dependent on the rotor time constant T_r.
- As discussed above, the parameter error affects the calculation of the slip speed, which will lead to an error in the flux orientation. In sensorless control, the rotor speed is also estimated. In that case, the rotor speed estimation is equally important as the parameter identification. That is the reason of the researchers in [186, 187] are searching for techniques that can identify both at the same time.

5.3 Analysis on the IM dq Misalignment

In a controlled IM, the torque balance is always achieved even if the misalignment exists.

In Figure 5.3, the stator currents I_s is decoupled by both the controller and rotor reference frame.

WIth the slip speed that is calculated by the machine parameters including R_r (Equation (5.2)). It is impossible to eliminate the error angle θ_{err} completely. i_d / i_q, i'_d / i'_q are different decouple values of I_s, their relationship is shown in Equation (5.6).

$$\begin{bmatrix} i'_{sq} \\ i'_{sd} \end{bmatrix} = \begin{bmatrix} \cos\theta & \sin\theta \\ -\sin\theta & \cos\theta \end{bmatrix} \begin{bmatrix} i_{sq} \\ i_{sd} \end{bmatrix} \tag{5.6}$$

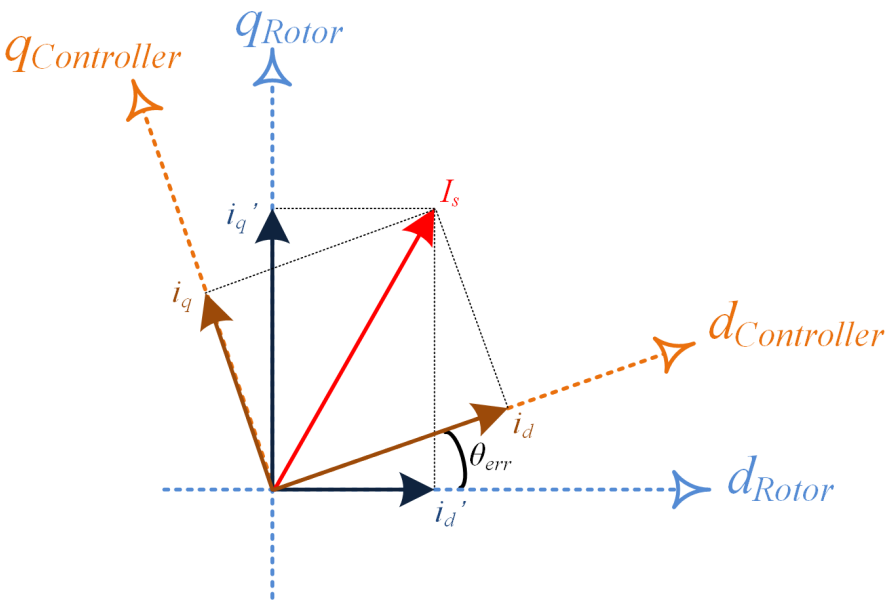

Figure 5.3: Induction motor dq angle misalignment

The θ_{err} is decided by the torque balance. In other words, when dq axis are misaligned, the motor is still operating with the torque balanced. Thus there is only one possible angle error.

The torque balance means that the electric torque generated is equal to the required load torque. The electrical torque T_e is calculated with equation (5.7).

$$T_e = \frac{3P}{2}\frac{L_m^2}{L_r} i'_q i'_d \tag{5.7}$$

In equation (5.7), the i'_q and i'_d are the actual dq current in the motor (shown in Figure 5.3). When motor parameters L_m, L_r and the torque condition T_e are considered constant, the product of i'_q and i'_d is constant. In equation (5.8), this production is defined as K. Note that only the product of i'_q and i'_d is fixed, the specific combination of i'_q and i'_d is also influenced by the FOC control parameters.

$$K = i'_q i'_d = \frac{2L_r T_e}{3PL_m^2} \tag{5.8}$$

With the value of K calculated, the actual value of i'_q and i'_d are hidden since the accurate rotor flux direction is unknown. Replace them with i_q and i_d using Equation (5.6), Equation (5.9) can be found. i_q and i_d are easily read from the

controller. As the response time of the current loop is much faster than the torque balancing process, thus it is satisfactory to apply the reference values of i_q^* and i_d^* as i_q and i_d.

$$K = i'_q i'_d = \frac{\sin(2\theta)}{2}\left(i_q^2 - i_d^2\right) + \cos(2\theta)\, i_q i_d \tag{5.9}$$

In Equation (5.9), the only unknown factor is the error angle θ. It is found by solving the equation.

In the next sections, simulation and hardware tests are performed to verify the proposed method.

5.4 Simulation Results

In this section, a simulation is made with Simulink to verify the propoesd method. There are normal condition and error condition where the rotor resistance R_r has changed. The parameters in the IM model are shown in Table 5.2.

The stator currents, rotor speed and torque are shown in Figure 5.4. The working condition is set to a relatively higher speed and torque to give a better demonstration of the influence of R_r change. The motor acceleration starts at $t = 0s$. Reference speed is set to 1200 rpm. At $t = 3s$, a 30 Nm load torque is added. At $t = 5s$, the rotor resistance applied to the controller changes from 100% to 50% of the rated value within 1 second. A small torque oscillation can be observed after the change.

With the given working condition, the dq axis current change is shown in Figure 5.5. Stator current i_q changes from $i_q = 20.77A$ to $i_q = 14.47A$ when R_r changes at $t = 5s$. Note that after R_r changes, the controller reference frame is no longer aligned with the actual rotor flux direction. To prove that, the slip theta calculated with the d-FOC and i-FOC are compared in Figure 5.6.

The direct FOC (DFOC) and indirect FOC (IFOC) represents two approaches to obtain the rotor flux direction when applying rotor flux oriented field-oriented control.

In DFOC, the rotor flux $\psi_{r\alpha}$ and $\psi_{r\beta}$ are calculated through the stator current and voltage. The rotor flux orientation is calculated as Equation (5.10). DFOC is very sensitive to the error in the current or voltage measurements. In addition, as the rotor flux angle θ_e is found with a tan^{-1} calculation, it make this method unstable in experiment conditions. However, in simulation, such disturbance does

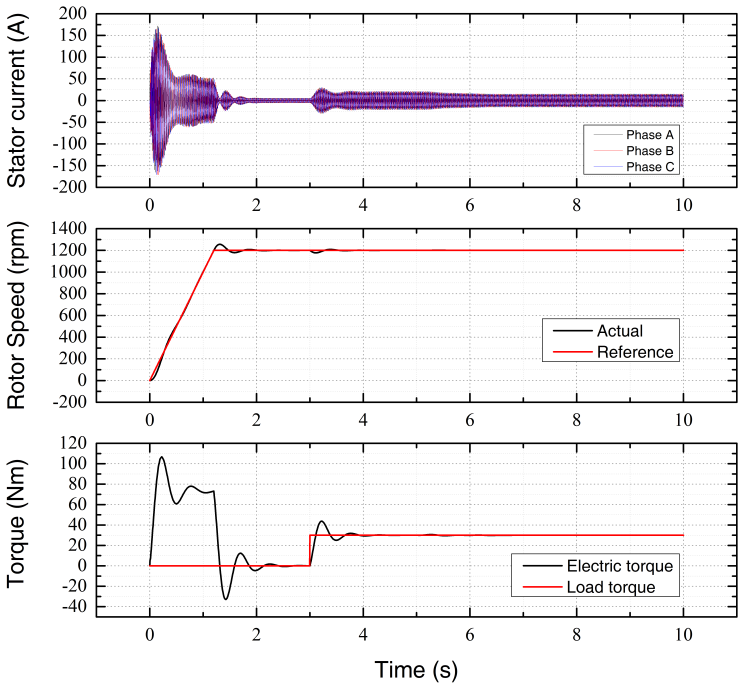

Figure 5.4: IM R_r misalignment simulation: working condition

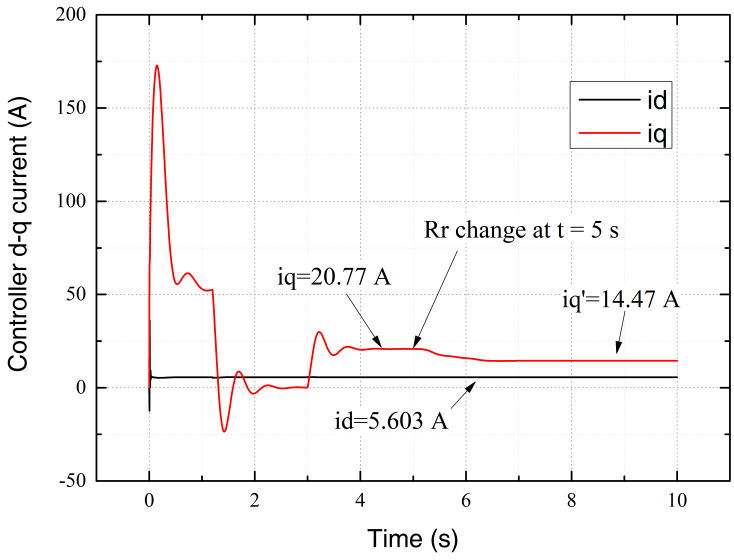

Figure 5.5: "d-q" current from controller reference frame

Table 5.2: Specifications of 15 kW induction machine

Specifications	**Value**
Rated power	15 kW
Stator voltage	415 V
Stator current	28 A
Rotor resistance R_r	0.2648 Ω
Stator resistance R_s	0.2788 Ω
Stator leakage inductance L_{ls}	2.814 mH
Rotor leakage inductanceL_{lr}	3.719 mH
Mutual inductanceL_m	89.240 mH
Moment of inertia J	0.7 kg.m^2
Friction factor B	0.02 N.m.s
Pairs of poles	2

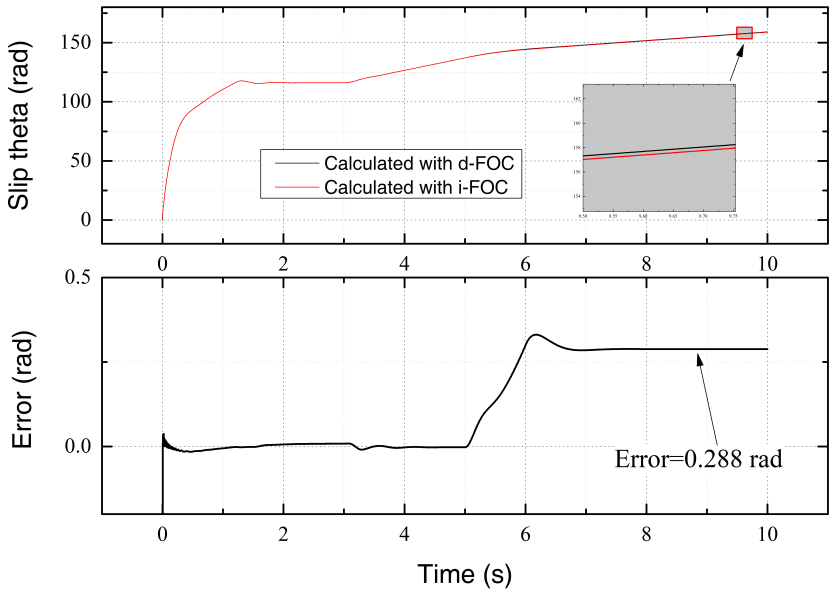

Figure 5.6: Error in slip rotor position θ_{err}

not exist. DFOC is suitable to find the actual rotor flux angle as a comparison. On the other hand, iFOC is the common approach to find the rotor flux angle in experiments. The angle is obtained by adding the rotor physical angle to the slip speed angle (Equation (5.11)). In IFOC, ω_{slip} is calculated with machine parameters. when there is a parameter variations, the calculation result will be mistaken, as shown in Figure 5.6. It is observed θ_{err} continuously increase since rotor resistance change in the controller at $t = 5\ s$, after about 2 seconds, a new balance is reached at $\theta_{err} = 0.288 rad$.

$$\theta_e = \tan^{-1}(\frac{\psi_{r\beta}}{\psi_{r\alpha}}) \tag{5.10}$$

$$\omega_e = \omega_r * p + \omega_{slip} \tag{5.11}$$

$$\theta_e = \frac{1}{s}\omega_e \tag{5.12}$$

The misalignment currents are read in Figure 5.5, $i_q = 14.47\ A$, and $i_d = 5.603\ A$. Applying then to the proposed method in Equation (5.8) and Equation (5.9),

$$K = 116.76$$

.

The solution of Equation (5.9) is shown in Figure 5.7. The calculation result $\theta_{err} = 0.289\ rad$ matches the actual angle error from the model reading, which is $\theta_{err} = 0.288\ rad$. This simulation result proves that the proposed method is practical in finding the misalignment angle.

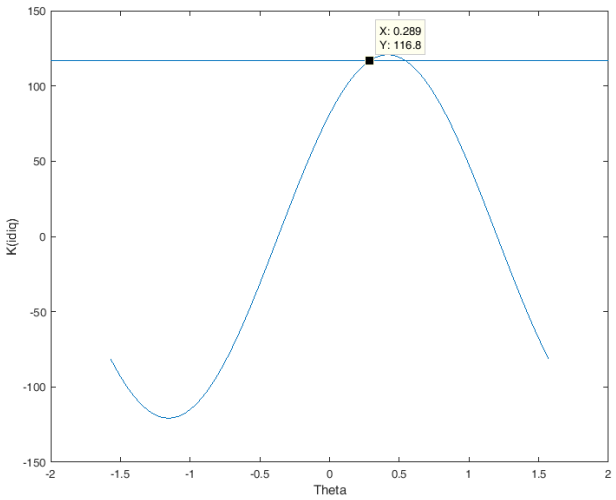

Figure 5.7: Simulation result: solution to Equation (5.9)
Intersect point: X(θ_{err})=0.289 rad, Y(K)=116.8

5.5 Hardware Test

The algorithm is tested on the 15 kW IM. The machine parameters are shown in Table 5.2. The hardware setup is comprehensively introduced in Section 3.6. It will not be repeated for conciseness.

5.5.1 Test Results Under the Default T_r

The test condition is set to 1200 rpm, 30 Nm. The rotor time constant in the controller is intentionally set to twice of the manufacturer provided value in order to create a misalignment angle. K is calculated assuming that T_e is 31 Nm, and i_d, i_q are measured values from the controller. The test results are logged as,

$$\begin{aligned} K =& \frac{2L_r T_e}{3PL_m^2} = 120.62(A^2) \\ i_d =& 5.67(A) \\ i_q =& 16.81(A) \end{aligned} \tag{5.13}$$

Figure 5.8 shows when the torque is balanced, the electrical angel error θ under different load conditions(represent as the different values of K). Solving Equation (5.9) is in the same way of finding the cross point in this figure. The horizontal

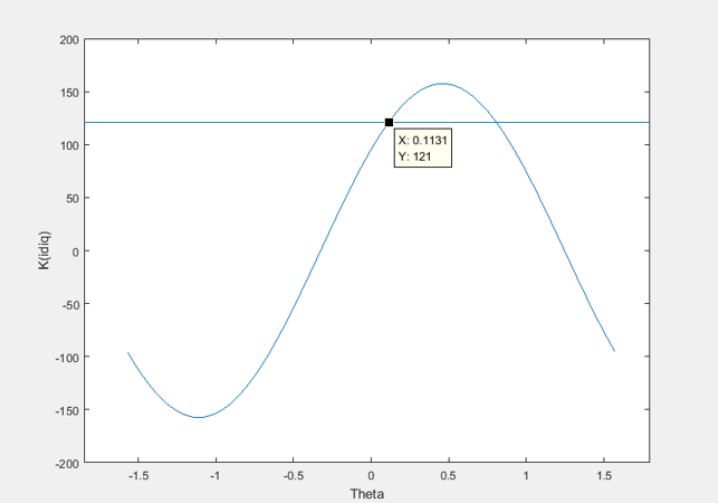

Figure 5.8: Hardware result: solution to Equation (5.9)
Intersect point: X(θ_{err})=0.1131 rad, Y(K)=121

line shows $K = 120.6244053(A^2)$, the solution is the intersection point of the two curves. For an equation with trigonometric functions, there are multiple solutions. However, as the error of the slip speed, θ should be close to zero, the solution is $\theta = 0.1131\ rad$, which is about 6.48° misalignment between two reference frames.

5.5.2 Test Results Under Various T_r

In another test under the same working condition, the rotor time constant in the controller is intentionally changed to simulate the working condition where the real rotor time constant is unknown. The torque balance is constant, i_d, i_q are logged as follows. Result calculated shown in Table 5.3, where the T_r column presents how many times the rotor time constant is set as a ratio in contrast to the value provided by the motor manufacturer. The calculated error angle is calculated and transformed into an electrical degree. T_r^* is the time constant that provided by the manufacturer.

Note that in this test, $T_r = 1 \times T_r^*$ does not lead to the smallest error angle. That indicates that the value provided by the manufacturer is not accurate, or the parameter has changed through time. Since the error angel is the smallest when $T_r = 1.2 \times T_r^*$, it is possible that the real value is close to $1.2 \times T_r^*$.

$$\omega_{sl} = \frac{L_m}{\tau_r} \frac{i_{sq}}{\lambda_{dr}} \tag{5.14}$$

Table 5.3: Estimation error angel with the proposed method

Tr/T_r^*	id	iq	Error angle (degree)
0.5	5.987	36.99	-4.320
0.8	5.977	24.92	-2.880
1	5.551	19.92	1.439
1.2	5.971	19.32	0.900
1.5	5.921	14.6	15.297

On the other hand, one should note that the slip speed calculation (Equation (5.14)) is also influenced by other parameters. When it is assumed that $T_r = 1.2 \times T_r^*$ is actual value. It is possible that it is the other parameters that changed while the new $T_r = 1.2 \times T_r^*$ compensates the change. In industrial applications, the conditions are more complicated with more variables to be considered. It would be challenging to identify them all simultaneously. In that case, applying T_r that identified with the proposed method would be a reliable approach to improve the system efficiency.

Max torque per ampere (MTPA) is another important concept in industrial applications. The "Ampere" in this context may calculated with

$$\left|\overrightarrow{i}\right| = \sqrt{i_d^2 + i_q^2}$$

Another interesting finding in this chapter is that low angel error does not lead to MTPA operation. In other words, the efficiency is actually higher in some error conditions.

Table 5.4: Stator currents vector magnitude

Tr/T_r^*	id	iq	$\left\|\overrightarrow{i}\right\|$
1	5.551	19.92	20.69
1.2	5.971	19.32	20.22
1.5	5.921	14.6	15.77
0.8	5.977	24.92	25.63
0.5	5.987	36.99	37.47

Compare experiments working in the same condition in Table 5.4. Test $T_r = 1.5$ has the minimal total current. However, the angle error for the same condition is very large due to analysis. This contradiction can be explained with Equation (5.7). As electric torque is the production of i_d and i_q, from a mathematical calculation, Max torque per ampere (MTPA) operation is achieved when $i_d = i_q$, in that case, large angel error in $T_r = 1.5$ make the total current smaller.

In real applications, the MTPA requires more quantitative analysis. As in marine, a large torque is required by the propeller, which indicate that the i_q is large, on the other hand, the rotor flux linkage that generated by i_d is bounded by magnetic material saturation. That means in various working conditions, the rule to determine MTPA strategy also various.

5.6 Summary

In this chapter, a discussion is made on the parameter identification of marine IM applications. The slip speed calculation is very important and it demands an accurate value of the electric parameters. R_r is the most important parameter in marine applications considering its sensitivity to environmental temperature and its influence to machine efficiency. The R_r identification methods are briefly reviewed.

In the next section, the DQ misalignment issue caused by the error in R_r is analyzed. It is shown in that condition, the torque balance between electric torque generated and required load torque are kept. In that case, with an active closed loop controller, a new i_q and i_d will be reached. A method is proposed to find the misalignment angle θ_{err} with the d-q current information.

The simulation is carried out to verify the proposed method. It is shown that the estimated θ_{err} matches the actual value found by the DFOC method. Next, in the hardware test, the rotor resistance in the controller is intentionally tuned to a error value, and the θ_{err} is calculated under multiple conditions. It is shown that θ_{err} is minimal when the T_r is set to 1.2 times of the original value. That implies a potential error in the parameter provided by machine manufacture, or the parameter has changed through time.

In the next chapter, the parameter identification issue will be extended to the PMSM. In the PMSM, there is no influence from the slip speed. The importance of each parameter is reconsidered in the standard of marine applications. The flux estimation through Luenberger observer is introduced. And the recursive

least square (RLS) approach is implemented to identify four critical parameters simultaneously.

Chapter 6

PMSM Parameter Identification in Marine Applications

The high-performance control of PMSM requires the accurate knowledge of machine parameters. In industrial applications, although the motor parameters can be obtained through multiple approaches, it is difficult to find the accurate parameters in various operating conditions. The resistance changes with temperature, inductance is influenced by the saturation level of the current. A small parameter variation will affect the controller performance, while a large one will make the whole system unstable. In the sensorless control, a parameter error will lead to an error in position estimation.

In this chapter, the discussion will be focused on the marine applications, the key parameters in marine PMSM are discussed. The inductance L_d and L_q, stator resistance R_s, and rotor flux ψ are the most important parameters to be identified. To begin with, a rotor flux ψ estimation method through a Luenberger observer is proposed. It is verified with hardware test. Next, a full order parameter (d,q axis inductance, resistance, and flux) identification by the recursive least square (RLS) method is proposed. The d-axis perturbation is introduced to overcome the deficiency of data. The selection of the forgotten factor is discussed. The results show that the L_q, L_d and flux can be estimated with some error. However, the resistance estimation cannot reach a satisfying outcome. The potential causes are discussed.

6.1 Background

In this section, the issue of PMSM parameter variation is discussed. Next, the importance of each parameter in marine applications are introduced. In the end, some PMSM parameter identification algorithms are reviewed.

6.1.1 PMSM Parameter Variations

The mathematical model for the PMSM is shown in Equation (6.1) [53].

$$\begin{cases} \frac{d}{dt}i_d = \frac{1}{L_d}v_d - \frac{R}{L_d}i_d + \frac{L_q}{L_d}p\omega_m i_q \\ \frac{d}{dt}i_q = \frac{1}{L_q}v_q - \frac{R}{L_q}i_q - \frac{L_d}{L_q}p\omega_m i_d - \frac{\lambda p\omega_m}{L_q} \\ T_e = 1.5p[\lambda i_q + (L_d - L_q)i_d i_q] \end{cases} \tag{6.1}$$

where L_d and L_q refer to the d and q axis inductions, respectively. R refers to stator resistance. i_d and i_q are the stator currents of d and q axis. ω_m is the rotor mechanical speed in rad/s. λ is the rotor flux linkage that generated by the permanent magnet. It keeps constant in normal conditions and only affected by saturation of the magnetic material. p is the number of pole pairs.

In practice, some of the parameters that provided by the manufacturer are not accurate. In addition, their values may change slowly depending on the working condition [188]. The causes for parameter variations and their risks are summarized in Table 6.1.

Table 6.1: PMSM parameter variation and its affects [189]

Working Conditions	Parameter affected	Risk
Temperature	Resistance	Current loop fail
	Rotor flux linkage	Efficiency Permanent demagnetization
Current rating	Inductance(due to saturation)	Current loop fail
Coupling, friction	Inertia, friction factor	Speed loop fail

The parameter identification techniques are proved to be an effective approach to enhance the controller performance and reduce the risk [189].

6.1.2 PMSM Parameter Variations in Marine Applications

There is a wide implementation of PMSM on electric ships that have been introduced in the literature [190–192]. In marine applications, the PMSM parameter identification is equally essential as IM. Part of the reasons is similar with the IM that reported in Section 5.1. For the PMSM, the inductance L_d and L_q, stator resistance R_s and rotor flux ψ are chosen as they are particularly important in marine applications. The reasons are listed as follows.

Inductance L_d and L_q

Inductance L_d and L_q are important to the interior PMSM (IPMSM). It is introduced in [193] that IPMSM have many advantages over other PM Motor structures.

- Firstly, building an SPMSM requires larger airgap for mechanical safety concerns, especially in marine applications where the power ratings are usually huge. On the other hand, the air gap in an IPMSM can be made smaller.
- Secondly, the PMSM design must be robust against the demagnetization in ships. For the SPMSM, it can only be achieved by using thicker magnets, as for the IPMSM, an additional path for the armature winding can be applied for protection.
- Lastly, magnets in an IPMSM are not placed on the surface. It is safer against physical damages. Additionally, such structure makes it less vulnerable to the corrosion on the ocean [194].

Rotor Flux ψ and Stator Resistance R_s

The rotor flux ψ has always been an important parameter to all PMSMs. In electric ships, it is essential for the torque controller design and the demagnetization protect.

The stator resistance R_s is selected due to its sensitivity against temperature.

6.1.3 PMSM Parameter Identification Algorithms

The parameter identification of PMSM is presented in many litertatures. The methods can be categorized as the off-line and on-line methods. The off-line methods measure the machine parameters during standstill. Results are easier to find in this way. The off-line signal injection methods can be designed more aggressive since the motor operation is not taken into consideration. On-line parameter identification is more difficult since most of the parameters are coupled when the motor is operating, when a failed estimation is applied to estimate the other parameters, the results would be influenced. However, since motor parameters change in various working conditions, on-line estimation results are more valuable for the motor drives.

An inductance estimation method based on a locked rotor approach is proposed in [195]. The saturation and the cross magnetization effects in an interior PMSM is considered as the primary cause for the inductance variation. Signals are injected to both d and q axis to find the parameters for an ideal two-axis machine model. A similar method is proposed in [196] regarding on the synchronous reluctance machine. Parameters are found by analyses on two axis signals. In addition, a simpler mathmatical model for the synchronous reluctance machine is proposed. Finite element analysis (FEA) is also an excellent off-line approach to find the parameters [197]. It is also possible to find a table of changing parameters in various working conditions (voltage, current, etc.) through the FEA. By lookup table, the controller can work as the parameters are identified on-line [198]. In [199], the signal injection method is introduced to a PMSM at standstill.

Most on-line parameter identification approaches are focused on the resistance, inductance and rotor flux linkage. Among which the rotor resistance has drawn most attention since it greatly influences the performance of the sensorless controller [200, 201]. It is proved that the adaptive resistance is also essential to the flux estimation [202]. In [203], the rotor position error is estimated and used as a feedback signal to estimate the resistance and flux. In extra low-speed working conditions, the estimated resistances are applied to achieve a more accurate speed estimation [204]. There are also on-line parameter identification approaches that designed for the inductance alone. It is proved that a more accurate inductance can improve the current controller performance [205].

Several attempts have been made to identify all the parameters simultaneously with a full order observer. The full order observer algorithm requires exceeding

calculation. At the same time, the convergence of the algorithm is not promising. The Full order observer for PMSM cannot work without current perturbations, since it is rank-deficient for the steady state machine model to estimate more than two parameters [133, 206, 207]. Mostly, perturbations are introduced on the d-axis current, since in PMSM controller the rotor flux is decided by the built-in magnet, the d-axis current is normally set to zero.

As in observer algorithms, modern control theories are introduced, like the RLS, the extended kalman filter (EKF), and the MRAS. The RLS algorithms are applied in multiple papers. In [208], a full order observer is designed. The estimated parameters are the d and q axis inductance, flux linkage and rotor resistance. A double-observer loop structure is introduced to solve the convergence issue. A fast loop is made to estimate the inductance, while the slow loop is for the flux and resistance since the temperature change ratio is much slower than the electromagnetic changes. In the RLS observer, assuming one of the parameters as constant can significantly reduce the calculation complexity and increase estimation accuracy. In [209], the rotor flux is considered as constant, other parameters are observed in a IPMSM. On the contrary, the rotor flux is the focus in [128].

There are other mathematical methods applied to the identification except for the RLS. In [210], EKF is chosen due to its high tolerance against measurement errors. The winding resistance and the flux linkage are identified independently. Simulation results are shown. A MRAS-based estimation method is introduced in [201]. The stater resistance is estimated on-line to ensure low-speed operation performance. Another online method is proposed in [211], where an auxiliary measurement of the power and torque information is applied to achieve a better estimation performance.

Beside the electric parameters, there is literature focus on the mechanical parameter identification. The methods normally apply to both interior PM and surface-mount PM [212]. A mass identification method is proposed in [213], and an adaptive controller is applied to the linear PMSM servo drive regarding on the changing plant parameters. In [214], an artificial-neural-network (ANN) based method is applied to improve the speed loop performance adaptively. The ANN is updated by an online training model in a wide range of operating conditions.

6.2 Rotor Flux Estimation with Luenberger Observer

For all the PMSMs, the rotor flux is generated by the permanent magnet that placed in the rotor. The value of the rotor flux is essential for the calculation of the electric torque output. If the stator current is decoupled into a $d-q$ reference frame, the electric torque for the PMSM is shown as Equation (6.2) [53].

$$T_e = \frac{3}{2} n_p \frac{L_m}{L_r} i_{qs} \Phi \tag{6.2}$$

In Equation (6.2), Φ is the rotor flux. It is depended on the physical property of the permanent magnet. With its help, the assignment of d-axis current i_d is not necessary anymore, i.e. $i_{dref} = 0$. That will lead to high power and mass density for the PMSM. For some other occasions, a positive value of i_d is introduced to gain maximum torque per ampere operation, or a negative i_d to decreasing the rotor flux by stator to counter large electromotive force (EMF) in high-speed [215]. The proper knowledge for rotor flux induced by the magnet is essential for advanced control of PMSM.

The off-line measurement method for rotor flux is introduced in Section 2.3.3. However, the rotor flux may not keep constant in various working conditions. Additionally, some requirements for off-line measurement method cannot be fulfilled once the motor is installed. For example, the rotor needs to be driven by external torque and reaches a specific speed, and the back-emf curve needs to be captured by an oscilloscope. Thus, online rotor flux estimation method is necessary and practical.

In this section, the rotor flux estimation method through Luenberger observer is proposed and tested. The equations are derived, and the estimation results are compared with the off-line measurement results.

6.2.1 Mathematical Model and Configuration Diagram

The mathematical model for PMSM is shown in Equation (6.1) [53].

With Equation (6.1), define state x as Equation (6.3).

$$x = \begin{bmatrix} i_q \\ \\ \lambda \end{bmatrix} \tag{6.3}$$

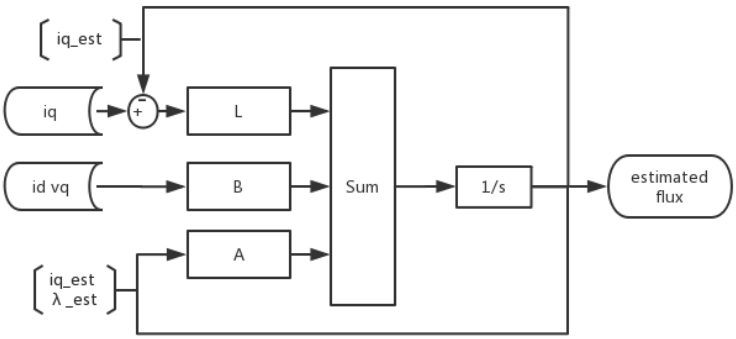

Figure 6.1: Rotor flux Luenberger observer

The state space model is rewrite as Equation (6.4).

$$\frac{d}{dt}x = \begin{bmatrix} \frac{-R_s}{L_q} & \frac{-\omega_e}{L_q} \\ 0 & 0 \end{bmatrix} x + \begin{bmatrix} \frac{1}{L_q} & \frac{-L_d\omega_e}{L_q} \\ 0 & 0 \end{bmatrix} \begin{bmatrix} V_q \\ i_d \end{bmatrix} \tag{6.4}$$

Define system parameter matrix A, B and system input u.

$$A = \begin{bmatrix} \frac{-R_s}{L_q} & \frac{-\omega_e}{L_q} \\ 0 & 0 \end{bmatrix},\ B = \begin{bmatrix} \frac{1}{L_q} & \frac{-L_d\omega_e}{L_q} \\ 0 & 0 \end{bmatrix},\ \boldsymbol{u} = \begin{bmatrix} V_q \\ i_d \end{bmatrix} \tag{6.5}$$

A Luenberger Observer can be written as Equation (6.6).

$$\dot{z}(t) = Az(t) + Bu(t) + L(y(t) - Cz(t)) \tag{6.6}$$

In rotor flux estimation perspective, $y(t)$ and $Cz(t)$ are the actual and estimation value of i_q. The diagram for the same configuration is shown in Figure 6.1. Matrix L is designed to control the dynamic response of the observer.

6.2.2 Hardware Test Results

The hardware test is carried out on the 3 kW PMSM test rig since it is an IPMSM machine. Its introduction is in Section 4.6.1. The hardware setup is remained the same with Chapter 4 and it will not be repeated.

The working condition is shown in Figure 6.2. It is set to steady state operation

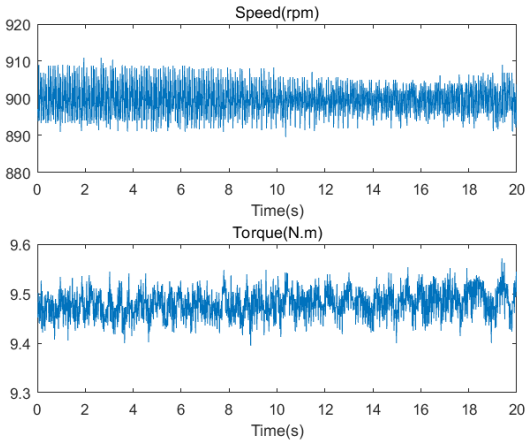

Figure 6.2: Working condition for Luenberger observer test

of 900 rpm, with a load of 9.5 Nm added to the machine. The load is added to increase the stator current from the inverter, since the inverter current sensor's resolution is limited when in low current.

The rotor flux estimation result is shown in Figure 6.3. This estimation successfully converged to a constant value, which is around $0.21Wb$. The rotor flux calculated with the off-line back EMF test is $0.197Wb$ (Section 2.3.3), it is shown in a red line in Figure 6.3. The error between them is 6.5%. There are two factors that may lead to the difference.

- As there is no external torque supply on the other end of the test machine, the back-emf test requires to run the machine to a certain speed with the normal inverter, than break the circuit and connect the stator ends to the oscilloscope. The back EMF testing result may not be accurate.
- The Luenberger observer is highly parameter dependent. Additionally, it requires the accuracy of the current measurement, which is plausible in this test.

The robustness of the observer is tested with three major parameters L_d, L_q and R_s changed. The results are shown in Figure 6.4 to Figure 6.6. For each one, the parameter variation does not happen in the machine, which is very hard to realize in hardware tests. Equivalently, the parameters applied to the observer are intentionally increased 50% higher than the actual value.

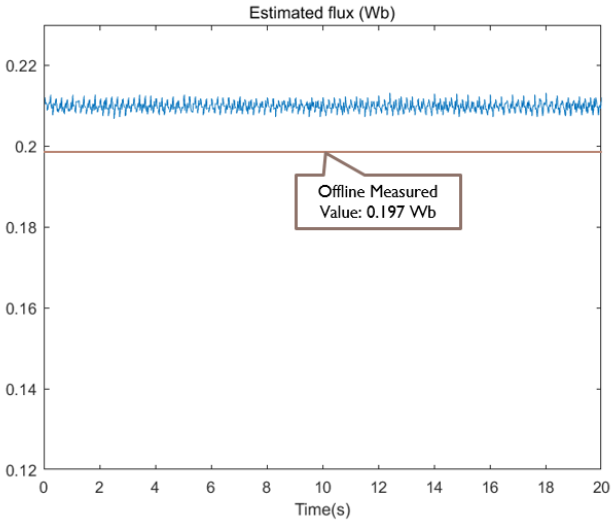

Figure 6.3: Luenberger observer test result

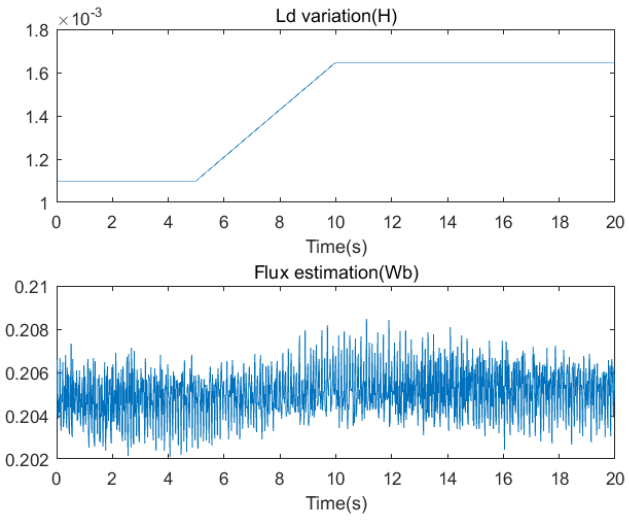

Figure 6.4: Luenberger observer robustness test: L_d

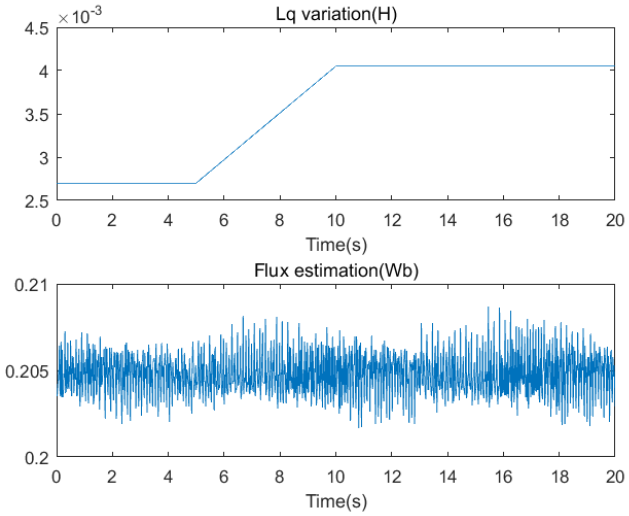

Figure 6.5: Luenberger observer robustness test: L_q

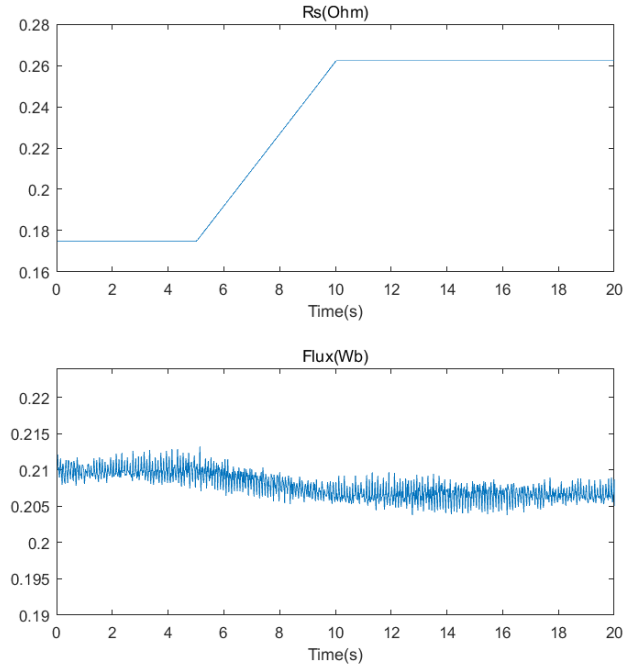

Figure 6.6: Luenberger observer robustness test: R_s

The test results show Luenberger observer has high overall robustness against inductance variation on both d and q axis. When stator resistance changes, the estimation result drops from 0.21 Wb to 0.207 Wb. Among the three parameters, R_s changes with temperature most. Temperature is most likely to change in various working conditions. The robustness test results explain the reason for the error in Figure 6.3.

6.3 Online Parameters Identification with RLS

Estimation of multiple parameters at the same time is a more challenging task. In a full order observer, all the parameters are estimated as a vector from matrix calculation. In that case, error in one parameter may influence the other. At the same time, more system working conditions are required for the on-line parameter identification Take the RLS method as an example, a perturbation is necessary. It should provide the most data to the estimation algorithm while casting the least influence to the normal system operation. In spite of this, the estimation of multiple parameters simultaneously still have more constraints.

In this section, the RLS method is applied to estimate the PMSM parameters. The purpose is to estimate d and q axis inductance, rotor resistance and rotor flux at the same time. The introduction of the RLS algorithm is given, the equations are derived for the implementation on PMSM. Then simulation and hardware test results are shown.

6.3.1 A Brief Introduction to the RLS Algorithm

The RLS method is based on the least square (LS) algorithm. By a certain number of measurement on system input and output, the system parameter can be estimated. The least square is focused on the calculation of a certain time period. Comparatively, RLS is designed to work under online estimation tasks. For a system described in the form of Equation (6.7) [216].

$$Y = \Phi\theta \tag{6.7}$$

where Y presents the system output while Φ is the measurement vector. θ presents the parameter vector that require estimation.

$$\Phi = [\varphi_1, \varphi_2, \varphi_3, \cdots \ \varphi_k]^T \tag{6.8}$$

$$Y = [y_1, y_2, y_3, \cdots \ y_k]^T \tag{6.9}$$

The LS cost function can be defined as Equation (6.10). The aim of the algorithm is to find vector θ to gain minimal value of V.

$$V_\theta = \frac{1}{2}\sum_{k=1}^{N}(y_k - \varphi_k^T\theta)^2 \tag{6.10}$$

The solution of the equation can be given as

$$\theta_{est} = (\Phi^T \cdot \Phi)^{-1} \cdot \Phi^T \cdot Y \tag{6.11}$$

To change the LS algorithm can be considered as an RLS algorithm at a particular time point. However, for RLS the results from the previous time also need to be taken into consideration. The LS at a particular time k can be written as

$$\theta_{est(k)} = (\Phi_{(k)}^T \cdot \Phi_{(k)})^{-1} \cdot \Phi_{(k)}^T \cdot Y_{(k)} \tag{6.12}$$

Define $F_{(k)} = (\Phi_{(k)}^T \cdot \Phi_{(k)})$, as $\Phi_{(k)} = [\Phi_{(k-1)} \ \varphi_k]$, Equation (6.13) can be derived.

$$F_{(k)} = (\Phi_{(k)}^T \cdot \Phi_{(k)}) = (\Phi_{(k-1)}^T \cdot \Phi_{(k-1)}) + \varphi_{(k)}\varphi_{(k)}^T = F_{(k-1)} + \varphi_{(k)}\varphi_{(k)}^T \tag{6.13}$$

Next, the equation for $\theta_{est(k)}$ can be found in Equation (6.14).

$$\theta_{est(k)} = \ F_{(k)}^{-1}\left[F_{(k)} \ \theta_{est(k-1)} - \varphi_{(k)} \ . \ \ \varphi_{(k)}^T.\theta_{est(k-1)} + \varphi_{(k)} \ y_{(k)} \ \right] \tag{6.14}$$

Thus, the time related RLS algorithm can be written as Equation (6.15) [216].

$$\begin{cases} \theta_{est(k)} = \theta_{est(k-1)} + F_{(k)}^{-1} \cdot \varphi_{(k)}(y_{(k)} - \varphi_{(k)}^T \cdot \theta_{est(k-1)}) \\ F_{(k)} = F_{(k-1)} + \varphi_{(k)} \cdot \varphi_{(k)}^T \end{cases} \tag{6.15}$$

Introduce the forgotten factor λ to set the different weights to the present time data and the previous time data. The final equations for RLS are shown in Equation (6.16).

$$\begin{aligned} \theta_{est(k)} &= \theta_{est(k-1)} + K_{(k)} \cdot \epsilon_{(k)} \\ \epsilon_{(k)} &= y_{(k)} - \varphi_{(k)}^T \cdot \theta_{est(k-1)} \\ K_{(k)} &= P_{(k-1)} \cdot \varphi_{(k)} [\lambda \cdot I_n + \varphi_{(k)}^T \cdot P_{(k-1)} \cdot \varphi_{(k)}] \\ P_{(k)} &= [I_n - K_{(k)} \cdot \varphi_{(k)}^T] \cdot P_{(k-1)} / \lambda \end{aligned} \tag{6.16}$$

6.3.2 RLS for PMSM Parameter Identification

Applying the RLS algorithm to PMSM parameter identification, the vector and matrix are shown in Equation (6.17), where ω_e is the electrical speed of the motor. It can be calculated by multiplying the number of pole pairs and the mechanical speed ω_r. Estimated K_T is the rotor flux linkage, as λ refers to the forgotten factor in the first place.

$$Y = \begin{bmatrix} V_q \\ V_d \end{bmatrix}, \ \theta = \begin{bmatrix} L_q \\ L_d \\ r_s \\ K_T \end{bmatrix}, \ \varphi^T = \begin{bmatrix} 0 & \omega_e i_d & i_q & \omega_r \\ -\omega_e i_q & 0 & i_d & 0 \end{bmatrix} \tag{6.17}$$

RLS as a full order observer estimates all four parameters at the same time. The condition of observer convergence is strict. Adding perturbation is very important.

Take this PMSM parameter estimation as an example. There are more state variables contained than the number of equations. This data deficiency cannot be overcome by methods without introducing a new operation model. Here the d-axis current i_d is set to $3A \pm 2A$ for 0.03 second at each state.

6.3.3 Simulation Results

The simulation is carried out to verify the performance of RLS on PMSM. The simulation is realized on Simulink. Matrix calculation is performed in an S-function.

Table 6.2: Specifications of 7.7 kW PMSM

Specifications	**Value**
Rated current (A)	27.7
Rated speed (rpm)	3150
Rated torque (Nm)	31.8
Inductance L_d (mH)	1.089
Inductance L_q (mH)	2.606
Measured Resistance R_s (Ω) @150Hz	0.176
Inertia J (kgm^2)	0.012
Calculated PM Flux (Wb)	0.18
Pairs of poles	3

The parameters for the 7.7 kW PM machine are applied to the model, shown in Table 6.2.

The working conditions for the parameter identification are shown in Figure 6.7 and Figure 6.8. The machine is accelerated to $900rpm$ in a no-load condition. After the speed is stable, a load torque $T_L = 5Nm$ is added at $t = 1s$. A small speed spike can be observed in Figure 6.7.

As discussed in Section 6.3.2, perturbation is required for RLS algorithm. In the simulation, i_d is set to $3A \pm 2A$, while i_q follows the speed controller output. The current loop tracking is shown in Figure 6.8. It can be observed that i_q oscillates with the perturbation in i_d.

The parameter identification results are shown in Figure 6.9. The rotor speed is shown in Figure 6.7 and the dq axis currents are shown in Figure 6.8 . The results show that the L_d and flux have the most stable estimation, while the estimation for L_q and R_s has a large error in a no-load condition. After adding a 5 Nm load, L_q and R_s starts to converge, and a small error still remains.

For the RLS algorithm, there are two factors that significant to the identification results. One is the perturbation, and the other one is the forgotten factor.

In this simulation, the perturbation is introduced to the d-axis current (Figure 6.8). If the perturbation is removed, i.e. set $i_d = 3A$ in constant. The estimation results are shown in Figure 6.10. It is proved that RLS cannot converge to a constant value, all four parameters' identification have failed.

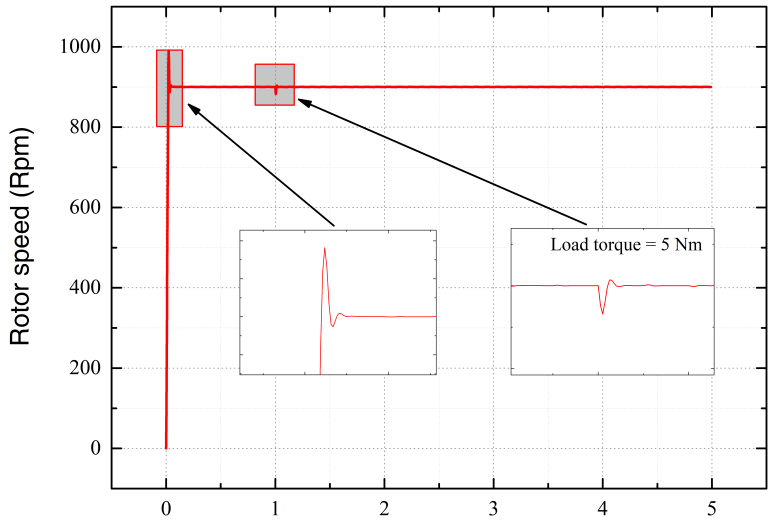

Figure 6.7: Simulation for RLS: rotor speed

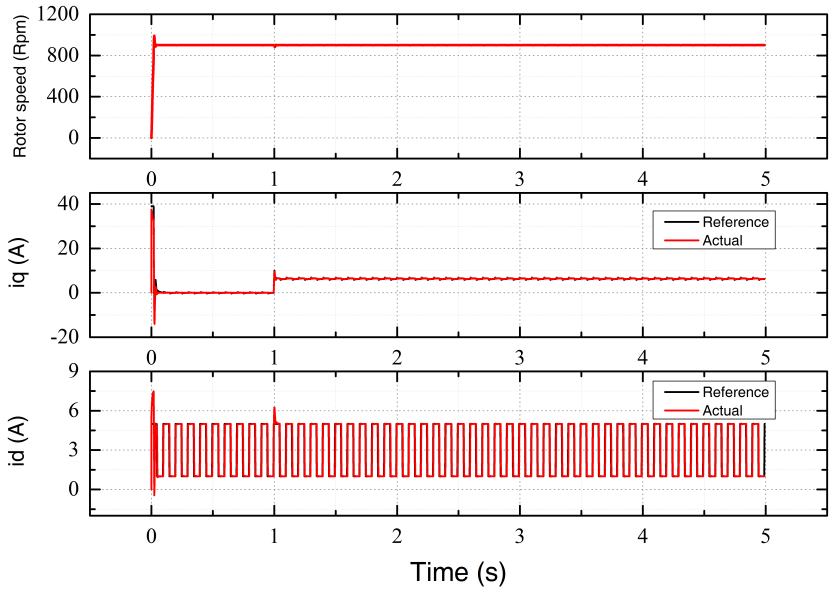

Figure 6.8: Simulation for RLS: stator current in $d-q$

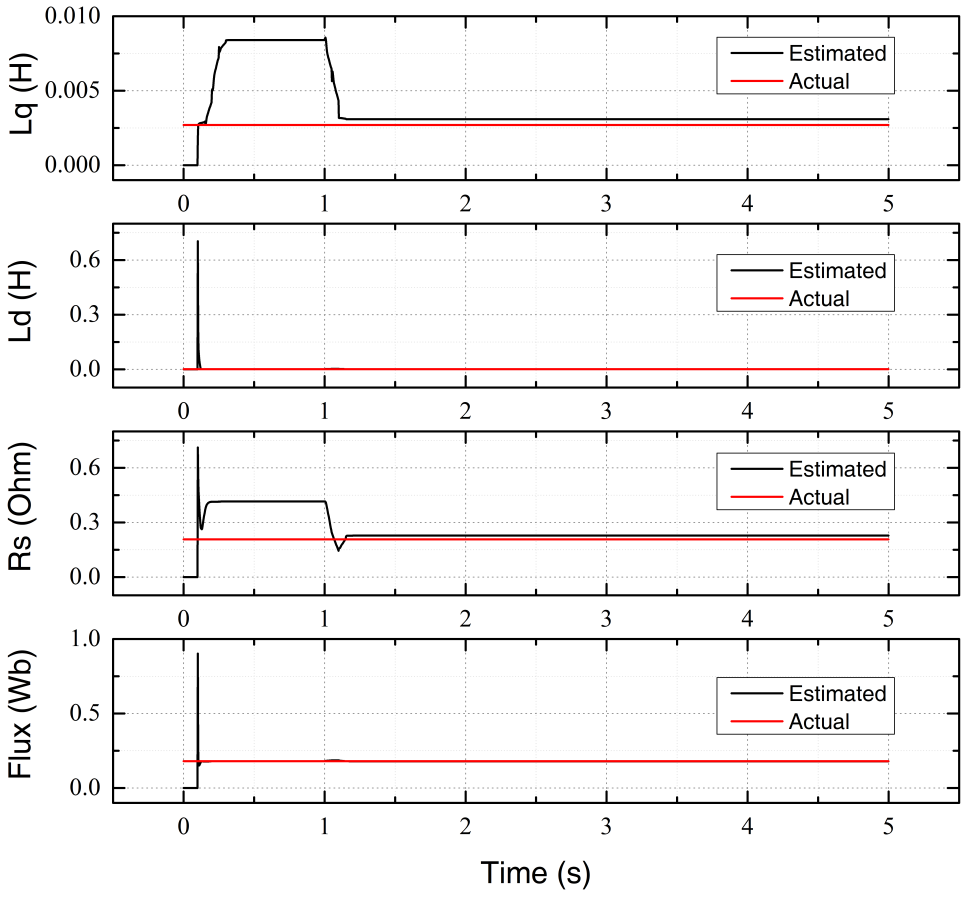

Figure 6.9: Simulation for RLS: identification results 1

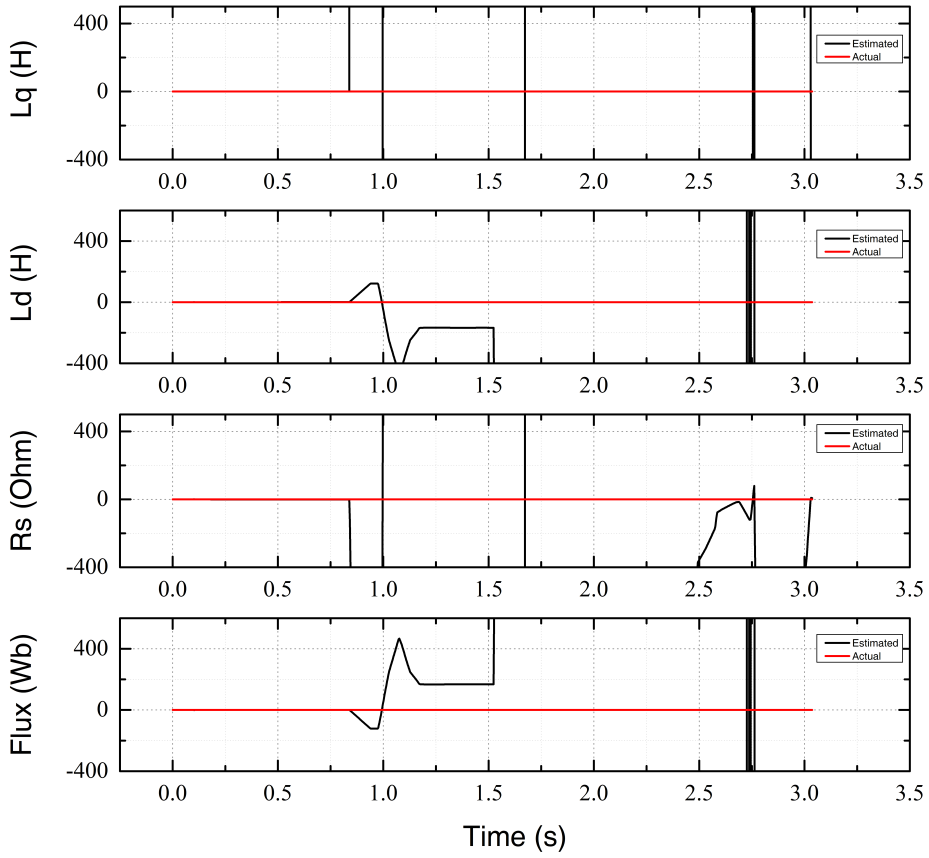

Figure 6.10: Simulation for RLS: identification results 2
(Failed due to no perturbation is introduced to i_d)

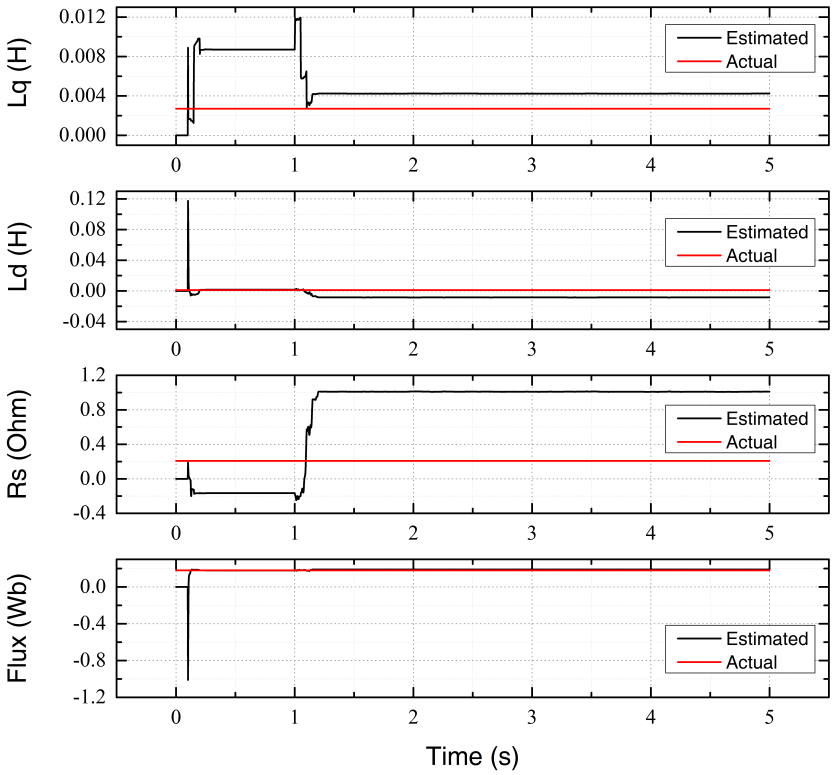

Figure 6.11: Simulation for RLS: identification results 3
(failed when forgotten factor is set to $\lambda = 0.9$, normal value is $\lambda = 0.99$)

The forgotten factor is the parameter that describes the recursive character in the RLS. λ in Equation (6.18) presents forgotten factor. It is a value between 0 and 1. The larger λ leads to less historical data influence on the final result. For a well identified result in Figure 6.9, $\lambda = 0.99$.

$$\begin{aligned} \theta_{est(k)} &= \theta_{est(k-1)} + K_{(k)} \cdot \epsilon_{(k)} \\ \epsilon_{(k)} &= y_{(k)} - \varphi^T_{(k)} \cdot \theta_{est(k-1)} \\ K_{(k)} &= P_{(k-1)} \cdot \varphi_{(k)} [\lambda \cdot I_n + \varphi^T_{(k)} \cdot P_{(k-1)} \cdot \varphi_{(k)}] \\ P_{(k)} &= [I_n - K_{(k)} \cdot \varphi^T_{(k)}] \cdot P_{(k-1)} / \lambda \end{aligned} \tag{6.18}$$

If λ is set to 0.9, the identification results are presented in Figure 6.11. L_q and L_d estimation have more error than the $\lambda = 0.99$ result. For R_s the error become very large.

6.3.4 Hardware Test

Same as the Luenberger observer test (Section 6.2), the Hardware test is carried out on the 3 kW PMSM test rig introduced in Section 4.6.1. The test is carried out when the speed and torque are stable. The working conditions are shown in Figure 6.12. The perturbation i_d is shown.

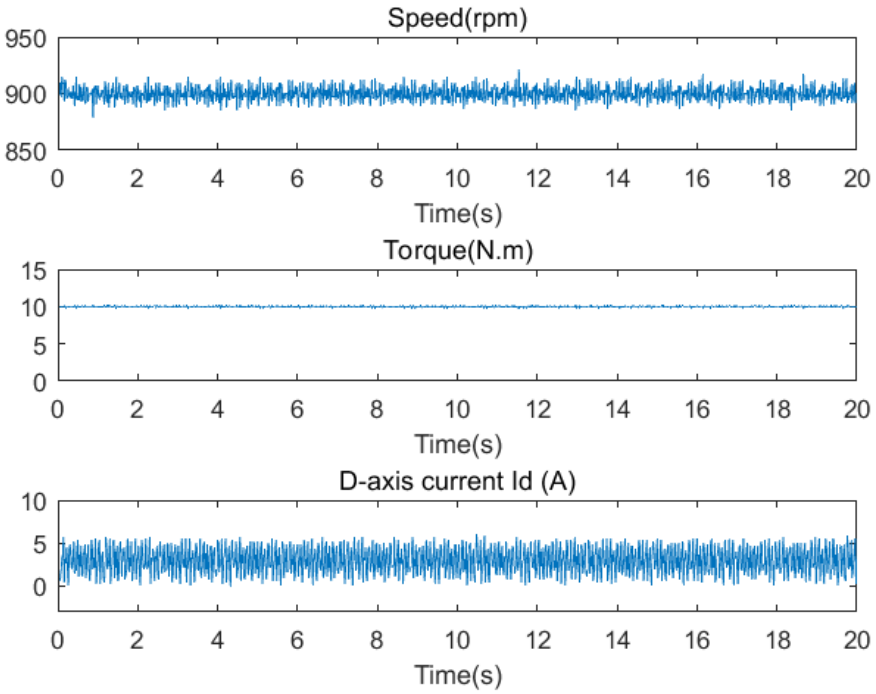

Figure 6.12: Motor working condition during RLS estimation

The estimation results are shown in Figure 6.13. In contrast to simulation results, these hardware identification vectors are converged. The estimated value of L_q is very accurate, L_d and flux is estimated with some error, and the estimated flux seems close to the Luenberger observer estimated result ($K_t = 0.21$). At the same time, the resistance cannot achieve a satisfied estimation. One possible reason is that the current signal resolution is not high enough. The Semikorn inverter build-in current sensor ADC has a range of 1200 A with 12 bits digital output (4096 digits), which leads to approximately 0.29 A/digit. If the current sensor resolution can be increased in a future test, the RLS results can be improved.

The forgotten factor is crucial for the estimation. Generally speaking, it re-

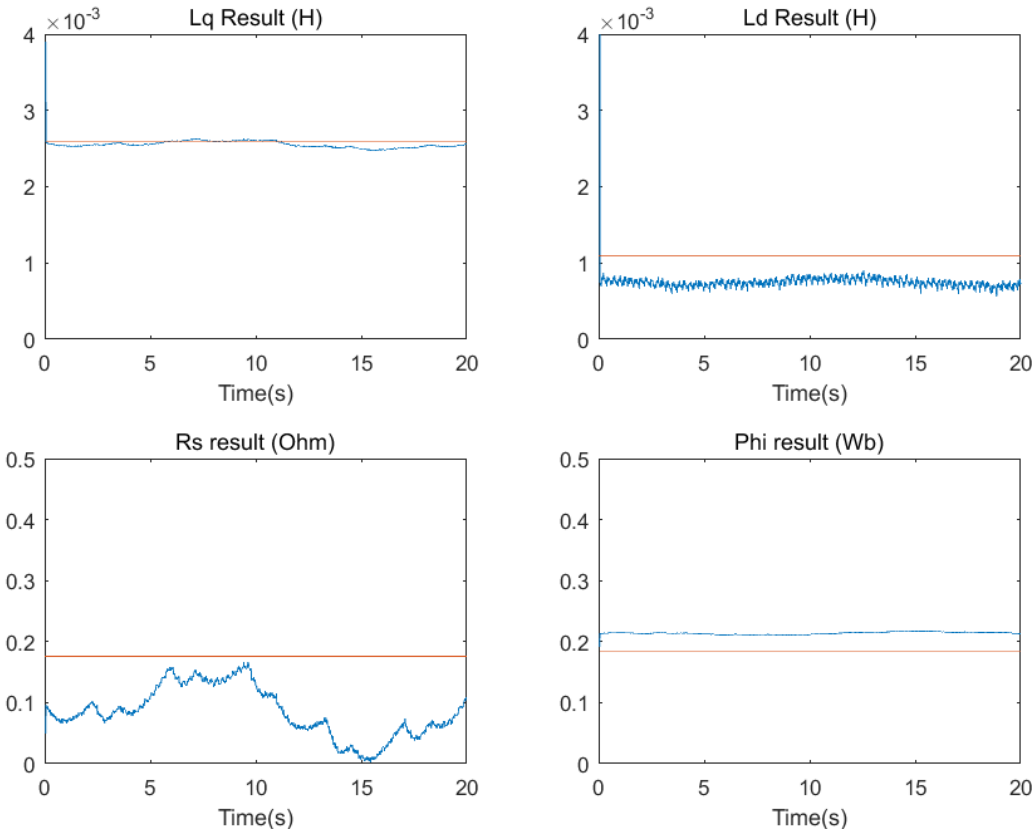

Figure 6.13: Parameter identification results for RLS (Red: reference; Blue: estimation result)

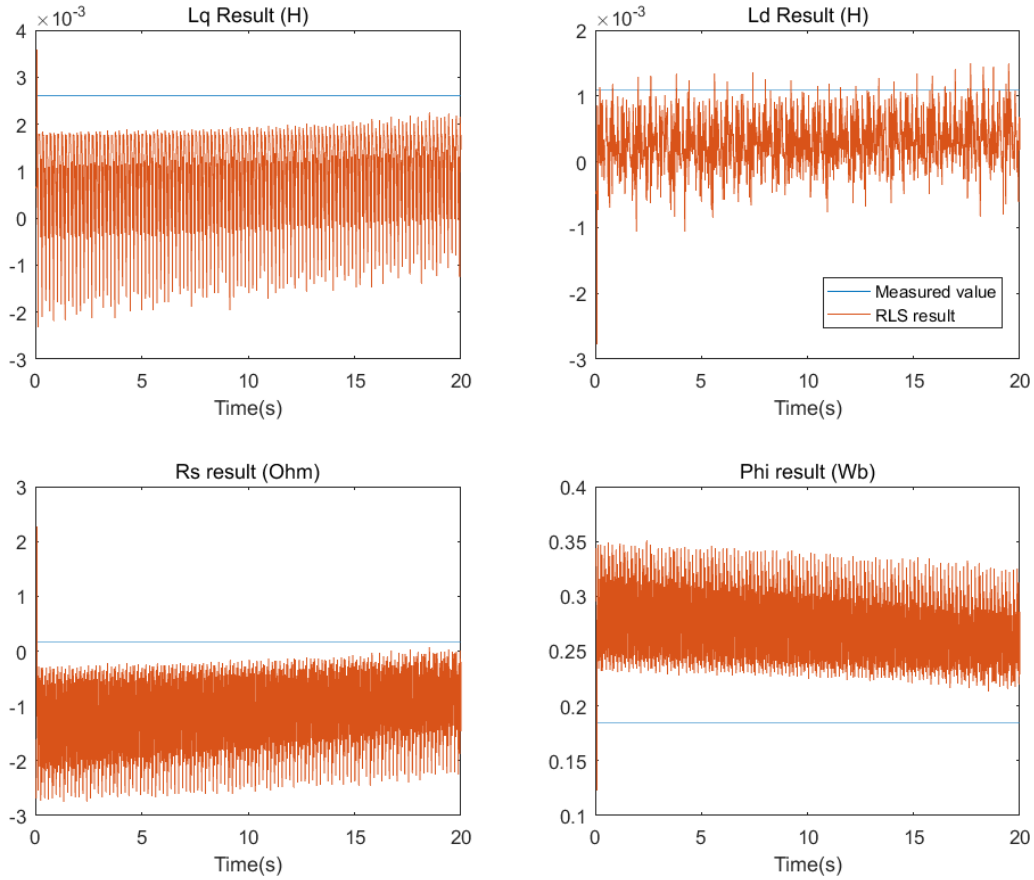

Figure 6.14: Parameter identification results for RLS: Forgotten factor=0.99

flects how the algorithm deal with noise, and how fast its response to the dynamic change. There are no quantitative rules to decide the value, in the simulation, $\lambda = 0.99$ lead to a better result, however, the same value may not working well in hardware test. Generally speaking, hardware environments are more strict to simulation. Accuracy is sacrificed for higher robustness.

The forgotten factor should go closer to 1 for a system that contains more noise. The forgotten factor of $\lambda = 0.999$ and $\lambda = 0.99$ are tested. From the estimation results, $\lambda = 0.999$ is a better choice. Results of $\lambda = 0.99$ are presented in Figure 6.14, the identification results suffer from both large oscillation and error. None of the parameters is successfully identified.

6.4 Summary

In this chapter, the parameter identification issue for the PMSM is discussed. The key parameters in marine PMSM are compared.The inductance L_d and L_q, stator resistance R_s, and rotor flux ψ are identified as the most important parameters.

An offline method to measure rotor flux is introduced in Chapter 2. In this chapter, two online identification methods are introduced, namely the Luenberger observer, and the recursive least square (RLS) approach. The mearsurment and two online identifications are made on the same hardware, their values are compared, and the possible reasons for the differences are discussed.

For the rotor flux Luenberger observer, The equations are shown, and it is verified with hardware test. There is an error of 6 % between the flux estimation result and the measured flux. In addition, the robustness of the Luenberger observer against errors on the other parameters is very important. In this chapter, the Luenberger observer is tested with 50 % error is added to the inductances L_d, L_q, and resistance R_s. The hardware results are shown to give an explicit view of the influences.

Lastly, the observer based on the RLS method is introduced. This method can identify L_q, L_d, R_s and ψ at the same time. The equations are shown, the design of i_d perturbation and the forgotten factor is discussed. Then the algorithm is verified on simulation. It shows that the estimation results are promising with properly setting of forgotten factor and perturbation. However, in the experiment results, the rotor resistance R_s cannot be identified properly. This differs from the simulation is most likely caused by the noise or error in the measurement of the input signal. In the simulation, R_s is the most sensitive one among the identified four. It can be regarded as the small error in simulation amplified by the noise when it goes to hardware test.

In chapter 7, the conclusion of this thesis is drawn. The future works for all chapters are proposed.

Chapter 7

Conclusions and Recommendations

7.1 Conclusions

On the SPS, a majority of energy generated is consumed by the propulsion system, in particular, by the electric machines in the main thrusters and the azimuthing thrusters. It is legitimate to say that the design of electric machine drive in marine applications is significant to the overall performance of the MES or the future AES.

The Optimal reset controller (ORC) is introduced to the speed loop tracking to improve the dynamic response of the electric machines. ORC is considered as a combination of a base linear controller and an optimal controller. In industrial applications, the FOC scheme with a PI controller is still one of the most widely implemented approaches. In such a system, ORC has been introduced as an add-on to the existing PI controller to improve its dynamic performance. The procedures of implementing the ORC are presented in detail. After simulation, HIL and hardware tests, it is proved that the ORC relatively improves the system performance in speed loop trajectory tracking. The overall tracking error is reduced, and the overshoots are almost completely eliminated. The sudden load change is another challenge in marine applications. On a continuous test, the speed variation that induced by sudden load change is also suppressed by the ORC.

Sensorless control for an electric machine is another topic that discussed in this thesis, especially for the PMSM. There are two reasons why PMSM sensor-

less control is more important than that for IM. First, PMSM is known for its high power density and efficiency. In marine applications, many working environments that suitable for PM machines are compact in space (e.g. tunnel thruster, podded propeller). It is impractical to install speed sensors in many applications considering difficulties in manufacturing and maintenance. Secondly, the rotor flux in a PMSM is dependent on the rotor physical position. As a result, the misalignment in the identification of rotor position leads to an efficiency reduce. Lastly, introducing the FOC with a wrong flux direction increases the risk of permanent demagnetizing. Chapter 4 focuses on the starting period of a sensorless controller. A smooth transition method is proposed to prevent the current overshoot, the physical vibration, and noise during the startup process of a closed-loop sensorless FOC. The stage before (open loop start) and after (sensorless FOC based on back-EMF) the transient is investigated and analyzed. Thorough hardware test results are provided to analysis the PMSM sensorless start issue and test the proposed algorithms.

The machine parameters are varying according to the working conditions and environments. The manufacturer generally provides a set of parameters that measured through off-line tests in laboratory conditions. However, the mechanical parameters require calibration every time when the machine is installed. In addition, the electric ones require on-line identification since their values change with working conditions. Since many modern control algorithms are model based, their robustnesses against parameter variation are usually required. In the marine IM, the parameter identification case is more specific. The rotor time constant τ_r has a direct influence on the calculation of the slip speed in i-FOC. Although the dq axis misalignment is caused by a τ_r variation, the torque balance is still achieved (similarly, torque balance is also a key to analysis the PMSM behaviour upon an open loop start in Chapter 4). A method is proposed to calculate the error angle with the i_q and i_d measured in the new torque balance. The proposed method is verified by both simulation and hardware test.

For the PMSM, the flux estimation technique with a Luenberger observer is tested. The estimation results are compared with the measurement value. However, to achieve more accurate result with the Luenberger observer, the accurate knowledge of the other parameters are required. A robustness test is carried out. Next, a full order observer based on RLS is implemented on the PMSM. In contrast to the previous works, the selection of the forgotten factor and the injection of perturbation signal is discussed. The simulation identified all the parameters

successfully. In the hardware test results for stator resistance is not satisfactory. It is most likely caused by the inevitable noise in the current sensor. The noise signal is considerably amplified by the matrix calculation in RLS, which makes it difficult to implement in hardware.

7.2 Recommendations for Future Research

There are several interesting orientations that worth pursuing beyond this thesis. They are listed as future work due to time limitations or hardware constraints.

A. Hardware in the loop test

The HIL test is a helpful tool to test machine controllers. Researchers that choose HIL test normally value its safety or flexibility. However, there is another benefit about HIL test that commonly got overlooked.

Many algorithms that work perfectly in the simulation may fail at a hardware test. The reason may be complicated and coupled. As a test plan that combines hardware and simulation, running hardware in the loop test can provide more information to the researcher. Take the RLS parameter identification method as an example. The identification fail in hardware test may be caused by noise, DSP calculation capacity or the error is in the parameter provided by the manufacturer. Running an HIL test can tell more.

B. The ORC with time variant reset-intervals

ORC resets the linear integrator state in a constant time intervals. Given the characteristic of each controller: for longer reset time interval, the controller performance is closer to the base linear controller, while shorter reset time means that the ORC have more influence to the system and better dynamic response is achieved.

If the time interval can be set to time-variant according to various control stages, the performance of ORC will be improved. However, the criterion to determine reset interval is hard to define. Additionally, the stability analyses are required in that case.

C. Further improvements on the smooth transition method

Simulation and hardware test results in Chapter 4 has proven that the smooth transition method is better than the direct transition. However, it is also observed that when the decreasing i_q is close to the setpiont value, and the error angle decreases dramatically until finally reaches zero. This phenomenon is shown in

the red boxed time period in Figure 7.1. If the changing ratio of i_q can be reduced in the red boxed section, the mechanical performance of PMSM can be further improved.

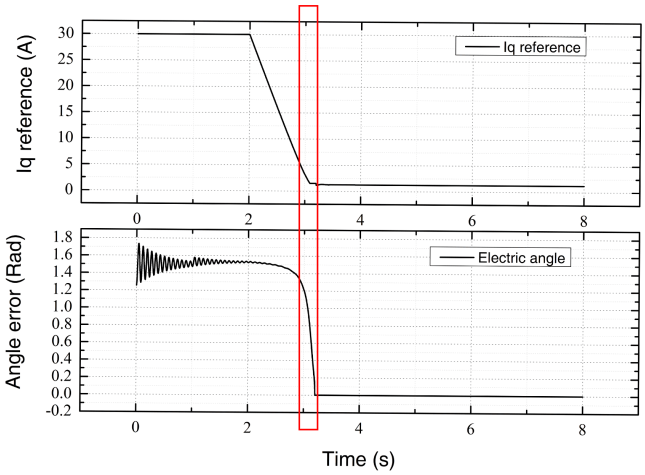

Figure 7.1: Simulation result on q-axis current and angle error

A potential approach is adding a compensation loop so that the i_q decreasing ratio is limited in the "red-boxed" period to avoid the sudden change in rotor error angle. In addition, as an industrial application, the current measurement accuracy brings more challenge to this research.

D. Continuous work on rotor time constant identification with the proposed method

The rotor time constant variation is mostly contributed to the change in rotor resistance R_r. On the other hand, although the influence on inductance L_r is minimal, it cannot be ignored. Further analysis would focus on the various working conditions of the machine. In addition, if there is an efficient method to solve the equation contains trigonometric function, the proposed method can be developed to an on-line identification algorithm. Continuous work will be carried out in the future.

E. The effect of magnetization saturation in the PMSM parameter identification

The parameter identification for the PMSM is introduced in Chapter 6. The identification results show that the stator resistance R_s is not well identified, while

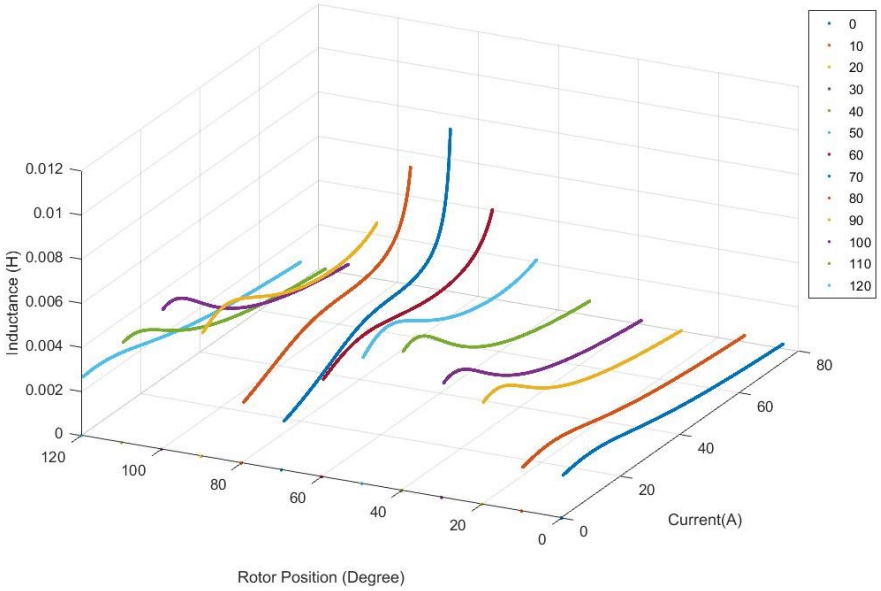

Figure 7.2: Pulse voltage test results on PMSM inductance

the results of L_d, L_q and λ suffer a small error. The most probable cause is within the noise in the current signal collection.

In addition, there may be other factors affecting the hardware test result. It is assumed that L_d, L_q are constant during the test. However, they may be influenced by the saturation effect and vary according to the current levels. This can be proved by another test that carried out on the 3 kW PMSM test rig.

This test is enlightened by the double pulse test that is popular in the power electronics topics. However, the second pulse is not necessary. An IGBT switch is connected in phase to phase on the PMSM. Experiment set up is shown in Figure 7.3a. A pulsed voltage of $600V$, duration of $200\mu s$ is given. The current is logged with an oscilloscope, each screenshot represents the experiment result of a particular rotor angle. One of the total 13 oscilloscope screenshots is shown in Figure 7.3b, the section $'a'$ *to* $'b'$ (labeled in two cyan vertical lines) shows the current variation through time, i.e., $\frac{di}{dt}$. The inductance is found with the relationship between voltage and current.

$$L = \frac{1}{v}\frac{di}{dt}$$

This test is performed under standstill. Since the inductance L_d, L_q for interior

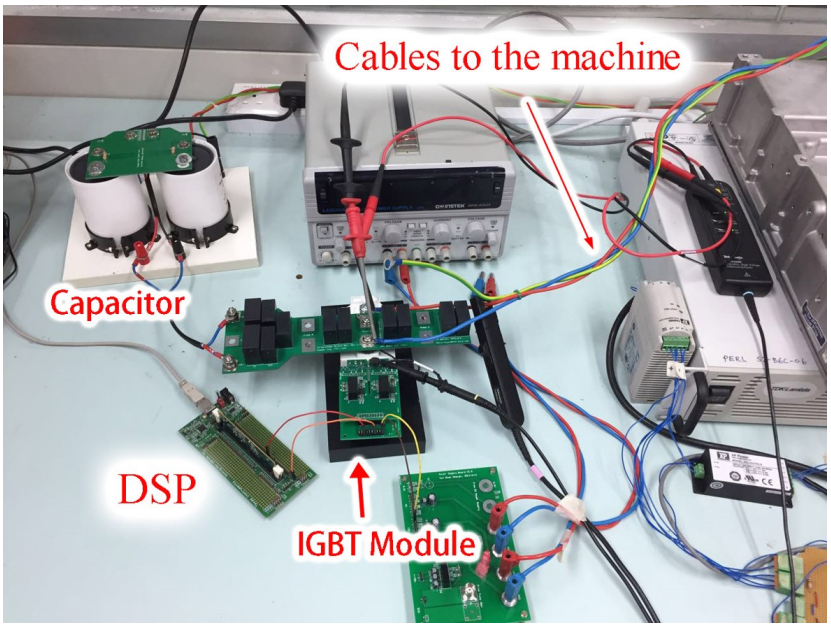

(a) Experiment set up

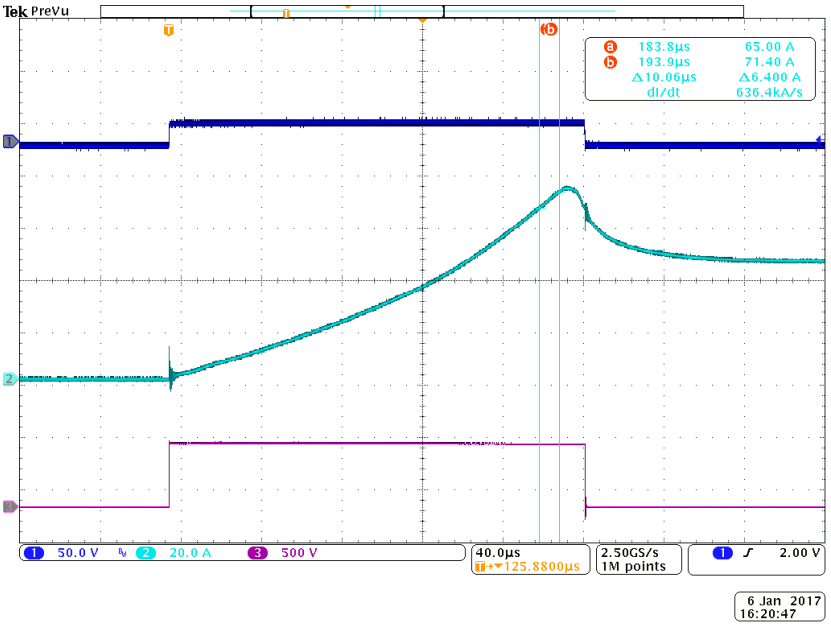

(b) Scope screenshot
Blue: gate signal; Cyan: current measurement;
Red: Voltage output

Figure 7.3: Pulse voltage test on PMSM inductance: experiment

PM are rotor position dependence, multiple tests are made, and experiment results are logged. Results are plotted in a 3D-form, shown in Figure 7.2. This plot shows the inductance within a current range of $0A$ *to* $80A$, the rotor position range of $0°$ *to* $120°$ in physical angle. Maximal value of $120°$ is chosen since the machine has three pole pairs. Which means the cycle for inductance variation is $120°$. Obviously, the inductance is not constant in the test result, showing that in the parameter identification tests, the current level is possible to influence the result. More knowledge about machine design and magnetization saturation is required to investigate this result. It would be an exciting area to explore in the future.

Bibliography

[1] T. Ericsen, N. Hingorani, and Y. Khersonsky, "Power electronics and future marine electrical systems," in *Petroleum and Chemical Industry Technical Conference, 13-15 Sept. 2004San Francisco, CA, USA*.

[2] Z. Jin, L. Meng, J. M. Guerrero, and R. Han, "Hierarchical control design for a shipboard power system with dc distribution and energy storage aboard future more-electric ships," *IEEE Transactions on Industrial Informatics*, vol. 14, no. 2, pp. 703–714, 2018.

[3] T. J. McCoy, "Electric ships past, present, and future [technology leaders]," *IEEE Electrification Magazine*, vol. 3, no. 2, pp. 4–11, 2015.

[4] K. Satpathi, A. Ukil, and J. Pou, "Short-circuit fault management in dc electric ship propulsion system: Protection requirements, review of existing technologies and future research trends," *IEEE Transactions on Transportation Electrification*, vol. 4, no. 1, pp. 272–291, 2018.

[5] G. Sulligoi, A. Tessarolo, V. Benucci, A. M. Trapani, M. Baret, and F. Luise, "Shipboard power generation: Design and development of a medium-voltage dc generation system," *IEEE Industry Applications Magazine*, vol. 19, no. 4, pp. 47–55, 2013.

[6] "China launches worlds first all-electric cargo ship, will use it to haul coal," https://www.rolls-royce.com/products-and-services.aspx, accessed: May-27-2018.

[7] "The electric revolution is coming to freighters and cruise ships," https://qz.com/1039133/the-electric-revolution-is-coming-to-freighters-and-cruise-ships/, accessed: May-27-2018.

[8] "Products of rolls-royce marine," https://www.rolls-royce.com/products-and-services.aspx, accessed: May-27-2018.

[9] W. P. Symington, A. Belle, H. D. Nguyen, and J. R. Binns, "Emerging technologies in marine electric propulsion," *Proceedings of the Institution of Mechanical Engineers, Part M: Journal of Engineering for the Maritime Environment*, vol. 230, no. 1, pp. 187–198, 2016.

[10] S. Jothibasu and S. Santoso, "New electric shipboard topologies for high resiliency," *IEEE Transactions on Power Systems*, vol. 33, no. 3, pp. 2975–2983, 2018.

[11] J. M. Miller, *Propulsion systems for hybrid vehicles*. John Wiley & Sons, London, 2004, vol. 45.

[12] G. Seenumani, J. Sun, and H. Peng, "Real-time power management of integrated power systems in all electric ships leveraging multi time scale property," *IEEE Transactions on Control Systems Technology*, vol. 20, no. 1, pp. 232–240, 2012.

[13] R. Geertsma, R. Negenborn, K. Visser, and J. Hopman, "Design and control of hybrid power and propulsion systems for smart ships: A review of developments," *Applied Energy*, vol. 194, pp. 30–54, 2017.

[14] "Rim-driven thruster," https://en.wikipedia.org/wiki/Rim-driven_thruster, accessed: May-30-2018.

[15] "Ieee standard test procedure for polyphase induction motors and generators," *IEEE Std 112-2017 (Revision of IEEE Std 112-2004)*, pp. 1–115, 2018.

[16] N. H. Doerry and J. C. Davis, "Integrated power system for marine applications," *Naval Engineers Journal*, vol. 106, no. 3, pp. 77–90, 1994.

[17] G. Sulligoi, A. Vicenzutti, and R. Menis, "All-electric ship design: From electrical propulsion to integrated electrical and electronic power systems," *IEEE Transactions on Transportation Electrification*, vol. 2, no. 4, pp. 507–521, 2016.

[18] Y. Xie, G. Seenumani, J. Sun, Y. Liu, and Z. Li, "A pc-cluster based real-time simulator for all-electric ship integrated power systems analysis and

optimization," in *Electric Ship Technologies Symposium, 21-25 May 2007, Virginia, United States.*

[19] G. Seenumani, J. Sun, and H. Peng, "A numerically efficient iterative procedure for hybrid power system optimization using sensitivity functions," in *American Control Conference, 11-15 Jul. 2007, New York, United States.*

[20] S. Bose, B. Natarajan, C. M. Scoglio, N. N. Schulz, D. M. Gruenbacher, and S. Das, "Shipboard power systems reconfigurationa cyber-physical framework for response time analysis," *IEEE Transactions on Industrial Informatics*, vol. 10, no. 1, pp. 439–449, 2014.

[21] F. D. Kanellos, G. J. Tsekouras, and N. D. Hatziargyriou, "Optimal demand-side management and power generation scheduling in an all-electric ship," *IEEE Transactions on Sustainable Energy*, vol. 5, no. 4, pp. 1166–1175, 2014.

[22] B. Zahedi, L. E. Norum, and K. B. Ludvigsen, "Optimized efficiency of all-electric ships by dc hybrid power systems," *Journal of Power Sources*, vol. 255, pp. 341–354, 2014.

[23] C.-L. Su, M.-C. Lin, and C.-H. Liao, "A method for evaluating energy efficiency to justify power factor correction in ship power systems," *IEEE Transactions on Industry Applications*, vol. 49, no. 6, pp. 2773–2782, 2013.

[24] J. F. Hansen and F. Wendt, "History and state of the art in commercial electric ship propulsion, integrated power systems, and future trends," *Proceedings of the IEEE*, vol. 103, no. 12, pp. 2229–2242, 2015.

[25] J. Thongam, M. Tarbouchi, A. Okou, D. Bouchard, and R. Beguenane, "Trends in naval ship propulsion drive motor technology," in *Electrical Power & Energy Conference (EPEC),IEEE, 21-23 Aug. 2013, Nova Scotia, Canada.*

[26] D. Alexander, "Hybrid electric drive for naval combatants." *Proceedings of the IEEE*, vol. 103, no. 12, pp. 2267–2275, 2015.

[27] S.-L. Dai, M. Wang, and C. Wang, "Neural learning control of marine surface vessels with guaranteed transient tracking performance," *IEEE Transactions on Industrial Electronics*, vol. 63, no. 3, pp. 1717–1727, 2016.

[28] W. He, S. S. Ge, B. V. E. How, Y. S. Choo, and K.-S. Hong, "Robust adaptive boundary control of a flexible marine riser with vessel dynamics," *Automatica*, vol. 47, no. 4, pp. 722–732, 2011.

[29] W. He, S. Zhang, and S. S. Ge, "Boundary control of a flexible riser with the application to marine installation," *IEEE Transactions on Industrial Electronics*, vol. 60, no. 12, pp. 5802–5810, 2013.

[30] "Dynamic positioning," https://en.wikipedia.org/wiki/Dynamic_positioning, accessed: May-12-2018.

[31] M. Benatmane, T. McCoy, T. Dalton, and T. Cooper, "Electric power generation and propulsion motor development for us navy surface ships," *Transactions-institute of Marine Engineers-series C-*, vol. 110, pp. 53–62, 1998.

[32] "Mermaid podded propulsors," https://www.rolls-royce.com/products-and-services/marine/product-finder/propulsors/podded-azimuthing-propulsors.aspx, accessed: Jul-28-2018.

[33] "Abb azipod gearless propulsion," https://new.abb.com/marine/systems-and-solutions/electric-propulsion/azipod, accessed: May-03-2018.

[34] "Drives and motors for winches," https://new.abb.com/drives/segments/winches, accessed: May-03-2018.

[35] "Marine products and systems," https://www.rolls-royce.com/~/media/Files/R/Rolls-Royce/documents/marine-product-finder/MPS%202017%20LR.pdf, accessed: May-03-2018.

[36] Q. Chen, W. Li, and G. Chen, "Fuzzy p+ id controller for a constant tension winch in a cable laying system." *IEEE Trans. Industrial Electronics*, vol. 64, no. 4, pp. 2924–2932, 2017.

[37] H. Henao, S. M. J. R. Fatemi, G. A. Capolino, and S. Sieg-Zieba, "Wire rope fault detection in a hoisting winch system by motor torque and current signature analysis," *IEEE Transactions on Industrial Electronics*, vol. 58, no. 5, pp. 1727–1736, 2011.

[38] F. Booth and M. Laye, "Lack of adequate appreciation of physical exercise's complexities can pre-empt appropriate design and interpretation in scientific discovery," *The Journal of Physiology*, vol. 587, no. 23, pp. 5527–5539, 2009.

[39] J. C. Dermentzoglou, "Investigating the incorporation of a doubly fed induction machine as a shaft generator into a ship's system," *ICEM 2014, Oral Presentation, Berlin, Germany*, pp. 2–5, 2014.

[40] J. L. Kirtley, A. Banerjee, and S. Englebretson, "Motors for ship propulsion," *Proceedings of the IEEE*, vol. 103, no. 12, pp. 2320–2332, 2015.

[41] P. L. Alger and R. Arnold, "The history of induction motors in america," *Proceedings of the IEEE*, vol. 64, no. 9, pp. 1380–1383, 1976.

[42] S. Chapman, *Electric machinery fundamentals*. Tata McGraw-Hill Education, New York, 2005.

[43] R. Ottersten, *Vector control of a double-sided PWM converter and induction machine drive*. Chalmers University of Technology, Sweden, 2000.

[44] M. Popescu, *Induction motor modelling for vector control purposes*. Helsinki University of Technology, Finland, 2000.

[45] R. Pena, J. Clare, and G. Asher, "Doubly fed induction generator using back-to-back pwm converters and its application to variable-speed wind-energy generation," *IEE Proceedings-electric Power Applications*, vol. 143, no. 3, pp. 231–241, 1996.

[46] D. Gerada, Z. Xu, D. Golovanov, and C. Gerada, "Comparison of electrical machines for use with a high-horsepower marine engine turbocharger," in *Electric Drives: Optimization in Control of Electric Drives (IWED), 31 Jan-3 Feb2018, Moscow*.

[47] D. Gerada, A. Mebarki, N. L. Brown, K. J. Bradley, and C. Gerada, "Design aspects of high-speed high-power-density laminated-rotor induction machines," *IEEE Transactions on Industrial Electronics*, vol. 58, no. 9, pp. 4039–4047, 2011.

[48] B. Robyns, B. Francois, P. Degobert, and J. P. Hautier, *Vector control of induction machines*. Springer, Berlin, 2012.

[49] K. Chau, C. C. Chan, and C. Liu, "Overview of permanent-magnet brushless drives for electric and hybrid electric vehicles," *IEEE Transactions on Industrial Electronics*, vol. 55, no. 6, pp. 2246–2257, 2008.

[50] E. W. Mukti, S. Wijanarko, A. Muqorobin, and L. Rozaqi, "Field oriented control design of inset rotor pmsm drive," in *AIP Conference Proceedings, 3-6 Oct. 2017, Moscow.*

[51] L. Liu, W. Liu, and D. A. Cartes, "Particle swarm optimization-based parameter identification applied to permanent magnet synchronous motors," *Engineering Applications of Artificial Intelligence*, vol. 21, no. 7, pp. 1092–1100, 2008.

[52] J. Dong, Y. Huang, L. Jin, and H. Lin, "Comparative study of surface-mounted and interior permanent-magnet motors for high-speed applications," *IEEE Transactions on Applied Superconductivity*, vol. 26, no. 4, pp. 1–4, 2016.

[53] J. F. Gieras, *Permanent magnet motor technology: design and applications.* CRC Press, Florida, 2002.

[54] S. Rauch and L. Johnson, "Design principles of flux-switch alternators," *Transactions of the American Institute of Electrical Engineers. Part III: Power Apparatus and Systems*, vol. 74, no. 3, pp. 1261–1268, 1955.

[55] M. Cheng, W. Hua, J. Zhang, and W. Zhao, "Overview of stator-permanent magnet brushless machines," *IEEE Transactions on Industrial Electronics*, vol. 58, no. 11, pp. 5087–5101, 2011.

[56] Y. Liao, F. Liang, and T. A. Lipo, "A novel permanent magnet motor with doubly salient structure," *IEEE Transactions on Industry Applications*, vol. 31, no. 5, pp. 1069–1078, 1995.

[57] I. Boldea, J. Zhang, and S. A. Nasar, "Theoretical characterization of flux reversal machine in low-speed servo drives-the pole-pm configuration," *IEEE Transactions on Industry Applications*, vol. 38, no. 6, pp. 1549–1557, 2002.

[58] R. P. Deodhar, S. Andersson, I. Boldea, and T. J. Miller, "The flux-reversal machine: A new brushless doubly-salient permanent-magnet machine," *IEEE Transactions on Industry Applications*, vol. 33, no. 4, pp. 925–934, 1997.

[59] Z. Zhu and J. Chen, "Advanced flux-switching permanent magnet brushless machines," *IEEE Transactions on Magnetics*, vol. 46, no. 6, pp. 1447–1453, 2010.

[60] W. Hua, M. Cheng, Z. Zhu, and D. Howe, "Analysis and optimization of back emf waveform of a flux-switching permanent magnet motor," *IEEE Transactions on Energy Conversion*, vol. 23, no. 3, pp. 727–733, 2008.

[61] D. Wang, H. Lin, S. Cheng, Z. Jia, and X. Zheng, "A novel circular winding brushless dc (cwbldc) machine with low torque ripple," in *Industrial Electronics Society, IECON, 9-12 Nov. 2015, Yokohama, JP.*

[62] C. S. Joice, S. Paranjothi, and V. J. S. Kumar, "Digital control strategy for four quadrant operation of three phase bldc motor with load variations," *IEEE Transactions on Industrial Informatics*, vol. 9, no. 2, pp. 974–982, 2013.

[63] C. W. De Silva, *Modeling and control of engineering systems.* CRC Press, Florida, 2009.

[64] C.-l. Xia, *Permanent magnet brushless DC motor drives and controls.* John Wiley & Sons, New Jersey, 2012.

[65] R. Carlson, M. Lajoie-Mazenc, and J. Fagundes, "Analysis of torque ripple due to phase commutation in brushless dc machines," *IEEE Transactions on Industry Applications*, vol. 28, no. 3, pp. 632–638, 1992.

[66] C.-S. Berendsen, G. Champenois, and A. Bolopion, "Commutation strategies for brushless dc motors: influence on instant torque," *IEEE Transactions on Power Electronics*, vol. 8, no. 2, pp. 231–236, 1993.

[67] S. Sung, G. Jang, and H. Lee, "Torque ripple and unbalanced magnetic force of a bldc motor due to the connecting wire between slot windings," *IEEE Transactions on Magnetics*, vol. 48, no. 11, pp. 3319–3322, 2012.

[68] Y. Liu, Z. Zhu, and D. Howe, "Direct torque control of brushless dc drives with reduced torque ripple," *IEEE Transactions on Industry Applications*, vol. 41, no. 2, pp. 599–608, 2005.

[69] J. Fang, H. Li, and B. Han, "Torque ripple reduction in bldc torque motor with nonideal back emf," *IEEE Transactions on Power Electronics*, vol. 27, no. 11, pp. 4630–4637, 2012.

[70] C. Xia, Y. Wang, and T. Shi, "Implementation of finite-state model predictive control for commutation torque ripple minimization of permanent-magnet brushless dc motor," *IEEE Transactions on Industrial Electronics*, vol. 60, no. 3, pp. 896–905, 2013.

[71] C. Xia, Y. Xiao, W. Chen, and T. Shi, "Torque ripple reduction in brushless dc drives based on reference current optimization using integral variable structure control," *IEEE Transactions on Industrial Electronics*, vol. 61, no. 2, pp. 738–752, 2014.

[72] P. Waide and C. U. Brunner, "Energy-efficiency policy opportunities for electric motor-driven systems," *IEA Energy Papers*, 2011.

[73] L. Lavrinovicha and J. Dirba, "Comparison of permanent magnet synchronous motor and synchronous reluctance motor based on their torque per unit volume," in *Electric Power Quality and Supply Reliability Conference (PQ), 11-13 June 2014, Rakvere, Estonia.*

[74] R. E. Betz and M. G. Jovanovic, "The brushless doubly fed reluctance machine and the synchronous reluctance machine-a comparison," *IEEE Transactions on Industry Applications*, vol. 36, no. 4, pp. 1103–1110, 2000.

[75] A. Consoli, C. Cavallaro, G. Scarcella, and A. Testa, "Sensorless torque control of syncrel motor drives," *IEEE Transactions on Power Electronics*, vol. 15, no. 1, pp. 28–35, 2000.

[76] R. Morales-Caporal and M. Pacas, "A predictive torque control for the synchronous reluctance machine taking into account the magnetic cross saturation," *IEEE Transactions on Industrial Electronics*, vol. 54, no. 2, pp. 1161–1167, 2007.

[77] W. Duesterhoeft, M. W. Schulz, and E. Clarke, "Determination of instantaneous currents and voltages by means of alpha, beta, and zero components," *Transactions of the American Institute of Electrical Engineers*, vol. 70, no. 2, pp. 1248–1255, 1951.

[78] R. Park, "Two reaction theory of synchronous machines," *Trans. AIEE*, vol. 48, p. 716, 1929.

[79] B. Wu and M. Narimani, *High-power converters and AC drives*. John Wiley & Sons, New Jersey, 2017, vol. 59.

[80] J. N. Nash, "Direct torque control, induction motor vector control without an encoder," *IEEE Transactions on Industry Applications*, vol. 33, no. 2, pp. 333–341, 1997.

[81] M. Tursini, F. Parasiliti, and D. Zhang, "Real-time gain tuning of pi controllers for high-performance pmsm drives," *IEEE Transactions on Industry Applications*, vol. 38, no. 4, pp. 1018–1026, 2002.

[82] T. Pajchrowski, "The direct drive with variable moment of inertia in the structure of the reference model," in *Power Electronics and Motion Control Conference and Exposition (PEMC), 21-25 Sep. 2014, Turkey.*

[83] C.-H. Liu and Y.-Y. Hsu, "Design of a self-tuning pi controller for a statcom using particle swarm optimization," *IEEE Transactions on Industrial Electronics*, vol. 57, no. 2, pp. 702–715, 2010.

[84] B. Singh, S. S. Murthy, and S. Gupta, "Statcom-based voltage regulator for self-excited induction generator feeding nonlinear loads," *IEEE Transactions on Industrial Electronics*, vol. 53, no. 5, pp. 1437–1452, 2006.

[85] M. Cheng, Q. Sun, and E. Zhou, "New self-tuning fuzzy pi control of a novel doubly salient permanent-magnet motor drive," *IEEE Transactions on Industrial Electronics*, vol. 53, no. 3, pp. 814–821, 2006.

[86] Y. Song, X. Huang, and C. Wen, "Robust adaptive fault-tolerant pid control of mimo nonlinear systems with unknown control direction," *IEEE Transactions on Industrial Electronics*, vol. 64, no. 6, pp. 4876–4884, 2017.

[87] S. Bolognani and M. Zigliotto, "Fuzzy logic control of a switched reluctance motor drive," in *Industry Applications Society Annual Meeting, 2-8 Oct. 1993, Toronto, Ontario, Canada.*

[88] X. Zhang, G. Foo, M. D. Vilathgamuwa, K. J. Tseng, B. S. Bhangu, and C. Gajanayake, "Sensor fault detection, isolation and system reconfiguration

based on extended kalman filter for induction motor drives," *IET Electric Power Applications*, vol. 7, no. 7, pp. 607–617, 2013.

[89] J. Talla, V. Q. Leu, V. Šmídl, and Z. Peroutka, "Adaptive speed control of induction motor drive with inaccurate model," *IEEE Transactions on Industrial Electronics*, vol. 65, no. 11, 2018.

[90] R.-J. Wai and K.-H. Su, "Adaptive enhanced fuzzy sliding-mode control for electrical servo drive," *IEEE Transactions on Industrial Electronics*, vol. 53, no. 2, pp. 569–580, 2006.

[91] W.-J. Wang and J.-Y. Chen, "A new sliding mode position controller with adaptive load torque estimator for an induction motor," *IEEE Transactions on Energy Conversion*, vol. 14, no. 3, pp. 413–418, 1999.

[92] K.-K. Shyu and H.-J. Shieh, "A new switching surface sliding-mode speed control for induction motor drive systems," *IEEE Transactions on Power Electronics*, vol. 11, no. 4, pp. 660–667, 1996.

[93] J. R. Arribas and C. V. Gonzalez, "Optimal vector control of pumping and ventilation induction motor drives," *IEEE Transactions on Industrial Electronics*, vol. 49, no. 4, pp. 889–895, 2002.

[94] F. Alonge, F. D'Ippolito, G. Giardina, and T. Scaffidi, "Design and low-cost implementation of an optimally robust reduced-order rotor flux observer for induction motor control," *IEEE Transactions on Industrial Electronics*, vol. 54, no. 6, pp. 3205–3216, 2007.

[95] H. Wang, X. Ge, and Y.-C. Liu, "Second-order sliding-mode mras observer based sensorless vector control of linear induction motor drives for medium-low speed maglev applications," *IEEE Transactions on Industrial Electronics*, 2018.

[96] W. Tang, J. Yang, G. Zhang, Y. Sun, S. Ademi, F. Blaabjerg, and Q. Zhu, "Sensorless control of brushless doubly-fed induction machine using a control winding current mras observer," *IEEE Transactions on Industrial Electronics*, 2018.

[97] M. H. Holakooie, M. Ojaghi, and A. Taheri, "Direct torque control of six-phase induction motor with a novel mras-based stator resistance estimator,"

IEEE Transactions on Industrial Electronics, vol. 65, no. 10, pp. 7685–7696, 2018.

[98] G. Witvoet, W. H. Aangenent, W. P. H. Heemels, M. van de Molengraft, and M. Steinbuch, "H 2 performance analysis of reset control systems," in *46th IEEE Conference on Decision and Control, 12-14 Dec. 2007, New Orleans, LA, USA*.

[99] J. Clegg, "A nonlinear integrator for servomechanisms," *Transactions of the American Institute of Electrical Engineers, Part II: Applications and Industry*, vol. 77, no. 1, pp. 41–42, 1958.

[100] K. Krishnan and I. Horowitz, "Synthesis of a non-linear feedback system with significant plant-ignorance for prescribed system tolerances," *International Journal of Control*, vol. 19, no. 4, pp. 689–706, 1974.

[101] Y. Chait and C. Hollot, "On horowitz's contributions to reset control," *International Journal of Robust and Nonlinear Control: IFAC-Affiliated Journal*, vol. 12, no. 4, pp. 335–355, 2002.

[102] H. Hu, Y. Zheng, Y. Chait, and C. Hollot, "On the zero-input stability of control systems with clegg integrators," in *American Control Conference, 4-6 Jun. 1997, New Mexico, United States*.

[103] Q. Chen, Y. Chait, and C. Hollot, "Analysis of reset control systems consisting of a fore and second-order loop," *Journal of Dynamic Systems, Measurement, and Control*, vol. 123, no. 2, pp. 279–283, 2001.

[104] I. Horowitz and P. Rosenbaum, "Non-linear design for cost of feedback reduction in systems with large parameter uncertainty," *International Journal of Control*, vol. 21, no. 6, pp. 977–1001, 1975.

[105] O. Beker, C. V. Hollot, and Y. Chait, "Plant with integrator: an example of reset control overcoming limitations of linear feedback," *IEEE Transactions on Automatic Control*, vol. 46, no. 11, pp. 1797–1799, 2001.

[106] T. Loquen, S. Tarbouriech, and C. Prieur, "Stability analysis for reset systems with input saturation," in *46th IEEE Conference on Decision and Control, 12-14 Dec. 2007, New Orleans, LA, USA*.

[107] A. Baños, F. Perez, and J. Cervera, "Networked reset control systems with discrete time-varying delays," in *IECON 36th Annual Conference on IEEE Industrial Electronics Society, 10-13 Sep. 2010, Glendale, Arizona.*

[108] F. Perez, A. Baños, and J. Cervera, "Design of networked periodic reset control systems," in *Industrial Electronics (ISIE), 27-30 Jun. 2011, Gdansk, Poland.*

[109] A. Baños, J. Carrasco, and A. Barreiro, "Reset times-dependent stability of reset control systems," *IEEE Transactions on Automatic Control*, vol. 56, no. 1, pp. 217–223, 2011.

[110] L. Leyao, W. Fen, and W. Xinmin, "A reset controller design method for mimo linear systems," in *Control Conference (CCC), 5-9 Jul.2013, Xi'an, China.*

[111] Y. Yamakawa, K. Kamimura, T. Yamazaki, and S. Kurosu, "Air-conditioning control system using pd control with adjustable manual reset," in *SICE Annual Conference, 18-21 Aug. 2010, Taiwan.*

[112] Y. Guo, Y. Wang, L. Xie, and J. Zheng, "Stability analysis and design of reset systems: Theory and an application," *Automatica*, vol. 45, no. 2, pp. 492–497, 2009.

[113] Y. Guo, Y. Wang, L. Xie, H. Li, and W. Gui, "Optimal reset law design of reset control systems with application to hdd systems," in *Decision and Control, 15-18 Dec. 2009, Shanghai, China.*

[114] H. Li, C. Du, Y. Wang, and Y. Guo, "Discrete-time optimal reset control for hard disk drive servo systems," *IEEE Transactions on Magnetics*, vol. 45, no. 11, pp. 5104–5107, 2009.

[115] H. Li, C. Du, and Y. Wang, "Discrete-time h 2 optimal reset control with application to hdd track-following," in *Control and Decision Conference, 17-19 June 2009, Guilin, China.*

[116] S. Wu, Y. Wang, and S. Cheng, "Optimal reset control design for current control and uncertainties estimation in permanent magnet synchronous," *IET Electric Power Applications*, vol. 6, no. 2, pp. 122–132, 2012.

[117] F. Huerta, J. K. Gruber, M. Prodanovic, and P. Matatagui, "Power-hardware-in-the-loop test beds: evaluation tools for grid integration of distributed energy resources," *IEEE Industry Applications Magazine*, vol. 22, no. 2, pp. 18–26, March 2016.

[118] Y. Li, D. M. Vilathgamuwa, and P. C. Loh, "Design, analysis, and real-time testing of a controller for multibus microgrid system," *IEEE Transactions on Power Electronics*, vol. 19, no. 5, pp. 1195–1204, 2004.

[119] M. Steurer, C. S. Edrington, M. Sloderbeck, W. Ren, and J. Langston, "A megawatt-scale power hardware-in-the-loop simulation setup for motor drives," *IEEE Transactions on Industrial Electronics*, vol. 57, no. 4, pp. 1254–1260, 2010.

[120] K. Lian and P. Lehn, "Real-time simulation of voltage source converters based on time average method," *IEEE Transactions on Power Systems*, vol. 20, no. 1, pp. 110–118, 2005.

[121] P. Kotsampopoulos, V. Kleftakis, G. Messinis, and N. Hatziargyriou, "Design, development and operation of a phil environment for distributed energy resources," in *IECON 2012-38th Annual Conference on IEEE Industrial Electronics Society, 25-29 Oct. 2012, Montral, Canada.*

[122] "Tamagawa seiki co., ltd." https://www.tamagawa-seiki.com/products/resolver-synchro/, accessed: May-08-2018.

[123] "Singlsyn vr type resolver," https://www.tamagawa-seiki.com/downloads/pdf/#link02, accessed: May-08-2018.

[124] "An introduction to tunnel thrusters in ships design and application," https://www.marineinsight.com/naval-architecture/introduction-to-tunnel-thrusters-ships/, accessed: Jul-28-2018.

[125] "Technical information-propulsion-download," https://www.rolls-royce.com/~/media/Files/R/Rolls-Royce/documents/marine-product-finder/propulsion-brochure.pdf, accessed: Jul-28-2018.

[126] A. Sarikhani and O. A. Mohammed, "Sensorless control of pm synchronous machines by physics-based emf observer," *IEEE Transactions on Energy Conversion*, vol. 27, no. 4, pp. 1009–1017, 2012.

[127] O. Wallmark, L. Harnefors, and O. Carlson, "Sensorless control of pmsm drives for hybrid electric vehicles," in *Power Electronics Specialists Conference, 20-23 Jun. 2004, Aachen, Germany.*

[128] M. Rashed, P. F. MacConnell, A. F. Stronach, and P. Acarnley, "Sensorless indirect-rotor-field-orientation speed control of a permanent-magnet synchronous motor with stator-resistance estimation," *IEEE Transactions on Industrial Electronics*, vol. 54, no. 3, pp. 1664–1675, 2007.

[129] T. Bernardes, V. F. Montagner, H. A. Gründling, and H. Pinheiro, "Discrete-time sliding mode observer for sensorless vector control of permanent magnet synchronous machine," *IEEE Transactions on Industrial Electronics*, vol. 61, no. 4, pp. 1679–1691, 2014.

[130] Z. Zhang, Y. Zhao, W. Qiao, and L. Qu, "A space-vector-modulated sensorless direct-torque control for direct-drive pmsg wind turbines," *IEEE Transactions on Industry Applications*, vol. 50, no. 4, pp. 2331–2341, 2014.

[131] S. Chi, Z. Zhang, and L. Xu, "Sliding-mode sensorless control of direct-drive pm synchronous motors for washing machine applications," *IEEE Transactions on Industry Applications*, vol. 45, no. 2, pp. 582–590, 2009.

[132] K. J. Astrom and B. Wittenmark, "A survey of adaptive control applications," in *Decision and Control, 13-15 Dec. 1995, New Orleans, USA.*

[133] Y. Shi, K. Sun, L. Huang, and Y. Li, "Online identification of permanent magnet flux based on extended kalman filter for ipmsm drive with position sensorless control," *IEEE Transactions on Industrial Electronics*, vol. 59, no. 11, pp. 4169–4178, 2012.

[134] D. Liang, J. Li, and R. Qu, "Sensorless control of permanent magnet synchronous machine based on second-order sliding-mode observer with online resistance estimation," *IEEE Transactions on Industry Applications*, vol. 53, no. 4, pp. 3672–3682, 2017.

[135] P. Mercorelli, "A hysteresis hybrid extended kalman filter as an observer for sensorless valve control in camless internal combustion engines," *IEEE Transactions on Industry Applications*, vol. 48, no. 6, pp. 1940–1949, 2012.

[136] ——, "A two-stage augmented extended kalman filter as an observer for sensorless valve control in camless internal combustion engines," *IEEE Transactions on Industrial Electronics*, vol. 59, no. 11, pp. 4236–4247, 2012.

[137] G. H. B. Foo, X. Zhang, and D. M. Vilathgamuwa, "A sensor fault detection and isolation method in interior permanent-magnet synchronous motor drives based on an extended kalman filter," *IEEE Transactions on Industrial Electronics*, vol. 60, no. 8, pp. 3485–3495, 2013.

[138] G. Foo and M. Rahman, "Sensorless sliding-mode mtpa control of an ipm synchronous motor drive using a sliding-mode observer and hf signal injection," *IEEE Transactions on Industrial Electronics*, vol. 57, no. 4, pp. 1270–1278, 2010.

[139] S. Sayeef, G. Foo, and M. F. Rahman, "Rotor position and speed estimation of a variable structure direct-torque-controlled ipm synchronous motor drive at very low speeds including standstill," *IEEE Transactions on Industrial Electronics*, vol. 57, no. 11, pp. 3715–3723, 2010.

[140] X. Luo, Q. Tang, A. Shen, and Q. Zhang, "Pmsm sensorless control by injecting hf pulsating carrier signal into estimated fixed-frequency rotating reference frame," *IEEE Transactions on Industrial Electronics*, vol. 63, no. 4, pp. 2294–2303, 2016.

[141] S. Medjmadj, D. Diallo, M. Mostefai, C. Delpha, and A. Arias, "Pmsm drive position estimation: Contribution to the high-frequency injection voltage selection issue," *IEEE Transactions on Energy Conversion*, vol. 30, no. 1, pp. 349–358, 2015.

[142] J. Liu and Z. Zhu, "Novel sensorless control strategy with injection of high-frequency pulsating carrier signal into stationary reference frame," *IEEE Transactions on Industry Applications*, vol. 50, no. 4, pp. 2574–2583, 2014.

[143] H. Kim and R. D. Lorenz, "Carrier signal injection based sensorless control methods for ipm synchronous machine drives," in *Industry Applications Conference, 3-5 Oct. 2004, Seattle, USA*.

[144] D. Raca, P. García, D. Reigosa, F. Briz, and R. Lorenz, "A comparative analysis of pulsating vs. rotating vector carrier signal injection-based sen-

sorless control," in *Applied Power Electronics Conference and Exposition, 24-28 Feb. 2008 Austin, TX USA*, pp. 879–885.

[145] N. Bianchi, S. Bolognani, J.-H. Jang, and S.-K. Sul, "Comparison of pm motor structures and sensorless control techniques for zero-speed rotor position detection," *IEEE Transactions on Power Electronics*, vol. 22, no. 6, pp. 2466–2475, 2007.

[146] Z. Zhu and L. Gong, "Investigation of effectiveness of sensorless operation in carrier-signal-injection-based sensorless-control methods," *IEEE Transactions on Industrial Electronics*, vol. 58, no. 8, pp. 3431–3439, 2011.

[147] M. Schroedl, "Sensorless control of ac machines at low speed and standstill based on the" inform" method," in *Industry Applications Conference, 6-9 Oct. 1996, San Diego, USA*.

[148] F. Briz, M. W. Degner, P. García, and R. D. Lorenz, "Comparison of saliency-based sensorless control techniques for ac machines," *IEEE Transactions on Industry Applications*, vol. 40, no. 4, pp. 1107–1115, 2004.

[149] M. J. Corley and R. D. Lorenz, "Rotor position and velocity estimation for a salient-pole permanent magnet synchronous machine at standstill and high speeds," *IEEE Transactions on Industry Applications*, vol. 34, no. 4, pp. 784–789, 1998.

[150] M. Fatu, R. Teodorescu, I. Boldea, G.-D. Andreescu, and F. Blaabjerg, "If starting method with smooth transition to emf based motion-sensorless vector control of pm synchronous motor/generator," in *IEEE Power Electronics Specialists Conference, 15-17 Jun. 2008, Rhodes, Greece*, 2008, pp. 1481–1487.

[151] H. Kim, J. Son, and J. Lee, "A high-speed sliding-mode observer for the sensorless speed control of a pmsm," *IEEE Transactions on Industrial Electronics*, vol. 58, no. 9, pp. 4069–4077, 2011.

[152] "Hysteresis dynamometers (hd series)," https://www.magtrol.com/product/hysteresis-dynamometers-hd-series/, accessed: May-10-2018.

[153] R. Norden, "Extra high strength structural steels for ice breakers," *British Maritime Technology*, 1989.

[154] "Russian nuclear icebreaker yamal on her way to the north pole, 2001," https://en.wikipedia.org/wiki/Icebreaker, accessed: Sep-30-2018.

[155] J. Lang and G. Verghese, "Adaptive estimation of state and parameters in electrical machines," in *European Conference on Power Electronics and Applications, 9-12 October, 1989, Aachen, Germany*, 1989, pp. 3–4.

[156] M. Vélez-Reyes, "Speed and parameter estimation for induction machines," Ph.D. dissertation, Massachusetts Institute of Technology, 1988.

[157] S. R. Shaw and S. B. Leeb, "Identification of induction motor parameters from transient stator current measurements," *IEEE Transactions on Industrial Electronics*, vol. 46, no. 1, pp. 139–149, 1999.

[158] H. A. Toliyat, E. Levi, and M. Raina, "A review of rfo induction motor parameter estimation techniques," *IEEE Transactions on Energy conversion*, vol. 18, no. 2, pp. 271–283, 2003.

[159] A. Bellini, A. De Carli, and M. La Cava, "Parameter identification for induction motor simulation," *IFAC Proceedings Volumes*, vol. 7, no. 2, pp. 195–205, 1974.

[160] A. Consoli, L. Fortuna, and A. Gallo, "Induction motor identification by a microcomputer-based structure," *IEEE Transactions on Industrial Electronics*, no. 4, pp. 422–428, 1987.

[161] C. Wang, D. W. Novotny, and T. A. Lipo, "An automated rotor time-constant measurement system for indirect field-oriented drives," *IEEE Transactions on Industry Applications*, vol. 24, no. 1, pp. 151–159, 1988.

[162] H. Schierling, "Self-commissioning-a novel feature of modern inverter-fed induction motor drives," in *Third International Conference on Power Electronics and Variable-Speed Drives, 13-15 July 1988, London, UK.* IET, 1988, pp. 287–290.

[163] R. Jötten and E. Lettner, "Adaptive and self-commissioning control for a drive with induction motor and current source inverter," in *European Conference on Power Electronics and Applications, 9-12 October, 1989, Aachen, Germany*, 1989, pp. 627–632.

[164] R. Joetten and G. Maeder, "Control methods for good dynamic performance induction motor drives based on current and voltage as measured quantities," *IEEE Transactions on Industry Applications*, no. 3, pp. 356–363, 1983.

[165] A. Nabae, I. Takahashi, H. Akagi, and H. Nakano, "Inverter-fed induction motor drive systems with an instantaneous slip-frequency estimation circuit," in *Power Electronics Specialists conference, 14-17 June 1982, Cambridge, MA, USA.*

[166] M. Vélez-Reyes, K. Minami, and G. C. Verghese, "Recursive speed and parameter estimation for induction machines," in *Industry Applications Society Annual Meeting, 1-5 October, 1989, San Diego, California.*

[167] S. N. Hasan and I. Husain, "A luenberger-sliding mode observer for on-line parameter estimation and adaptation in high-performance induction motor drives," in *IEEE Industry Applications Conference Forty-First IAS Annual Meeting, 8-11 Oct. 2006, Tampa, USA.*

[168] L. Loron and G. Laliberte, "Application of the extended kalman filter to parameters estimation of induction motors," in *Fifth European Conference on Power Electronics and Applications, 13-15 Sep. 1993, Brighton, UK.*

[169] L.-C. Zai, C. L. DeMarco, and T. A. Lipo, "An extended kalman filter approach to rotor time constant measurement in pwm induction motor drives," *IEEE Transactions on Industry Applications*, vol. 28, no. 1, pp. 96–104, 1992.

[170] T. Kataoka, S. Toda, and Y. Sato, "On-line estimation of induction motor parameters by extended kalman filter," in *Fifth European Conference on Power Electronics and Applications, 13-15 Sep. 1993, Brighton, UK.*

[171] R. Krishnan and F. C. Doran, "A method of sensing line voltages for parameter adaptation of inverter-fed induction motor servo drives," *IEEE Transactions on Industry Applications*, no. 4, pp. 617–622, 1987.

[172] M. Koyama, M. Yano, I. Kamiyama, and S. Yano, "Microprocessor-based vector control system for induction motor drives with rotor time constant identification function," *IEEE Transactions on Industry Applications*, no. 3, pp. 453–459, 1986.

[173] T. M. Rowan, R. J. Kerkman, and D. Leggate, "A simple on-line adaption for indirect field orientation of an induction machine," *IEEE Transactions on Industry Applications*, vol. 27, no. 4, pp. 720–727, 1991.

[174] D. Y. Ohm, Y. Khersonsky, and J. R. Kimzey, "Rotor time constant adaptation method for induction motors using dc link power measurement," in *Industry Applications Society Annual Meeting, 1-5 October, 1989, San Diego, California.*

[175] D. Dalal and R. Krishnan, "Parameter compensation of indirect vector controlled induction motor drive using estimated airgap power," in *Industry Applications Society annual meeting, October 6-11, 1987, New York, USA*, 1987, pp. 170–176.

[176] S. Wade, W. Dunnigan, and B. W. Williams, "A new method of rotor resistance estimation for vector-controlled induction machines," *IEEE Transactions on Industrial Electronics*, vol. 44, no. 2, pp. 247–257, 1997.

[177] S. Wade, M. W. Dunnigan, and B. W. Williams, "Modeling and simulation of induction machine vector control with rotor resistance identification," *IEEE Transactions on Power Electronics*, vol. 12, no. 3, pp. 495–506, 1997.

[178] J. C. Moreira and T. A. Lipo, "A new method for rotor time constant tuning in indirect field oriented control," *IEEE Transactions on Power Electronics*, vol. 8, no. 4, pp. 626–631, 1993.

[179] J.-S. Choi, Y.-S. Han, and Y.-S. Kim, "A new speed estimation scheme of the induction motor considering the flux saturation," *IEEE Transactions on Magnetics*, vol. 36, no. 5, pp. 3595–3598, 2000.

[180] T. Lipo and D. Novotny, *Dynamics and Control of Induction Motor Drives.* Oxford Press, Clarendon, UK, 1995.

[181] J. L. Silvino and B. Rabelo, "An improved estimation of the induction machine leakage inductances," *IEEE Transactions on Industrial Electronics*, vol. 46, no. 5, pp. 1040–1042, 1999.

[182] R. Krishnan, *Electric motor drives: modeling, analysis, and control.* Prentice Hall, New Jersey, 2001, vol. 626.

[183] A. Shiri, A. Vahedi, and A. Shoulaie, "The effect of parameter variations on the performance of indirect vector controlled induction motor drive," in *IEEE International Symposium on Industrial Electronics, 9-12 Jul. 2006, Seattle, USA.*

[184] F. Mehazzem, A. Reama, and H. Benalla, "Online rotor resistance estimation based on mras-sliding mode observer for induction motors," in *Power Engineering, Energy and Electrical Drives (POWERENG), 13-16 May. 2013, Istanbul, Turkey.*

[185] D. M. Reed, H. F. Hofmann, and J. Sun, "Offline identification of induction machine parameters with core loss estimation using the stator current locus," *IEEE Transactions on Energy Conversion*, vol. 31, no. 4, pp. 1549–1558, 2016.

[186] H. Tajima, G. Guidi, and H. Umida, "Consideration about problems and solutions of speed estimation method and parameter tuning for speed sensorless vector control of induction motor drives," in *Industry Applications Conference, 8-10 Oct. 2000, Rome, Italy.*

[187] K. Akatsu and A. Kawamura, "Sensorless very low-speed and zero-speed estimations with online rotor resistance estimation of induction motor without signal injection," *IEEE Transactions on Industry Applications*, vol. 36, no. 3, pp. 764–771, 2000.

[188] T. Boileau, N. Leboeuf, B. Nahid-Mobarakeh, and F. Meibody-Tabar, "Online identification of pmsm parameters: Parameter identifiability and estimator comparative study," *IEEE Transactions on Industry Applications*, vol. 47, no. 4, pp. 1944–1957, 2011.

[189] O. Sandre-Hernandez, R. Morales-Caporal, J. Rangel-Magdaleno, H. Peregrina-Barreto, and J. N. Hernandez-Perez, "Parameter identification of pmsms using experimental measurements and a pso algorithm," *IEEE Transactions on Instrumentation and Measurement*, vol. 64, no. 8, pp. 2146–2154, 2015.

[190] M. Barcaro, N. Bianchi, and S. Bolognani, "Hybrid electric propulsion system using submersed spm machine," in *18th International Conference on Electrical Machines, 6-9 Sept. 2008, Vilamoura.*

[191] Ø. Krøvel, R. Nilssen, S. Skaar, E. Løvli, and N. Sandoy, "Design of an integrated 100kw permanent magnet synchronous machine in a prototype thruster for ship propulsion," *CD Rom Proceedings of ICEM*, pp. 117–118, 2004.

[192] R. Lateb, N. Takorabet, F. Meibody-Tabar, A. Mirzaian, J. Enon, and A. Sarribouette, "Performances comparison of induction motors and surface mounted pm motor for pod marine propulsion," in *Fourtieth IAS Annual Meeting, 2-6 Oct. 2005, Kowloon, Hong Kong*, vol. 2. IEEE, 2005, pp. 1342–1349.

[193] B. Ruzojcic, D. Zarko, and D. Ban, "Interior permanent-magnet motor for ship propulsion, design and testing," in *13th European Conference on Power Electronics and Applications, 8-10 Sept. 2009, Barcelona*, pp. 1–10.

[194] M. Rosu, A. Arkkio, T. Jokinen, J. Mantere, and J. Westerlund, "The influence of optimised stator geometry and rotor configuration on motor characteristics in permanent magnet synchronous motor for ship propulsion drive," in *International Conference IEMD, 9-12 May 1999, Seattle, WA, USA*, pp. 305–310.

[195] B. Stumberger, G. Stumberger, D. Dolinar, A. Hamler, and M. Trlep, "Evaluation of saturation and cross-magnetization effects in interior permanent-magnet synchronous motor," *IEEE Transactions on Industry Applications*, vol. 39, no. 5, pp. 1264–1271, 2003.

[196] A. Kilthau and J. Pacas, "Appropriate models for the control of the synchronous reluctance machine," in *Industry Applications Conference, 13-18 Oct. 2002, Pittsburgh, PA, USA*.

[197] N. Bianchi and S. Bolognani, "Magnetic models of saturated interior permanent magnet motors based on finite element analysis," in *Industry Applications Conference, 12-15 Oct. 1998, St.Louis, MO, USA*.

[198] E. Armando, R. I. Bojoi, P. Guglielmi, G. Pellegrino, and M. Pastorelli, "Experimental identification of the magnetic model of synchronous machines," *IEEE Transactions on Industry Applications*, vol. 49, no. 5, pp. 2116–2125, 2013.

[199] S. Morimoto, M. Sanada, and Y. Takeda, "Mechanical sensorless drives of ipmsm with online parameter identification," *IEEE Transactions on Industry Applications*, vol. 42, no. 5, pp. 1241–1248, 2006.

[200] J. Holtz and J. Quan, "Sensorless vector control of induction motors at very low speed using a nonlinear inverter model and parameter identification," in *Industry Applications Conference, 30 Sept.-4 Oct. 2001, Chicago, IL, USA*.

[201] B. Nahid-Mobarakeh, F. Meibody-Tabar, and F.-M. Sargos, "Mechanical sensorless control of pmsm with online estimation of stator resistance," *IEEE Transactions on Industry Applications*, vol. 40, no. 2, pp. 457–471, 2004.

[202] M. F. Rahman, M. E. Haque, L. Tang, and L. Zhong, "Problems associated with the direct torque control of an interior permanent-magnet synchronous motor drive and their remedies," *IEEE Transactions on Industrial Electronics*, vol. 51, no. 4, pp. 799–809, 2004.

[203] T. Fukumoto, H. Hamane, and Y. Hayashi, "Performance improvement of the ipmsm position sensor-less vector control system by the on-line motor parameter error compensation and the practical dead-time compensation," in *Power Conversion Conference, 2-5 April, 2007, Nagoya, Japan.*

[204] Y. Inoue, Y. Kawaguchi, S. Morimoto, and M. Sanada, "Performance improvement of sensorless ipmsm drives in a low-speed region using online parameter identification," *IEEE Transactions on Industry Applications*, vol. 47, no. 2, pp. 798–804, 2011.

[205] H. Kim and R. D. Lorenz, "Improved current regulators for ipm machine drives using on-line parameter estimation," in *Industry Applications Conference, 13-18 Oct. 2002, Pittsburgh, PA, USA*.

[206] K. Liu, Q. Zhang, J. Chen, Z.-Q. Zhu, and J. Zhang, "Online multiparameter estimation of nonsalient-pole pm synchronous machines with temperature variation tracking," *IEEE Transactions on Industrial Electronics*, vol. 58, no. 5, pp. 1776–1788, 2011.

[207] G. Feng, C. Lai, K. Mukherjee, and N. C. Kar, "Current injection-based online parameter and vsi nonlinearity estimation for pmsm drives using

current and voltage dc components," *IEEE Transactions on Transportation Electrification*, vol. 2, no. 2, pp. 119–128, 2016.

[208] S. J. Underwood and I. Husain, "Online parameter estimation and adaptive control of permanent-magnet synchronous machines," *IEEE Transactions on Industrial Electronics*, vol. 57, no. 7, pp. 2435–2443, 2010.

[209] S. Ichikawa, M. Tomita, S. Doki, and S. Okuma, "Sensorless control of permanent-magnet synchronous motors using online parameter identification based on system identification theory," *IEEE Transactions on Industrial Electronics*, vol. 53, no. 2, pp. 363–372, 2006.

[210] Z.-Q. Zhu, X. Zhu, P. Sun, and D. Howe, "Estimation of winding resistance and pm flux-linkage in brushless ac machines by reduced-order extended kalman filter," in *Networking, Sensing and Control, 15-17 April, 2007, London, UK.*

[211] T. Senjyu, Y. Kuwae, N. Urasaki, and K. Uezato, "Accurate parameter measurement for high speed permanent magnet synchronous motors," in *Power Electronics Specialists Conference, 17-21 June 2001, Vancouver, BC, Canada.*

[212] K. M. Rahman and S. Hiti, "Identification of machine parameters of a synchronous motor," *IEEE Transactions on Industry Applications*, vol. 41, no. 2, pp. 557–565, 2005.

[213] W. Su and C. Liaw, "Robust balanced control of lpmsm servo drive with mass identification and large command change," *IEE Proceedings-Electric Power Applications*, vol. 153, no. 3, pp. 439–450, 2006.

[214] Y. Yi, D. M. Vilathgamuwa, and M. A. Rahman, "Implementation of an artificial-neural-network-based real-time adaptive controller for an interior permanent-magnet motor drive," *IEEE Transactions on Industry Applications*, vol. 39, no. 1, pp. 96–104, 2003.

[215] L. Sepulchre, M. Fadel, M. Pietrzak-David, and G. Porte, "New high speed pmsm flux-weakening strategy," in *Electrical Machines and Systems (ICEMS), 13-16 Nov, 2016, Chiba, Japan.*

[216] Y. Engel, S. Mannor, and R. Meir, "The kernel recursive least squares algorithm," *IEEE Transactions on Signal Processing*, vol. 52, no. 8, pp. 2275–2285, 2004.

List of Publications

- J. Zhai, Y. Wang and X. Liu, "Optimal reset controller designed for induction machine drive with hardware in the loop test," 2017 IEEE Applied Power Electronics Conference and Exposition (APEC), Tampa, FL, 2017, pp. 506-511.
- L. Niu, J. Zhai, X. Liu, Y. Wang and A. K. Gupta, "A smooth and fast transition method for PMSM SMO based sensorless control," 2016 IEEE 2nd Annual Southern Power Electronics Conference (SPEC), Auckland, 2016, pp. 1-6.
- K. Han, J. Zhai, Y. Wang and X. Liu, "Dead time compensation with variable resonant controller for induction motor drive system," 2017 13th IEEE International Conference on Control & Automation (ICCA), Ohrid, 2017, pp. 1090-1094.
- L. Niu, X. Liu, Y. Wang, A. K. Gupta and J. Zhai, "Induction machine rotor time constant identification using bisection search method," 2016 IEEE Region 10 Conference (TENCON), Singapore, 2016, pp. 3648-3652.